Cell Reports
Medicine

Article

Dysregulation of FLVCR1a-dependent mitochondrial calcium handling in neural progenitors causes congenital hydrocephalus

Graphical abstract

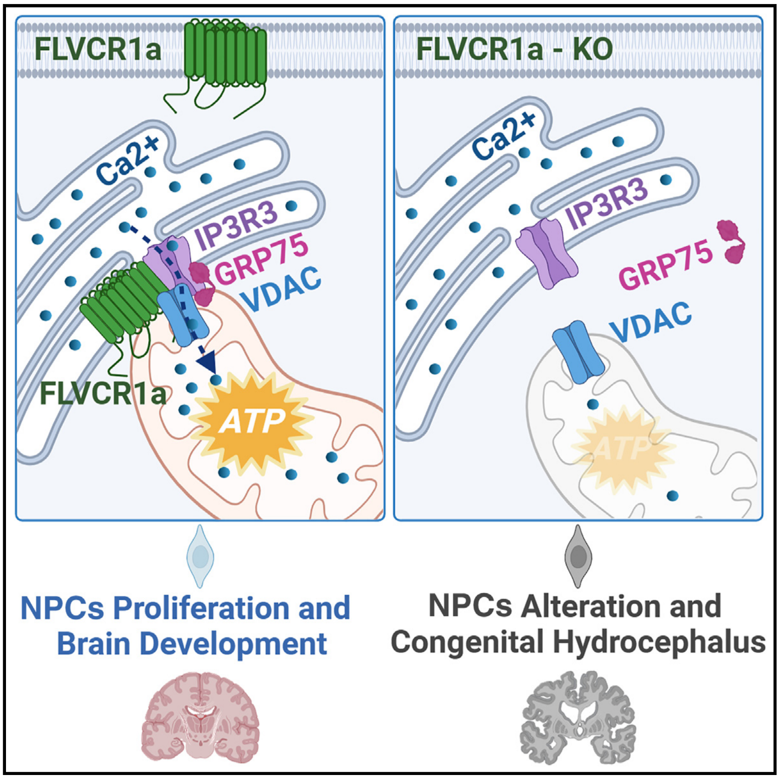

Highlights

- *FLVCR1* loss causes congenital hydrocephalus (CH) in humans and mice
- FLVCR1a interacts with the IP3R3-VDAC complex to regulate mitochondrial Ca^{2+} handling
- Loss of Flvcr1a-dependent Ca^{2+} regulation disrupts mitochondrial function in NPCs
- Mitochondrial Ca^{2+} loading restores the proliferation of Flvcr1a-null NPCs

Authors

Francesca Bertino, Dibyanti Mukherjee, Massimo Bonora, ..., Thomas Arnold, Emanuela Tolosano, Deborah Chiabrando

Correspondence

deborah.chiabrando@unito.it

In brief

Bertino et al. identify *FLVCR1* as a congenital hydrocephalus (CH)-associated gene. FLVCR1a coordinates neurogenesis by interacting with the IP3R3-VDAC complex, thereby regulating mitochondrial Ca^{2+} handling. Disruption of this process in *Flvcr1a*-null mouse NPCs leads to impaired mitochondrial function, defective neurogenesis, and brain ventricle enlargement, driving CH pathogenesis.

Bertino et al., 2024, Cell Reports Medicine *5*, 101647
July 16, 2024 © 2024 The Author(s). Published by Elsevier Inc.
https://doi.org/10.1016/j.xcrm.2024.101647

Cell Reports Medicine

CellPress
OPEN ACCESS

Article

Dysregulation of FLVCR1a-dependent mitochondrial calcium handling in neural progenitors causes congenital hydrocephalus

Francesca Bertino,[1] Dibyanti Mukherjee,[2] Massimo Bonora,[3] Christoph Bagowski,[4] Jeannette Nardelli,[5] Livia Metani,[1] Diletta Isabella Zanin Venturini,[1] Diego Chianese,[3] Nicolas Santander,[6] Iris Chiara Salaroglio,[7] Andreas Hentschel,[8] Elisa Quarta,[1] Tullio Genova,[9] Arpana Arjun McKinney,[10,11] Anna Lucia Allocco,[1] Veronica Fiorito,[1] Sara Petrillo,[1] Giorgia Ammirata,[1] Francesco De Giorgio,[1] Evan Dennis,[12] Garrett Allington,[12] Felicitas Maier,[4] Moneef Shoukier,[4] Karl-Philipp Gloning,[4] Luca Munaron,[9] Federico Mussano,[13] Ettore Salsano,[14] Davide Pareyson,[14] Maja di Rocco,[15] Fiorella Altruda,[1] Georgia Panagiotakos,[10,11] Kristopher T. Kahle,[16,17,18] Pierre Gressens,[5] Chiara Riganti,[7] Paolo P. Pinton,[3] Andreas Roos,[19,20,21] Thomas Arnold,[2] Emanuela Tolosano,[1] and Deborah Chiabrando[1,22,*]

[1]Department of Molecular Biotechnology and Health Sciences, Molecular Biotechnology Center "Guido Tarone", University of Torino, Torino, Italy
[2]Department of Pediatrics, Neonatal Brain Research Institute, University of California San Francisco, San Francisco, CA, USA
[3]Department of Medical Sciences, Section of Experimental Medicine, Laboratory for Technologies of Advanced Therapies, University of Ferrara, Ferrara, Italy
[4]Prenatal Medicine Munich, Department of Molecular Genetics, Munich, Germany
[5]Université Paris Cité, Inserm, NeuroDiderot, 75019 Paris, France
[6]Instituto de Ciencias de la Salud, Universidad de O'Higgins, Rancagua, Chile
[7]Department of Oncology, Molecular Biotechnology Center "Guido Tarone", University of Torino, Torino, Italy
[8]Leibniz-Institut für Analytische Wissenschaften-ISAS-e.V., Dortmund, Germany
[9]Department of Life Sciences and Systems Biology, University of Torino, Torino, Italy
[10]Eli and Edythe Broad Center of Regeneration Medicine and Stem Cell Research, Department of Biochemistry and Biophysics, University of California, San Francisco, San Francisco, CA, USA
[11]Departments of Psychiatry and Neuroscience, Institute for Regenerative Medicine, Black Family Stem Cell Institute, Seaver Center for Autism Research and Treatment, Mindich Child Health and Development Institute, Icahn School of Medicine at Mount Sinai, New York, NY, USA
[12]Department of Neurosurgery, Massachusetts General Hospital, Harvard Medical School, Boston, MA, USA
[13]Bone and Dental Bioengineering Laboratory, CIR Dental School, Department of Surgical Sciences, University of Torino, Torino, Italy
[14]Unit of Rare Neurological Diseases, Fondazione IRCCS Istituto Neurologico Carlo Besta, Milano, Italy
[15]Department of Pediatrics, Unit of Rare Diseases, Giannina Gaslini Institute, Genoa, Italy
[16]Division of Genetics and Genomics, Manton Center for Orphan Disease Research, Department of Pediatrics, and Howard Hughes Medical Institute, Boston Children's Hospital, Boston, MA, USA
[17]Broad Institute of MIT and Harvard, Cambridge, MA, USA
[18]Harvard Center for Hydrocephalus and Neurodevelopmental Disorders, Massachusetts General Hospital, Boston, MA, USA
[19]Department of Pediatric Neurology, Centre for Neuromuscular Disorders, Centre for Translational Neuro- and Behavioral Sciences, University Duisburg-Essen, 45147 Essen, Germany
[20]Brain and Mind Research Institute, Children's Hospital of Eastern Ontario Research Institute, Ottawa, ON K1H 8L1, Canada
[21]Department of Neurology, Medical Faculty and University Hospital Düsseldorf, Heinrich Heine University, 40225 Düsseldorf, Germany
[22]Lead contact
*Correspondence: deborah.chiabrando@unito.it

https://doi.org/10.1016/j.xcrm.2024.101647

SUMMARY

Congenital hydrocephalus (CH), occurring in approximately 1/1,000 live births, represents an important clinical challenge due to the limited knowledge of underlying molecular mechanisms. The discovery of novel CH genes is thus essential to shed light on the intricate processes responsible for ventricular dilatation in CH. Here, we identify *FLVCR1* (feline leukemia virus subgroup C receptor 1) as a gene responsible for a severe form of CH in humans and mice. Mechanistically, our data reveal that the full-length isoform encoded by the *FLVCR1* gene, FLVCR1a, interacts with the IP3R3-VDAC complex located on mitochondria-associated membranes (MAMs) that controls mitochondrial calcium handling. Loss of *Flvcr1a* in mouse neural progenitor cells (NPCs) affects mitochondrial calcium levels and energy metabolism, leading to defective cortical neurogenesis and brain ventricle enlargement. These data point to defective NPCs calcium handling and metabolic activity as one of the pathogenetic mechanisms driving CH.

INTRODUCTION

Congenital hydrocephalus (CH) is a common and morbid brain malformation characterized by enlargement of the cerebrospinal fluid (CSF)-filled ventricles in the brain, associated with marked neurodevelopmental disabilities.[1,2] CH is the leading reason for brain surgery in infants as neurosurgical CSF diversion remains the only therapeutic option.[3] Even though neurosurgical CSF diversion is beneficial for a subset of patients, ventriculomegaly and neurocognitive impairments persist in a substantial number of patients with CH,[4] thus highlighting our poor understanding of CH pathogenesis.

CH is a complex disorder influenced by both genetic and environmental factors.[1,5] It was traditionally considered a neurological disorder arising from impaired CSF dynamics. Indeed, any genetic or environmental factor impairing CSF production, flow, or reabsorption leads to CSF accumulation and increased intracranial pressure, with a negative impact on brain development and function. Interestingly, genetic studies recently pointed to impaired prenatal neurogenesis as a causative factor underpinning a non-negligible amount of CH cases.[6,7] According to the neuroprogenitor-based paradigm of CH, reduced neurogenesis might affect brain biomechanics, leading to a secondary enlargement of brain ventricles. In these cases, CSF removal is not effective because it is not addressing the primary cause of the disease.[6,7] The results of these studies will allow the identification of patients that can benefit from CSF diversion and highlight the need to identify novel therapeutic strategies for CH. For this reason, a better understanding of CH pathogenesis is mandatory. Indeed, the molecular mechanisms responsible for neurogenesis defects associated with CH remain largely unexplored.

Here, by describing a human fetus with a CH carrying a mutation in the *FLVCR1* (feline leukemia virus subgroup C receptor 1) gene and by generating a mouse model of the disease, we uncovered important mechanistic insights into CH pathogenesis. Initially identified as a plasma membrane heme exporter,[8] FLVCR1a has been recently proposed as a choline importer.[9–13] Our study broadened the known functions of FLVCR1a by exploring the intricate network of protein-protein interactions associated with this transporter. We demonstrated that FLVCR1a interacts with inositol 1,4,5 trisphosphate receptor type 3 (IP3R3) and voltage-dependent anion channel (VDAC). IP3R3 and VDAC form a complex of proteins involved in the tethering of mitochondrial and endoplasmic reticulum (ER) membranes that is crucial for the regulation of Ca^{2+} fluxes from the ER into the mitochondria.[14] Our analyses showed a key role of FLVCR1a in the maintenance of neural progenitor cells (NPCs) proliferation and survival through the regulation of mitochondria-ER contact sites, Ca^{2+} fluxes, and, consequently, cellular energetic metabolism.

Our findings converge on the deregulation of calcium handling as a key pathogenic mechanism driving CH and point to calcium and metabolic regulation as potential therapeutic entry points for CH.

RESULTS

An inactivating homozygous *FLVCR1* mutation causes CH in humans

We have here described a human fetus with a severe form of CH carrying a mutation in the *FLVCR1* gene. Sonographic examinations of 32 + 4 and 34 + 5 weeks of pregnancy showed extreme microcephaly with anechoic skull and no evidence of cerebral tissue (Figures 1A, S1A and S1B). The falx cerebri, thalami, tentorium, and cerebellum were normal. The internal carotid artery was not detectable on either side by color Doppler sonography (Figure S1C). These findings led to a prenatal diagnosis of hydranencephaly. The pregnancy was terminated in 34 + 5 gestational weeks with a birth weight of 1,590 g (−2.18z < 1 Pz), 41 cm body length (−2.31z < 1 Pz), and 27 cm head circumference (−3, 6 < 1 Pz). Macroscopic evaluation showed an immature male fetus of the 35th gestational week with microcephaly and hydrocephalus with only rudimentary cerebral structures and no indication of visceral anomalies (Figure S1D). Trio-whole-exome sequencing revealed a novel homozygous frameshift variant c.160delC, p. Arg54Gly fsTer59 in the *FLVCR1* gene (NM_014053.3, NP_054772.1) and confirmed the heterozygous status of the variant for both parents (Figure 1B). According to the American College of Medical Genetics (ACMG) guidelines, c.160delC, p. Arg54GlyfsTer59 in the *FLVCR1* gene is a likely pathogenic variant (class 4; PVS1; PM2).[15]

Mutations in the *FLVCR1* gene have been previously identified in patients with posterior column ataxia and retinitis pigmentosa (PCARP)[16–19] and hereditary sensory and autonomic neuropathy (HSAN).[20–23] *FLVCR1* mutations associated with PCARP/HSAN include either homozygous missense mutations or compound heterozygous mutations, characterized by a combination of a missense and a frameshift mutation. These variants are presumed to be partially inactivating. Remarkably, the mutation described herein represents one of the few instances of a frameshift *FLVCR1* mutation observed in homozygosity.

The *FLVCR1* gene encodes for two different isoforms, FLVCR1a and FLVCR1b, likely arising from alternative transcription start sites.[24] The c.160delC mutation occurs in the first exon of the *FLVCR1* gene, thus affecting the abundance of the full-length isoform, FLVCR1a. FLVCR1a is a complex glycosylated 12 transmembrane domain protein composed of 555 amino acids (60 kDa). The c.160delC mutation occurs very close to the translational start site, upstream of the region coding for the first transmembrane domain of the protein.[25] The mutation is predicted to give rise to a 112 amino acids (12 kDa) protein (Figure S1E). As no primary cells or tissue biopsy were available for biochemical investigations, we performed western blot analysis on the overexpressed mutated protein, showing the expression of a protein with a molecular weight mass of approximately 12 kDa, which is likely non-functional (Figure S1F).

Together, these data suggest that deleterious homozygous mutations in *FLVCR1* caused CH in humans, thus expanding the genetic basis of CH pathogenesis.

FLVCR1a is highly expressed by NPCs during development in humans and mice

As the genetic studies aforementioned indicate an essential role for FLVCR1a during brain development, we determined *FLVCR1*

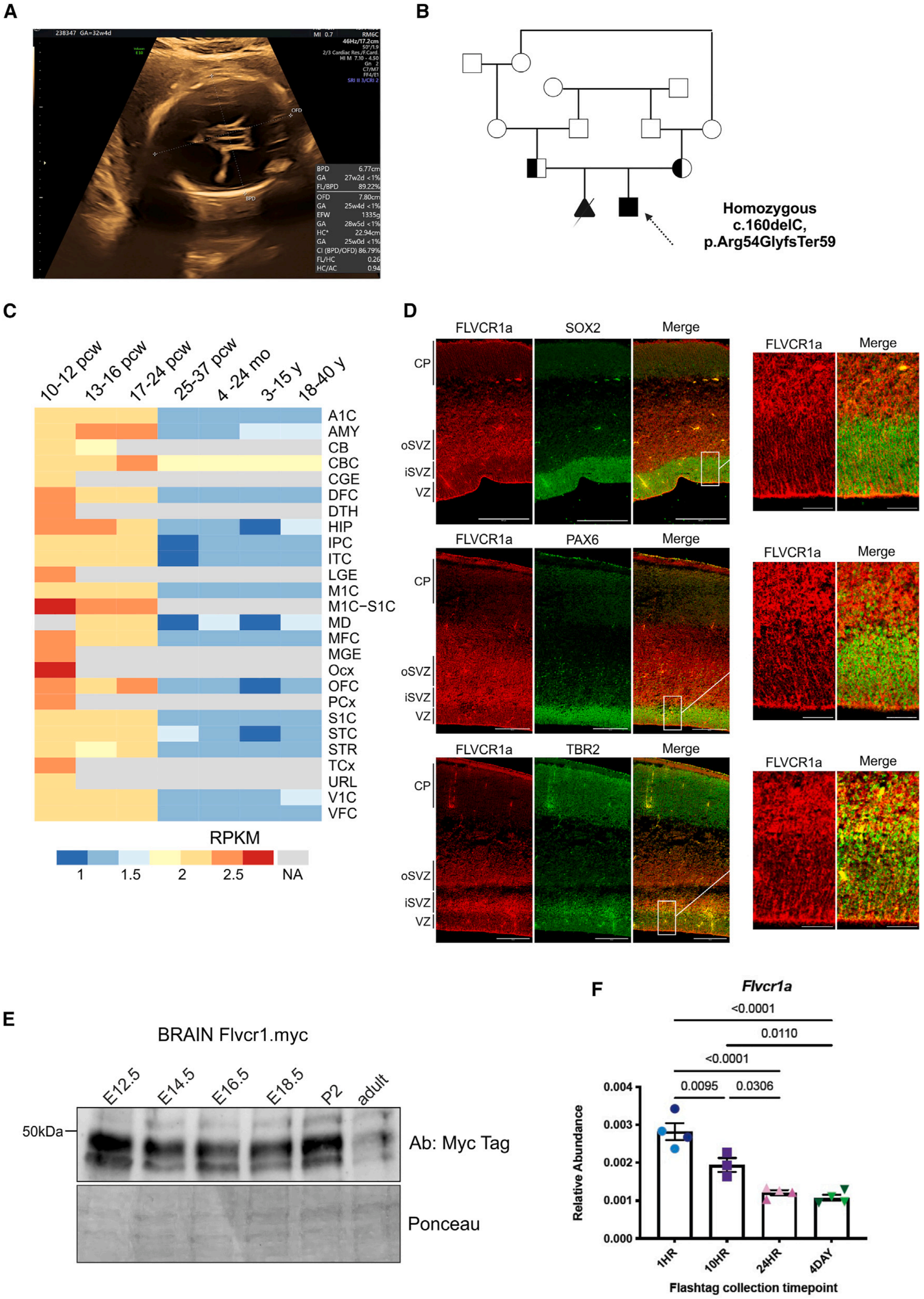

(legend on next page)

expression patterns during central nervous system (CNS) development.

Published atlases (https://www.brainspan.org/rnaseq/search/index.html; single-cell atlas) highlighted a 2-fold higher expression level of *FLVCR1a* in the first 24 weeks of gestation, compared to later stages of development (Figure 1C), with particularly strong expression in apical radial glial cell (RGC) progenitors (https://cells.ucsc.edu/?ds=early-brain&gene=FLVCR1). Immunofluorescence analyses performed on human brain slices at post-conception week 11 confirmed the enrichment of FLVCR1a in RGCs. FLVCR1a expression appears strong in SOX2+/PAX6+ RGCs and weaker but still present in TBR2+ intermediate progenitors (IPs) (Figure 1D). These data were further supported by the analysis of independent transcriptomic datasets, which showed greater *FLVCR1a* expression at early time points during human development (Figure S2A). Of note, *FLVCR1a* expression was reduced but not completely lost in the adult human brain (Figures S2B and S2C). In the fetal brain, a dataset from Fietz et al.[26] highlighted a peak of *FLVCR1a* expression in the ventricular zone (VZ) and outer subventricular zone that declined in the cortical plate (Figure S2D). Similarly, a different dataset from Pollen et al.[27] confirmed enriched expression of *FLVCR1a* in RGCs (Figure S2E).

To probe the expression of Flvcr1a in the developing mouse brain, we took advantage of mice expressing Flvcr1a fused with the Myc-Tag (Flvcr1-myc mouse).[28] Similarly to humans, Flvcr1a expression was higher in the developing brain and declined after birth (Figure 1E). Moreover, we performed *in utero* pulse-labeling via intraventricular injection of CFSE (“FlashTag” [FT]),[29] which allows fluorescence tagging of mitotic VZ progenitors lining the ventricles and subsequent tracking of time-locked cohorts of their postmitotic progeny, including neurons, throughout corticogenesis and early postnatal development. We performed FT injections at E13.5, isolated labeled cells at 1, 10, and 24 h and 4 days after injection, and then performed qPCR to assess the relative expression of *Flvcr1a* over time. This analysis revealed that *Flvcr1a* expression was highest in RGCs and progressively declined with differentiation (Figure 1F).

Collectively, these data indicate that *FLVCR1* expression peaks at early stages of neocortical development, with a specific enrichment in RGCs and IPs in both humans and mice.

Loss of *Flvcr1a* in NPCs impairs neurogenesis and causes CH in mice

To investigate the role of FLVCR1a in CNS development, we generated mice lacking *Flvcr1a* in NPCs by crossing mice bearing *Flvcr1a* floxed alleles (*Flvcr1a*$^{fl/fl}$)[30] with mice expressing Cre recombinase under the control of rat-Nestin promoter (NesCRE). *Flvcr1a*$^{fl/fl}$;NesCRE+ embryos were found at expected Mendelian ratios until embryonic day E18.5. However, no viable postnatal *Flvcr1a*$^{fl/fl}$;NesCRE+ mice were found in the offspring (Figures S3A and S3B), indicating perinatal lethality. Histological analysis showed that their pulmonary alveoli did not expand at birth (Figure S3C), suggesting that apnea could explain the newborn lethality. *Flvcr1a* deletion was verified by PCR analyses (Figures S3D) and confirmed by quantitative reverse-transcription PCR in the whole mouse embryo brains and in primary NPCs isolated from E12.5 mouse embryonic dorsal telencephalon (Figures S3E and S3F). Notably, Flvcr1b mRNA levels were also reduced in *Flvcr1a*$^{fl/fl}$;NesCRE+ embryo brains and NPCs (Figures S3G and S3H).

To analyze overall brain morphology and gross structural abnormalities resulting from *Flvcr1a* inactivation, we performed X-ray micro-computed tomography (micro-CT) on E18.5 *Flvcr1a*$^{fl/fl}$;NesCRE+ and *Flvcr1a*$^{fl/fl}$ embryos. Micro-CT analysis showed that *Flvcr1a*$^{fl/fl}$;NesCRE+ embryos displayed microcephaly, ventriculomegaly, and increased subarachnoid and perivascular spaces (Figure 2A), closely recapitulating the major clinical findings observed in the human fetus with homozygous *FLVCR1* mutations and representing a suitable animal model for the study of the human syndrome.

Transcriptomic analysis of E14.5 *Flvcr1a*$^{fl/fl}$;NesCRE+ and *Flvcr1a*$^{fl/+}$;NesCRE+ brains showed differential expression of core genes involved in both neuronal differentiation and NPCs proliferation (Figures S4A–S4D). Furthermore, we observed reduced expression of several genes related to CH, including *L1cam* and *Gli3* (Figure S4B). We also compared the transcriptomic profile of *Flvcr1a*$^{fl/fl}$;NesCRE+ embryos to those of two mouse models of CH characterized by activation of *Pik3ca* and disruption of *Prdm16* in neural progenitors,[31,32] respectively. This analysis revealed a core set of ∼50 genes differentially expressed in the three models with distinct degrees of correlation. Our model appeared closer to Pik3ca-overexpressing embryos

Figure 1. FLVCR1, responsible for CH in humans, is highly expressed by NPCs during development

(A) Sonographic examinations of 32 + 4 weeks of pregnancy showing extreme microcephaly with anechoic skull and no evidence of cerebral tissue in a human fetus carrying the c.160delC, p.Arg54GlyfsTer59 mutation in the *FLVCR1* gene.

(B) Family tree of the affected fetus.

(C) *FLVCR1a* expression data from developing human brain extracted from the dataset GSE25219 of the Human BrainSpan Atlas. This dataset consists of RNA sequencing and exon microarrays obtained at sequential developmental stages of the human brain. Heatmap indicates low (blue) and high (red) expression values. Gray color: no available data. PCW, post-conception weeks; A1C, auditory cortex; AMY, amygdala; CBC, cerebellar cortex; DFC, dorsolateral prefrontal cortex; HIP, hippocampus; IPC, posterior inferior parietal cortex; ITC, inferior temporal cortex; M1C, primary motor cortex; MD, mediodorsal nucleus of the thalamus; MFC, medial pre-frontal cortex; OFC, orbital prefrontal cortex; S1C, primary somatosensory cortex; STC, superior temporal cortex; STR, striatum; V1C, primary visual cortex; VFC, ventrolateral prefrontal cortex.

(D) FLVCR1a staining (red) in 11 post-conception weeks (PCW) human brain sections shows expression in RGCs (PAX6+ and SOX2+ cells) and IPs (TBR2+ cells). Scale bar: 500 μm. Magnified images of the insets on the left are shown on the right. Scale bar: 100 μm.

(E) Western blot analysis of FLVCR1a expression in the brains isolated from E12.5 to E18.5 embryos, 2 days (P2) and 3-month-old Flvcr1-myc mice. An anti-Myc-Tag antibody was used to detect endogenous FLVCR1a. A representative image is shown.

(F) Flvcr1a mRNA levels in “FlashTag”-labeled cell populations in the developing mouse cortex. The different isolation time points correspond to specific populations: 1 h = RGCs; 10 h = IPs; 24 h = newborn neurons; 4 days = neurons. Data represent mean ± SEM. See also Figure S1 and S2.

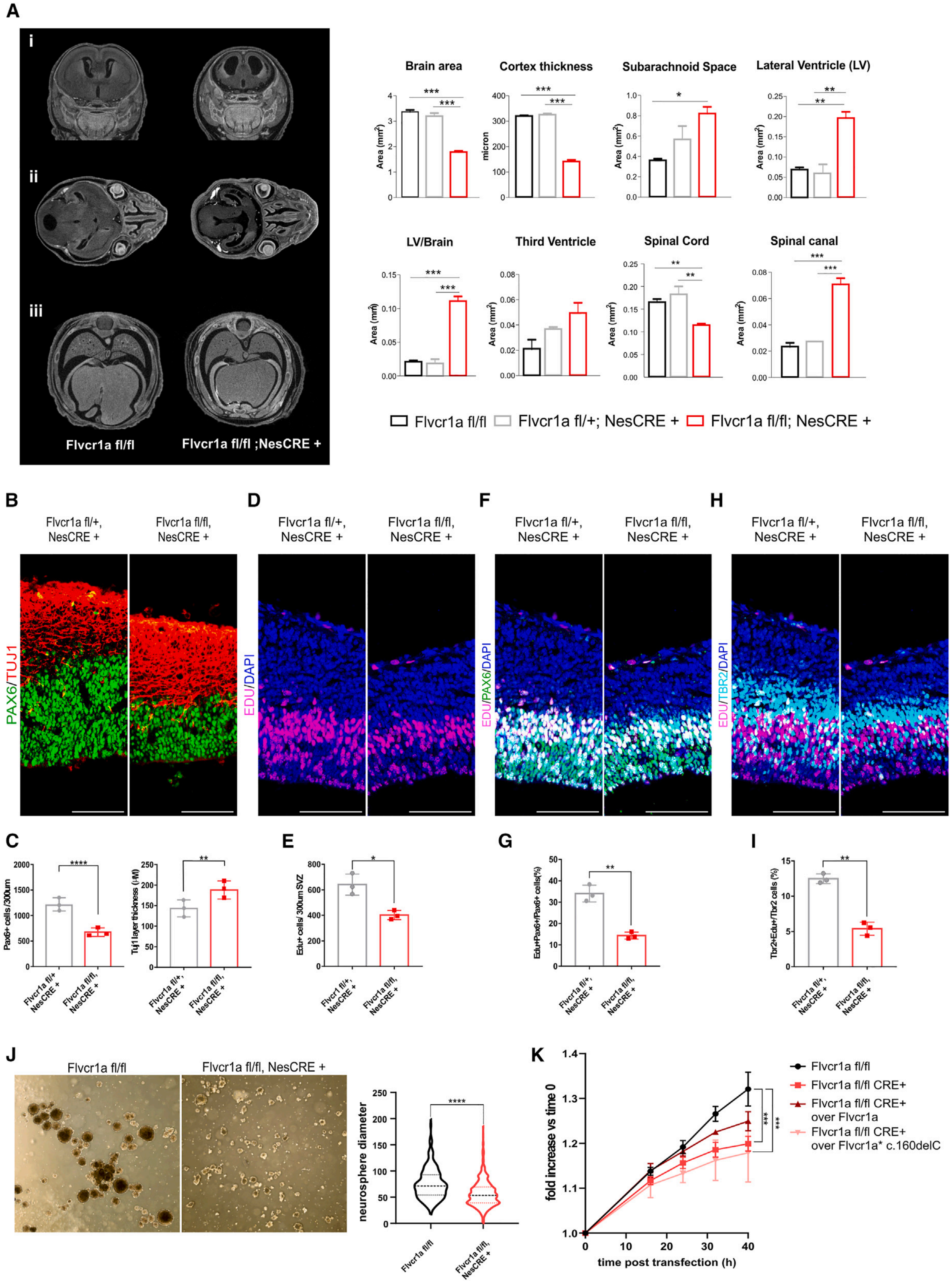

(legend on next page)

than to Prdm16-deleted animals, hinting at the impairment of cellular energetic metabolism in our model (Figure S4E).

These data suggest that defective neurogenesis contributes to CH in the absence of *Flvcr1a*. To analyze the impact of *Flvcr1a* loss on neurogenesis, we performed immunofluorescence staining of coronal brain sections. We observed reduced numbers of PAX6+ neural progenitors as early as E14.5 and an associated small but significant increase in the proportional thickness of the TUJ1+ neuronal layer in the developing cortex of *Flvcr1a*$^{fl/fl}$;NesCRE+ embryos compared to heterozygous mutants (Figure 2B and 2C). *Flvcr1a*$^{fl/fl}$;NesCRE+ embryos also displayed reduced numbers of TBR2+ IPs (Figure S5A). Similarly, cells expressing the layer-specific markers TBR1 and CTIP2 were less abundant (Figures S5B and S5C). Noteworthy, the same alterations persisted in *Flvcr1a*$^{fl/fl}$;NesCRE+ embryos at subsequent developmental stages (Figures S5D–S5G).

To evaluate whether alterations in cell proliferation accounted for the reduced neural progenitors at E14.5, we performed *in vivo* EdU labeling and TUNEL assay, respectively. EdU was injected into pregnant dams 2 hours prior to sacrifice, and embryos were collected at two different developmental stages. We found a significant reduction in the number of total EdU+ proliferative cells at E14.5 and E16.5, as well as a reduction in the number of both EdU+/PAX6+ and EdU+/TBR2+ cells (Figures 2D–2I and S6A–S6F).

To corroborate these data, NPCs were isolated from *Flvcr1a*$^{fl/fl}$ and *Flvcr1a*$^{fl/fl}$;NesCRE+ embryos. The dorsal telencephalon of E12.5 embryos was dissected to obtain neurospheres, which were subsequently mechanically dissociated to establish cortical NPC cultures. The diameter of *Flvcr1a*$^{fl/fl}$;NesCRE+ neurospheres was significantly smaller compared to control, suggesting early impaired proliferation of NPCs (Figure 2J). To elucidate whether the observed reduction in proliferation is attributed to the loss of Flvcr1a during neurodevelopment, we overexpressed both FLVCR1a and FLVCR1a*c160del in *Flvcr1a*$^{fl/fl}$;NesCRE+ NPCs (Figure S6G). Our analyses revealed that the impaired proliferation of *Flvcr1a*$^{fl/fl}$;NesCRE+ NPCs was restored upon FLVCR1a overexpression, while overexpression of FLVCR1a*c160del had no significant effect (Figures 2K and S6H).

Finally, we assessed whether cell death also contributed to the reduced cortical thickness of *Flvcr1a*$^{fl/fl}$;NesCRE+ embryos. Interestingly, TUNEL analysis revealed increased apoptosis in the cortex of E14.5 *Flvcr1a*$^{fl/fl}$;NesCRE+ embryos compared to *Flvcr1a*$^{fl/+}$;NesCRE+ mice (Figures S6I, and S6J).

Taken together, these data indicate that loss of FLVCR1a in neuroprogenitors leads to early disruptions in neurogenesis, by affecting the proliferation, differentiation, and survival of NPCs.

FLVCR1a interacts with the IP3R3-VDAC complex

To elucidate how FLVCR1a may regulate neural progenitor function, we investigated the FLVCR1a interactome using the tandem affinity purification (TAP) strategy coupled to tandem mass spectrometry. The FLVCR1a protein complex was purified from HEK293 T-Rex Flp-in cells overexpressing FLVCR1a fused with a small tag (TAP tag), which does not affect protein expression and localization (Figure S7A). The FLVCR1a protein complex was subsequently isolated (Figure S7B), analyzed on an SDS gel, and subjected to mass spectrometry. To discriminate false positive interactors, the empty vector expressing the TAP tag alone was used as a negative control. In total, 501 proteins could be identified with mass spectrometry analysis in the pull-down samples, of which 312 proteins were quantifiable (detected with at least 2 unique peptides). The top 50 FLVCR1a interactors are shown, stratified based on the ratio of FLVCR1a-TAP pull-down/empty, and sorted top to bottom from highest to least enriched proteins (Figure S7C). The extensive analysis of the interactome showed an enrichment of components of mitochondria, ER, and mitochondria-associated membranes (MAMs) (Figures 3A, 3B, and S7D).

Among all the identified FLVCR1a interactors, we found IP3R3, VDAC, and GRP75 proteins, which form a complex at MAMs mediating calcium transfer from the ER to mitochondria.[33] Interestingly, mitochondrial calcium is a positive regulator of various aspects of mitochondrial metabolism, which has recently been implicated in the regulation of NPC proliferation.[34–39]

These observations have prompted us to hypothesize that the interplay between FLVCR1a and the IP3R3-VDAC complex could play a crucial role in the proliferation of NPCs. Therefore, we verified the interaction between FLVCR1a and the

Figure 2. Loss of *Flvcr1a* in murine NPCs impairs neurogenesis and causes CH

(A) Micro-CT analyses performed on *Flvcr1a*$^{fl/fl}$;NesCRE+ and *Flvcr1a*$^{fl/+}$;NesCRE+ and *Flvcr1a*$^{fl/fl}$ embryos at E18.5. Quantification of the area of the brain, subarachnoid space, ventricles, spinal cord, spinal canal, and the cortical thickness with ImageJ software. Data represent mean ± SEM. ($n = 3$; one-way ANOVA, * = $p < 0.05$; ** = $p < 0.005$; *** = $p < 0.001$.)

(B) Immunostaining of PAX6+ and TUJ1+ cells of E14.5 *Flvcr1a*$^{fl/fl}$;NesCRE+ and *Flvcr1a*$^{fl/+}$;NesCRE+ cortexes. Each dot represents the mean of 3 images quantified from each animal. $N = 3$. Scale bar, 100 μm.

(C) Relative quantification of PAX6+ cells and TUJ1 thickness layer. Each dot represents the mean of 3 images quantified from each animal. Data represent mean ± SEM. $n = 3$.

(D) EdU staining of E14.5 *Flvcr1a*$^{fl/fl}$;NesCRE+ and *Flvcr1a*$^{fl/+}$;NesCRE+ cortexes. DAPI (blue) was used as a nuclear marker. Scale bar, 100 μm.

(E) Relative quantification of EdU+ cells. Each dot represents the mean of three images quantified from each animal. Data represent mean ± SEM. $n = 3$.

(F) EdU and PAX6 co-staining of E14.5 *Flvcr1a*$^{fl/fl}$;NesCRE+ and *Flvcr1a*$^{fl/+}$;NesCRE+ cortexes. DAPI (blue) was used as a nuclear marker. Scale bar, 100 μm.

(G) Relative quantification of EdU+/Pax6+ cells. Each dot represents the mean of three images quantified from each animal. Data represent mean ± SEM. $n = 3$.

(H) EdU and TBR2 co-staining of E14.5 *Flvcr1a*$^{fl/fl}$;NesCRE+ and *Flvcr1a*$^{fl/+}$;NesCRE+ cortex. DAPI (blue) was used as a nuclear marker. Scale bar, 100 μm. (I) Relative quantification of EdU+/TBR2+ cells. Each dot represents the mean of 3 images quantified from each animal. Data represent mean ± SEM. $n = 3$.

(J) Neurospheres isolated from *Flvcr1a*$^{fl/fl}$;NesCRE+ and *Flvcr1a*$^{fl/fl}$ cortexes and quantification of their diameter (t test; * = $p < 0.05$; ** = $p < 0.01$; *** = $p < 0.001$; **** = $p < 0.0001$).

(K) Proliferation rate of *Flvcr1a*$^{fl/fl}$ NPCs overexpressing an empty vector and *Flvcr1a*$^{fl/fl}$;NesCRE+ NPCs overexpressing an empty vector, FLVCR1a-myc, or FLVCR1a*c.160del-myc. Each time point represents the mean ± SEM of 5 different biological replicates (two-way ANOVA, *** = $p < 0.001$). See also Figures S3, S4, S5, S6.

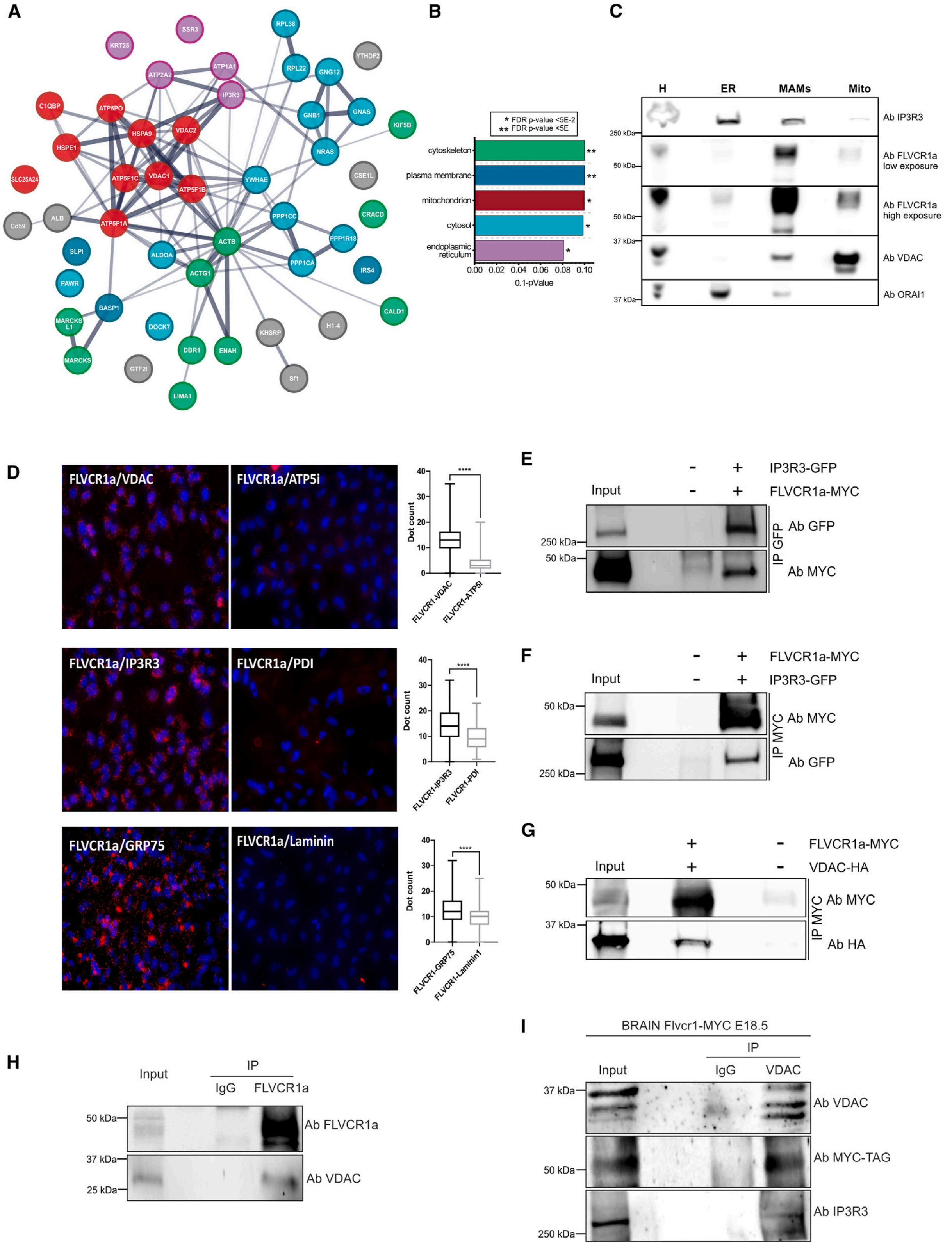

(legend on next page)

IP3R3-VDAC complex. Interestingly, immunofluorescence analyses showed that the endogenous FLVCR1a protein localized mostly at the plasma membrane but also intracellularly, where it partially co-localized with IP3R3, VDAC, and GRP75 as well as with the MAMs marker Sigmar1 (Figure S8A–S8D). Furthermore, subcellular fractionation showed that FLVCR1a is highly enriched in a subcellular fraction together with IP3R3 and VDAC (Figure 3C). Proximity ligation assay (PLA) confirmed the endogenous colocalization of FLVCR1a and VDAC, FLVCR1a and IP3R3, as well as FLVCR1a and GRP75 (Figure 3D). To confirm the protein-protein interaction, we purified FLVCR1a-TAP and performed western blot analysis for endogenous IP3R3 and VDAC (Figure S8E) and found that both proteins co-immunoprecipitated with FLVCR1a. The interaction was also validated by co-immunoprecipitation upon overexpression of the proteins (Figures 3E–3G). Immunoprecipitation of endogenous FLVCR1a from HEK293 cells followed by immunoblotting for VDAC demonstrated the interaction between endogenous FLVCR1a and VDAC (Figure 3H). Finally, immunoprecipitation of endogenous VDAC from E18.5 brains dissected from Flvcr1-myc embryos confirmed the interaction of FLVCR1a and VDAC *in vivo* (Figure 3I). Taken together, these data demonstrate that FLVCR1a interacts with the IP3R3-VDAC complex.

FLVCR1a regulates ER-mitochondria membrane tethering and mitochondrial calcium uptake

As the IP3R3-VDAC complex regulates ER-mitochondria membrane tethering, we investigated whether *FLVCR1a* loss in human cells results in MAM impairment. To this end, we analyzed the number of ER-mitochondria contact sites in HeLa cells upon *FLVCR1a* downregulation (Figures 4A and S9G) by confocal microscopy, using the two fluorescent proteins sec61-GFP and mt-DsRed to visualize the ER and mitochondria, respectively. Colocalization of the two fluorophores was then quantified as a proxy for ER-mitochondria membrane contacts. Interestingly, we observed a significant reduction in the number of MAMs upon *FLVCR1a* silencing, as quantified by Mander's colocalization coefficients and Pearson correlation coefficient (Figures 4B and 4C). Moreover, a decrease in ER-mitochondria tethering was further confirmed by PLA using the IP3R3-VDAC antibody pair (Figures 4D and 4E). To exclude the possibility that decreased abundance of IP3R3 and VDAC contributes to the observed reduction in MAMs, we analyzed their expression in *FLVCR1a*-silenced HeLa cells, but no alterations were observed (Figure 4F), confirming that *FLVCR1a* downmodulation disrupts MAMs in HeLa cells.

As the IP3R3-VDAC complex mediates calcium influx from the ER to mitochondria, we next investigated whether the modulation of FLVCR1a affects the activity of the complex. We analyzed HeLa cells expressing mtAEQmut, an aequorin-based calcium probe located in the mitochondrial matrix. The administration of histamine acts on Gq-coupled plasma membrane receptors and causes the production of inositol 1,4,5 trisphosphate (IP3), thus inducing the release of calcium from the ER to mitochondria and its consequent, transient, accumulation within mitochondrial matrix.[40] The efficiency of the ion transfer between the two compartments is highly sensitive to the status of MAMs.[41] The elevation of mitochondrial calcium concentration was significantly limited in *FLVCR1a*-deficient vs*.* proficient HeLa cells (Figures 4G and 4H), and reduced calcium influx in mitochondria was further confirmed using the fluorescence resonance energy transfer-based mitochondrial calcium reporter, 4mtD3CPV (Figure 4I). Importantly, cytosolic calcium was almost unaffected upon *FLVCR1a* silencing (Figure S9A and S9B), as was the store-operated Ca2+ entry (SOCE)-dependent mitochondrial Ca^{2+} uptake (Figures S9C and S9D) that involved the plasma membrane-ER contact sites.[42,43] Furthermore, FLVCR1a depletion did not affect the opening of the mitochondrial permeability transition pore (mPTP) (Figures S9E and S9F) as assessed by the Calcein-Co assay.[44,45] Overall, these data suggest that *FLVCR1a* downregulation specifically impairs ER-to-mitochondria calcium transfer through the IP3R3-VDAC1 complex and unveils an important functional role of FLVCR1a at MAMs.

To better dissect the role of FLVCR1a in MAM regulation, we analyzed HeLa cells overexpressing a Myc-tagged FLVCR1a protein (Figure 4J). Interestingly, overexpression of FLVCR1a resulted in increased ER-mitochondria contact sites (Figure 4K) and mitochondrial calcium uptake upon histamine stimulation (Figures 4L–4M). These data further support the role of FLVCR1a in the maintenance of MAM integrity and function.

As mutations in *FLVCR1* have been described in patients with PCARP/HSAN,[16–23] we sought to investigate if MAMs are

Figure 3. FLVCR1a interacts with the IP3R3-VDAC complex

(A) STRING analysis of the top 50 FLVCR1a interactors.

(B) Gene Ontology term analysis for subcellular compartments of the top 50 FLVCR1a interactors.

(C) Subcellular fractioning of HeLa cells. H, homogenate; ER, endoplasmic reticulum; MAMs, mitochondria-associated membranes; Mito, pure mitochondria.

(D) PLA was performed in HeLa cells using the FLVCR1a and VDAC1 antibodies (FLVCR1a-ATP5i pair was used as a negative control), or the FLVCR1a and IP3R3 antibodies (FLVCR1a-PDI pair was used as a negative control), or the FLVCR1a and GRP75 antibodies (FLVCR1a-Laminin pair was used as a negative control). (non parametric Mann-Whitney U test; **** = $p < 0.0001$.)

(E) Immunoprecipitation assay to detect the interaction between IP3R3-GFP and FLVCR1a-Myc. The protein complex was immune-precipitated using anti-GFP antibody, and the eluted proteins were detected by immunoblotting using either an anti Myc-Tag or an anti-GFP antibody. The vector expressing GFP alone was used as a negative control.

(F) Immunoprecipitation assay to detect the interaction between FLVCR1a-Myc and IP3R3-GFP. The protein complex was immune-precipitated using anti-Myc-Tag antibody, and the eluted proteins were detected by immunoblotting using either an anti-GFP or an anti Myc-Tag antibody.

(G) Immunoprecipitation assay to detect the interaction between FLVCR1a-Myc and VDAC-HA. The protein complex was immune-precipitated by an anti-Myc-Tag antibody, and the eluted proteins were detected by immunoblotting using either an anti-HA or an anti Myc-Tag antibody.

(H) Immunoprecipitation of endogenous FLVCR1a from HEK293 cells followed by immunoblotting of the eluted proteins by an anti-VDAC antibody.

(I) Immunoprecipitation of endogenous VDAC from E18.5 brains collected from the Flvcr1-myc embryos followed by immunoblotting using an anti-myc-Tag antibody. See also Figures S7 and S8.

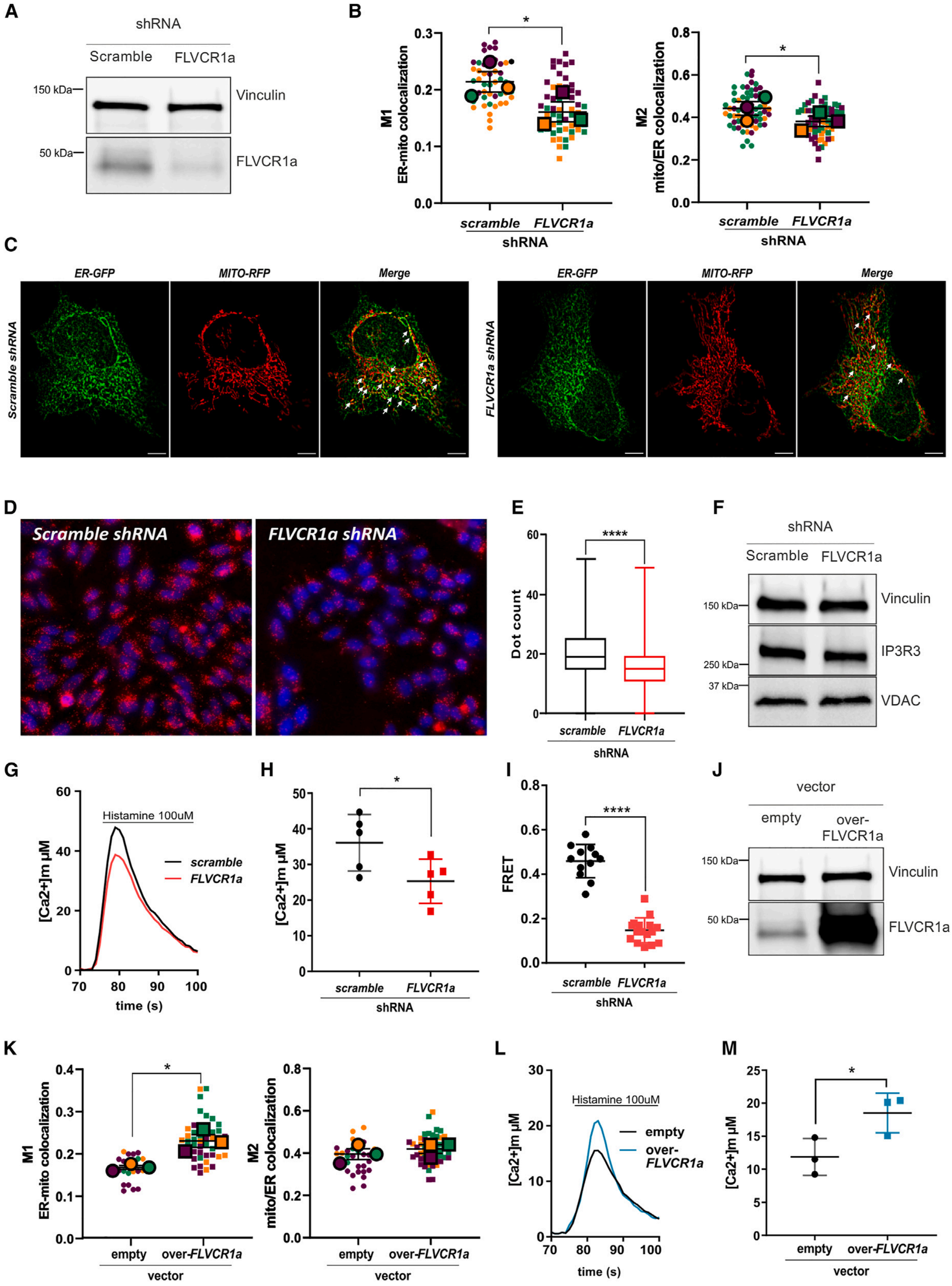

(legend on next page)

affected in primary fibroblasts derived from these patients compared to healthy volunteers. To this end, we analyzed FLVCR1a abundance, the extent of MAMs, and ER-to-mitochondria calcium fluxes. Interestingly, FLVCR1a is still expressed in patient-derived cells, but at lower levels (Figure 5A). PLA analysis using the IP3R3-VDAC antibody pair showed a decrease in the extent of MAMs in patients' cells (Figures 5B and 5C), despite the unchanged expression of IP3R3 and VDAC (Figure 5D). Of note, we observed a dramatic defect in mitochondrial calcium uptake in patient-derived cells as compared to healthy subjects (Figures 5E and 5F), independently from the expression level of the mitochondrial calcium uniporter (MCU) that was not affected by *FLVCR1* mutations (Figures 5G and S10).

Mitochondrial calcium homeostasis is essential for the maintenance of mitochondrial energetic metabolism, with calcium being an essential cofactor of several tricarboxylic acid (TCA) cycle dehydrogenases as well as of some electron transport chain (ETC) complexes, ATP synthase included.[46] Therefore, reduced concentration of mitochondrial calcium contributes to impaired oxidative metabolism and ATP production. Interestingly, patient-derived fibroblasts showed reduced mitochondrial ATP concentrations compared to controls (Figure 5H). However, ATP content is almost completely rescued upon MCU overexpression (Figure 5H). Similarly, the activity of ETC complexes is reduced in patients' cells but restored upon MCU overexpression (Figures 5I–5L), supporting the notion that altered mitochondrial calcium levels account at least in part to the metabolic defect observed in PCARP/HSAN fibroblasts.

Overall, these findings support a previously undescribed role of FLVCR1a in the regulation of ER-mitochondria membrane tethering and mitochondrial calcium transfer through its interaction with the IP3R3-VDAC complex at MAMs.

Loss of *Flvcr1a* in mouse NPCs impairs mitochondrial calcium handling and energetic metabolism

Proper mitochondrial calcium handling and regulation of energetic metabolism are essential for the proliferation of NPCs.[34–38] Interestingly, RNA sequencing analysis underscores deregulation of calcium and mitochondrial energetic metabolism in whole brains from *Flvcr1a*$^{fl/fl}$;NesCRE+ embryos (Figures 6A and S11A). In agreement with these data, we observed a reduction in the activity of ETC complexes, of adenine nucleotide translocase, and in the amount of mitochondrial ATP in whole brain from *Flvcr1a*$^{fl/fl}$;NesCRE+ embryos (Figures S11B–S11D). To investigate whether impaired MAM structure and function contribute to defective CNS development in *Flvcr1a*$^{fl/fl}$;NesCRE+ embryos, NPCs were isolated from E12.5 *Flvcr1a*$^{fl/fl}$;NesCRE+ and *Flvcr1a* $^{fl/+}$;NesCRE+ embryos. MAM integrity was assessed by transmission electron microscopy and showed a reduction in the number and length of contact sites between ER and mitochondria (Figure 6B), confirming that FLVCR1a coordinates ER-mitochondria membrane tethering in NPCs. Moreover, mitochondrial calcium influx was measured upon stimulation with the cholinergic agonist carbachol, which activates phospholipase C to promote phosphoinositide hydrolysis and the production of IP3. We found that calcium influx from ER to mitochondria is severely impaired in *Flvcr1a*$^{fl/fl}$;NesCRE+ NPCs (Figures 6C and 6D). Notably, the expression of FLVCR1a in *Flvcr1a*$^{fl/fl}$;NesCRE+ NPCs partially restored the calcium uptake in mitochondria, while the expression of the mutated FLVCR1a*c160del was not sufficient to recover the phenotype (Figures 6E and 6F). These data highlight the important role of FLVCR1a in the maintenance of MAM integrity and mitochondrial calcium homeostasis in NPCs.

As mitochondrial calcium regulates TCA cycle flux and oxidative phosphorylation, we examined cellular energetic metabolism in NPCs from *Flvcr1a* mutant embryos. The analyses

Figure 4. FLVCR1a regulates ER-mitochondria membrane tethering and ER-mitochondria calcium uptake

(A) Representative immunoblotting showing FLVCR1a protein levels upon FLVCR1a downregulation using short hairpin RNA (shRNA). A scramble shRNA was used as a control.

(B) Quantification of Mander's coefficients (M1 and M2) on confocal images of scramble or *FLVCR1a* shRNA HeLa cells expressing mt-DsRed and sec61-GFP. Superplot quantification showing each analyzed cell (small dot) and the mean of the three independent experiments (big dots). The three independent experiments are depicted with different colors. Data represent mean ± SEM. *n* = 3.

(C) Representative images of scramble or FLVCR1a shRNA HeLa cells expressing mt-DsRed (MITO, red) and sec61-GFP (ER, green). White arrows indicate signal colocalization (ER-mitochondria contact sites).Scale bar: 5 μm.

(D) DAPI staining (blue) and PLA (red dots) on scramble or FLVCR1a shRNA HeLa cells performed with the IP3R3-VDAC antibody pair.

(E) IP3R3-VDAC PLA dot count collected from 5 different 96-wells for each condition. The total dot count was normalized on the number of nuclei in each well. (Non-parametric Mann-Whitney U test; **** = $p < 0.0001$.)

(F) Immunoblotting showing VDAC and IP3R3 protein expression levels in HeLa cells. A representative image is shown. n = 3.

(G) Mitochondrial calcium uptake measured as Ca^{2+} responses to agonist stimulation (100 μM histamine) in HeLa cells expressing a mitochondrial aequorin-based probe. Representative calcium traces are shown.

(H) Quantification of peak mitochondrial calcium amplitude in HeLa cells upon agonist stimulation. Each dot represents the mean of 5 different wells from five independent experiments. Data represent mean ± SEM. *n* = 5.

(I) Mitochondrial calcium elevation following agonist stimulation (histamine) in HeLa cells using a fluorescence resonance energy transfer (FRET)-based probe. The calcium increase is calculated based on FRET efficiency. Each dot represents the FRET efficiency of each cell group analyzed arising from 2 independent replicates. *n*= 2.

(J) Immunoblotting showing FLVCR1a protein levels upon stable overexpression of FLVCR1a or an empty vector. A representative image is shown.

(K) Quantification of Mander's coefficients (M1 and M2) on confocal images of over empty vector of over FLVCR1a-myc HeLa cells expressing mt-DsRed and sec61-GFP. Superplot quantification showing each analyzed cell (small dot) and the mean of the three independent experiments (big dots). Three independent experiments are depicted with different colors. Data represent mean ± SEM. *n* = 3.

(L) Mitochondrial calcium uptake measured as calcium responses to agonist stimulation (100 μM histamine) in HeLa cells expressing a mitochondrial aequorin-based probe. Representative calcium traces are shown.

(M) Quantification of peak mitochondrial calcium amplitude in HeLa cells upon agonist stimulation. Each dot represents the mean of 5 different wells from 3 independent experiments. Data represent mean ± SEM. *n* = 3 (paired t test * = $p < 0.05$; ** = $p < 0.01$; *** = $p < 0.001$; **** = $p < 0.0001$). See also Figure S9.

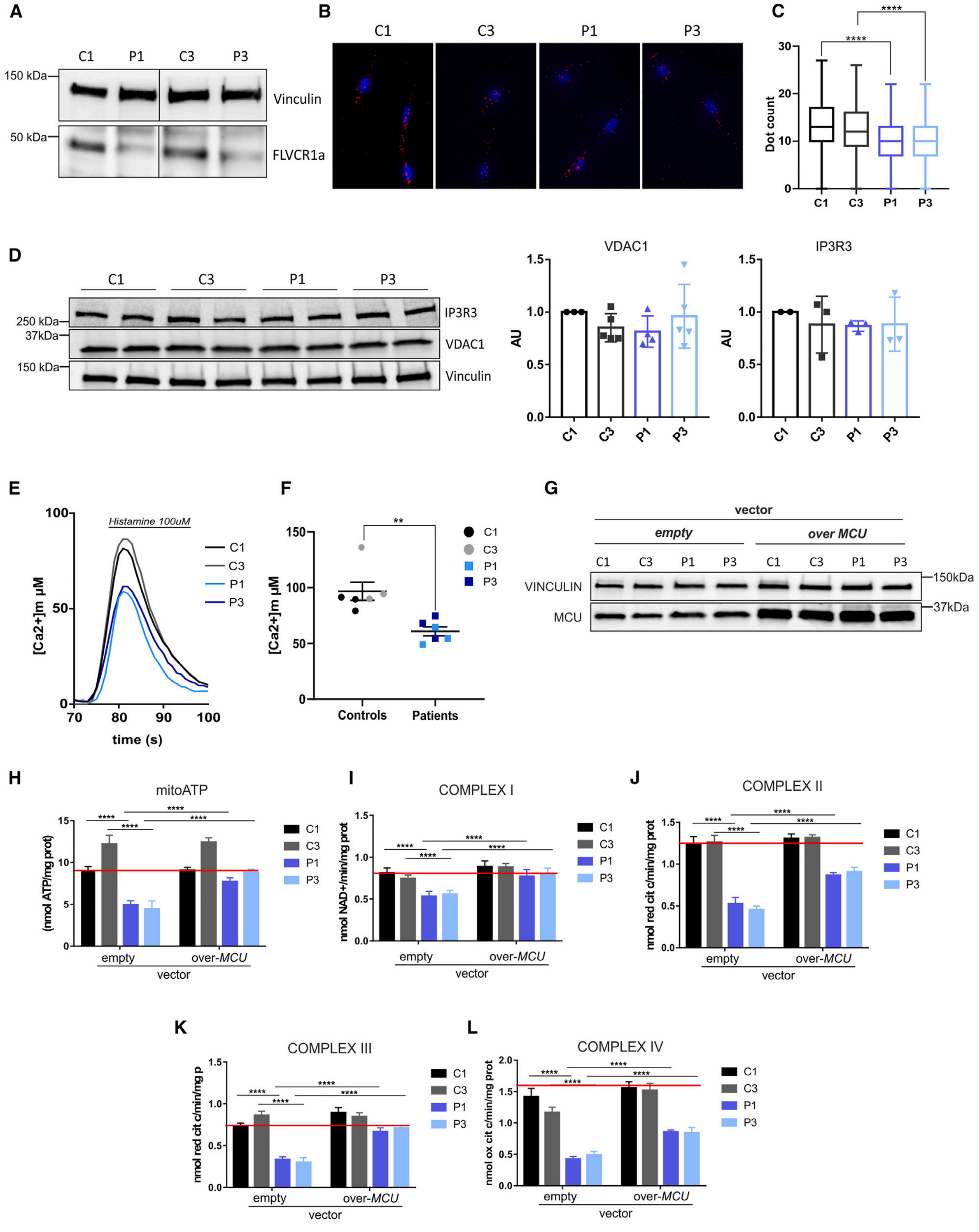

(legend on next page)

showed an overall reduction in energetic metabolism in *Flvcr1a*$^{fl/fl}$;NesCRE+ NPCs when compared to heterozygotes, as indicated by the reduced activity of calcium-dependent TCA cycle dehydrogenases (pyruvate dehydrogenase, isocitrate dehydrogenase, and α-ketoglutarate dehydrogenase) (Figure 6G) and decreased TCA cycle flux (Figure 6H). Futhermore, the activity of ETC complexes was reduced (Figures 6I and 6J), as was the final amount of mitochondrial ATP (Figure 6K).

To confirm that the observed impaired proliferation and the energetic failure in NPCs derived from *Flvcr1a*$^{fl/fl}$;NesCRE+ embryos are, in part, attributed to diminished calcium uptake in mitochondria, we overexpressed MCU (Figure 7A). Significantly, MCU overexpression rescued the proliferation of NPCs lacking Flvcr1a (Figures 7B and 7C). Moreover, the activities of TCA cycle dehydrogenases, ETC complexes, and mitochondrial ATP content exhibited partial rescue upon MCU overexpression (Figures 7D–7F). These data support the hypothesis that dysregulated mitochondrial calcium levels contribute, at least partially, to the metabolic impairment and the subsequent reduced NPC proliferation observed upon Flvcr1a loss during neurodevelopment.

Collectively, these data demonstrate that *Flvcr1a* deficiency in NPCs results in altered mitochondrial calcium homeostasis and impaired mitochondrial activity, which accounts for decreased NPC proliferation, thereby contributing to defective CNS development.

DISCUSSION

We here describe an inactivating homozygous *FLVCR1* mutation in a human fetus with severe CH. Interestingly, variants in *FLVCR1* have been recently described in additional newborns with profound hydrocephalus or microcephaly.[47,48] These case reports, together with the phenotype of *Flvcr1a*$^{fl/fl}$;NesCRE+ embryos, supported the crucial role for FLVCR1a in CH pathogenesis.

Our study improves the current knowledge about FLVCR1a function and its implication in neurological diseases. Initially identified as an essential plasma membrane heme exporter,[8,24,28,30,49–57] recent studies claimed FLVCR1a as a choline importer.[9–13] The definition of FLVCR1a interactome expands the known functions of FLVCR1a by showing its crucial role in the tethering of mitochondria-ER membranes and the regulation of mitochondrial Ca^{2+} fluxes, thus opening fascinating new questions about the physiological roles of this transporter. Besides controlling Ca^{2+} fluxes, mitochondria-ER contact sites emerged as central hubs controlling a multitude of cellular processes, including mitochondrial dynamics, autophagy, and lipid biosynthesis.[58,59] Curiously, mitochondria-ER contact sites have been proposed to be involved in intracellular heme trafficking,[60,61] and choline has been shown to regulate IP3R3 function,[62] suggesting that FLVCR1a may orchestrate a complex interplay between heme, choline, and Ca^{2+} metabolisms. Future studies should be directed to dissect the complex relationship existing between heme, choline, and mitochondrial Ca^{2+} handling and its relevance in pathophysiological conditions.

Our study converges on the notion that FLVCR1a is necessary for neurogenesis by regulating MAM structure and function. Indeed, loss of *Flvcr1a* affected mitochondrial calcium handling and energetic metabolism in NPCs and impaired mouse embryo neurodevelopment. Noteworthy, other proteins essential for NPC proliferation have been reported to regulate mitochondrial calcium levels. Specifically, the protein product of the microcephaly gene MCPH1 interacts with the IP3R3-VDAC complex to sustain calcium influx in mitochondria.[34] Moreover, ARHGAP11b protein, essential for neocortex expansion in humans, interacts with and inhibits the mPTP, blocking calcium release from mitochondria.[35] This cooperation is essential for the proper maintenance of NPC metabolism and proliferation.[63] Our work proposes FLVCR1a as an additional key regulator of NPC function through the modulation of mitochondrial calcium homeostasis and energetic metabolism. FLVCR1a, together with MCPH1 and ARHGAP11B, cooperates to maintain normal calcium homeostasis in mitochondria. When calcium homeostasis is lost, mitochondrial metabolism is compromised together with NPCs function and neocortex development. On a more general note, our data substantiate the notion that mitochondrial dynamics and metabolism exert key roles in neural stem cell maintenance.[38,39] Reduced NPC proliferation appeared to be a pivotal driving mechanism of CH upon *Flvcr1a* loss. Indeed,

Figure 5. Alteration of MAM structure and function in PCARP/HSAN fibroblasts

(A) Representative western blot depicting FLVCR1a abundance in fibroblasts derived from patients with PCARP/HSAN (P1 and P3) and healthy subjects (C1 and C3). Vinculin was used as a loading control.

(B) PLA (red dots) performed in control and patient-derived fibroblasts with the IP3R3-VDAC antibody pair. DAPI (blue) was used to stain the nuclei.

(C)IP3R3-VDAC PLA dot count was collected from five 96-wells for each condition. The total dot count was normalized on the total number of nuclei (Non-parametric Mann-Whitney U test; **** = $p < 0.0001$.).

(D) Immunoblotting of VDAC and IP3R3 proteins in control and patient-derived fibroblasts. Vinculin was used as loading control. Relative quantification of protein abundance. Each dot represents normalized protein abundance of 2 technical replicates of 3 independent experiments. Data represent mean ± SEM. $n = 3$.

(E) Mitochondrial calcium uptake measured as Ca^{2+} responses to agonist stimulation (100 μM histamine) in control and patient-derived fibroblasts. Representative calcium traces are shown.

(F) Quantification of peak mitochondrial calcium amplitude in control and patient-derived fibroblasts upon agonist stimulation. Each dot represents the mean of 5 different wells from 3 independent experiments. Data represent mean ± SEM. $n = 3$ (t test; ** = $p < 0.01$). (G) Immunoblotting showing MCU overexpression in patients and control fibroblasts. Vinculin was used as a loading control.

(H) Quantification of mitochondrial ATP levels in control and patient-derived fibroblasts, under basal conditions or upon MCU overexpression. Results are shown as nmoles ATP/mg of mitochondrial proteins. Data represent means ± SEM, $n = 2$.

(I–L) Activity of the ETC complex I–IV in patient-derived fibroblasts under basal conditions or upon MCU overexpression. Results are shown as nmoles of NAD+/min/mg of mitochondrial protein for complex I, nmoles reduced cytochrome *c*/min/mg of mitochondrial protein for complex II and III, and nmoles oxidized cytochrome *c*/min/mg of mitochondrial protein. Data represent means ± SEM, $n = 2$ (two-way ANOVA; **** = $p < 0.0001$). See also Figure S10.

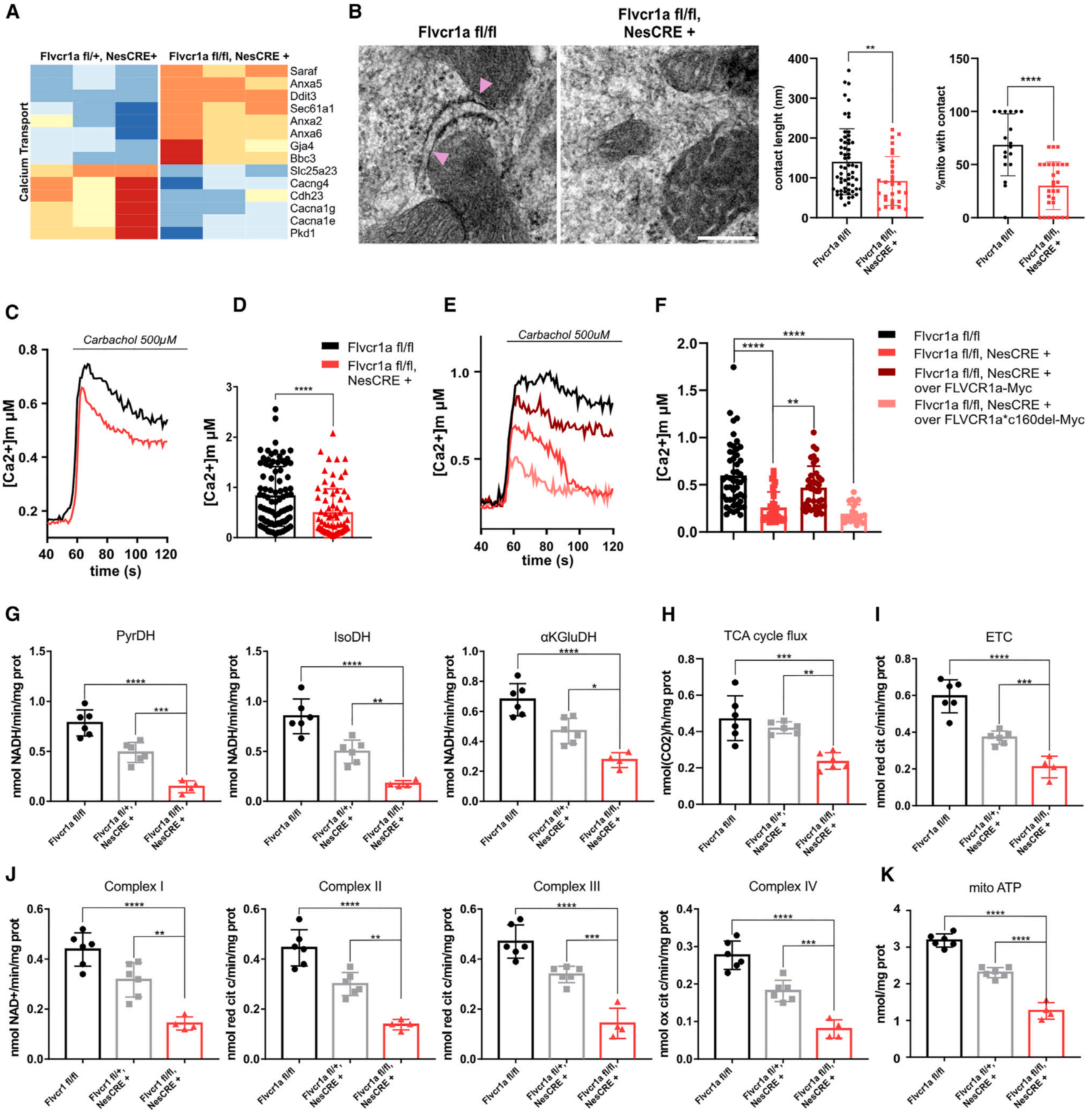

Figure 6. Loss of Flvcr1a in murine NPCs impairs mitochondrial calcium handling and energetic metabolism

(A) RNA sequencing data showing altered expression of genes involved in calcium transport and homeostasis in *Flvcr1a*$^{fl/fl}$;NesCRE+ compared to *Flvcr1a*$^{fl/+}$;NesCRE+ E14.5 brains.

(B) Transmission electron microscopy images from *Flvcr1a*$^{fl/fl}$;NesCRE+ compared to *Flvcr1a*$^{fl/fl}$ NPCs. Pink arrows show ER-mitochondria contacts. Quantification of contact lengths and number is shown. Data represent mean ± SD. (t test; ** = $p < 0.01$).

(C) Mitochondrial calcium uptake measured as Ca^{2+} responses to agonist stimulation (500 μM carbachol) in *Flvcr1a*$^{fl/fl}$;NesCRE+ and *Flvcr1a*$^{fl/fl}$ NPCs. The mito-GEM-GECO1 probe was used. Representative Ca^{2+} traces are shown.

(D) Quantification of peak mitochondrial Ca^{2+} amplitude upon agonist stimulation. Each dot represents the peak amplitude of single cells from 3 independent experiments. Data represent mean ± SEM. $n = 3$ (t test; ** = $p < 0.01$).

(E) Mitochondrial calcium uptake measured as Ca^{2+} responses to agonist stimulation (500 μM carbachol) in *Flvcr1a*$^{fl/fl}$ NPCs overexpressing an empty vector and *Flvcr1a*$^{fl/fl}$;NesCRE+ NPCs overexpressing an empty vector, FLVCR1a-myc, or FLVCR1a*c.160del protein. The mito-GEM-GECO1 probe was used. Representative Ca^{2+} traces are shown.

(legend continued on next page)

loss of *Flvcr1a* caused premature differentiation of NPCs at the expense of NPC maintenance, leading to an overall reduction in cortex thickness. As recently demonstrated, cortical hypoplasia can affect brain biomechanics and its ability to resist mechanical strain, resulting in a secondary expansion of ventricles in the absence of a primary defect in CSF dynamics.[6] Thus, our results corroborate the neuroprogenitor-based paradigm of CH.[6,7]

Altogether, these observations sustain the notion that the alteration of mitochondrial calcium handling and energetic metabolism can lead to both microcephaly and CH. These two apparently opposite disorders are not mutually exclusive. Studies have shown that ventriculomegaly can be a secondary complication of microcephaly.[6] Furthermore, genetic and computational studies showed a genetic overlap between CH and microcephaly,[6,7] thus suggesting the existence of common molecular mechanisms.

Emerging evidence sustains that the alteration of calcium homeostasis might be an important mechanism contributing to different forms of CH. Mutations in phosphatidylinositol-4,5-bisphosphate 3-kinase catalytic subunit alpha (*PIK3CA*), phosphatase and tensin homolog (*PTEN*), and mechanistic target of rapamycin kinase (*MTOR*) have been recently identified in a subset of patients with sporadic CH,[7] and studies in animal models support a role for PI3K signaling during neurogenesis. As PI3K participates in the control of calcium handling by regulating the phosphorylation of IP3R3, we can speculate that calcium dysregulation can contribute to the pathogenesis of these specific subtypes of CH. It is also worth noting that FLVCR2, responsible for CH in both humans and mice,[64–66] was discovered to interact with the calcium transporter sarcoplasmic/endoplasmic reticulum Ca^{2+}-ATPase (SERCA).[67] Taken together, these observations suggest that alteration of mitochondrial calcium homeostasis may have a broader than expected impact on CH pathogenesis.

Our study improves the understanding of the molecular pathogenesis of CH, highlighting dysregulated calcium homeostasis as a new pathogenetic mechanism in CH. Furthermore, our results provide important cues for the comprehension of PCARP/HSAN originating from partially inactivating mutations in *FLVCR1*. The alteration of MAM structure and function observed in patients' fibroblasts suggest that alteration of calcium handling might contribute to PCARP/HSAN pathogenesis. Supporting this concept, mutations in *IP3R3* have been found in patients with Charcot-Marie-Tooth disorder, a motor neuropathy.[68] Moreover, alterations in proteins regulating organelle-membrane shaping,[69] ER-mitochondria contact sites, and mitochondrial calcium handling have been described as underlying determinants of hereditary neuropathies.[70,71] As enhancers of calcium uptake in mitochondria already exist and are currently used in clinics to treat several neurological disorders,[72] our work also puts forward the development of new treatments for these rare neurological diseases.

Limitations of the study

The interaction between FLVCR1a and the IP3R3-VDAC complex raises crucial inquiries regarding the mechanisms through which this interplay occurs. Our study suggests that a certain amount of FLVCR1a may reside at MAMs, allowing the interaction with the IP3R3-VDAC complex. However, the separation of MAMs from the plasma membrane, where FLVCR1a is highly expressed, is challenging as confirmed by the residual expression of a plasma membrane protein ORAI in our MAM fractions. This is due to the dynamic interaction between the plasma membrane and the ER or mitochondria.[73,74] Therefore, we cannot exclude the existence of dynamic interactions between plasma membrane-localized FLVCR1a and the MAM-localized IP3R3-VDAC complex. Immunoelectron microscopy will be necessary to figure out the mode of interaction between these proteins. Finally, this study did not investigate the potential role of FLVCR1b nor the contribution of heme and choline metabolism to the proposed mechanism leading to CH.

STAR★METHODS

Detailed methods are provided in the online version of this paper and include the following:

- KEY RESOURCES TABLE
- RESOURCE AVAILABILITY
    - ○ Lead contact
    - ○ Materials availability
    - ○ Data and code availability
- EXPERIMENTAL MODEL AND SUBJECT DETAILS
    - ○ Ethic statement
    - ○ Human fetus carrying *FLVCR1* mutations

(F) Quantification of peak mitochondrial Ca^{2+} amplitude upon agonist stimulation. Each dot represents the peak amplitude of a single cell from two independent experiments. Data represent mean ± SEM. $n = 2$ (one-way ANOVA; ** = $p < 0.01$, **** = $p < 0.0001$).

(G) Activity of the pyruvate, isocitrate, and α-ketoglutarate dehydrogenases in NPCs isolated from *Flvcr1a*$^{fl/fl}$;NesCRE+, *Flvcr1a*$^{fl/+}$;NesCRE+, and *Flvcr1a*$^{fl/fl}$ embryos. Results are expressed as nmoles NADH/min/mg of mitochondrial protein. Each dot represents a single replicate of 3 different replicates of 2 independent experiments. Data represent mean ± SEM. $n = 2$.

(H) TCA cycle flux is expressed as pmol CO_2/h/mg of protein. Data represent mean ± SEM. $n = 2$.

(I) Overall ETC activity in NPCs isolated from *Flvcr1a*$^{fl/fl}$;NesCRE+, *Flvcr1a*$^{fl/+}$;NesCRE+, and *Flvcr1a*$^{fl/fl}$ embryos. Results are shown as nmoles reduced cytochrome *c*/min/mg of mitochondrial protein. Each dot represents a single replicate of 3 different replicates of 2 independent experiments. Data represent mean ± SEM. $n = 2$.

(J) Activity of the different mitochondrial ETC complexes in NPCs isolated from *Flvcr1a*$^{fl/fl}$;NesCRE+, and *Flvcr1a*$^{fl/+}$;NesCRE+ and *Flvcr1a*$^{fl/fl}$ embryos. Results are shown as nmoles of NAD+/min/mg of mitochondrial protein for complex I, nmoles reduced cytochrome *c*/min/mg of mitochondrial protein for complex II and III, and nmoles oxidized cytochrome *c*/min/mg of mitochondrial protein. Each dot represents a single replicate of 3 different replicates of 2 independent experiments. Data represent mean ± SEM. $n = 2$.

(K) Quantification of mitochondrial ATP levels in NPCs isolated from *Flvcr1a*$^{fl/fl}$;NesCRE+ and *Flvcr1a*$^{fl/+}$;NesCRE+ and *Flvcr1a*$^{fl/fl}$ embryos. Results are shown as nmoles ATP/mg of mitochondrial proteins. Each dot represents a single replicate of 3 different replicates of 2 independent experiments. Data represent mean ± SEM. $n = 2$ (one-Way ANOVA; * = $p < 0.05$; ** = $p < 0.01$; *** = $p < 0.001$; **** = $p < 0.0001$). See also Figure S11.

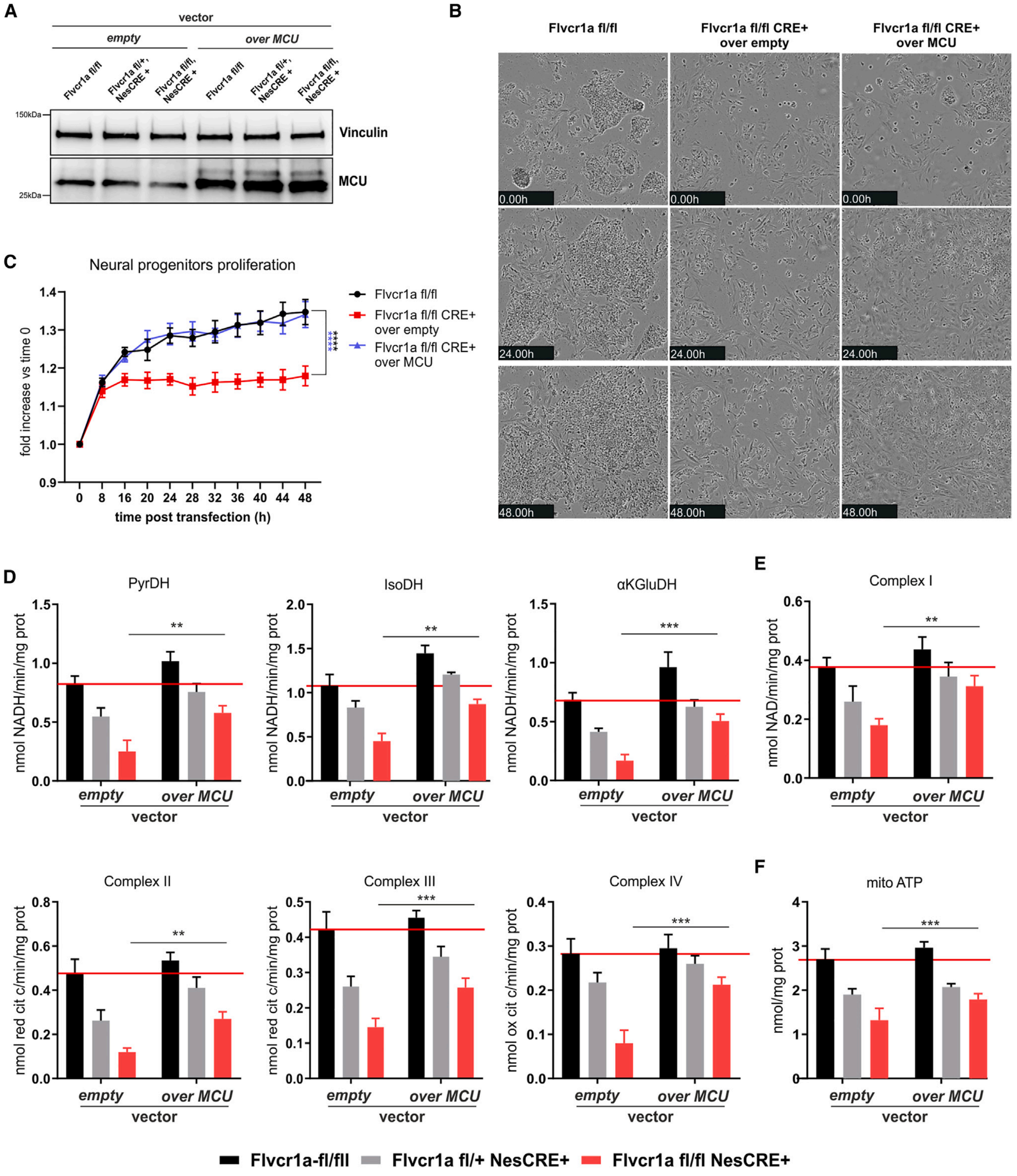

Figure 7. Mitochondrial calcium restoration improves *Flvcr1a*$^{fl/fl}$-NesCRE+ NPC proliferation and metabolism

(A) Immunoblotting showing MCU overexpression in *Flvcr1a*$^{fl/fl}$;NesCRE+, *Flvcr1a*$^{fl/+}$;NesCRE+, and *Flvcr1a*$^{fl/fl}$ NPCs. Vinculin was used as a loading control.

(B) Representative images of *Flvcr1a*$^{fl/fl}$ NPCs overexpressing an empty vector and *Flvcr1a*$^{fl/fl}$;NesCRE+ NPCs overexpressing an empty vector or MCU. NPC proliferation was measured for 48 h post-transfection using Incucyte SX5 Live-Cell Analysis.

(C) Proliferation rate of *Flvcr1a*$^{fl/fl}$ NPCs overexpressing an empty vector and *Flvcr1a*$^{fl/fl}$;NesCRE+ NPCs overexpressing an empty vector or MCU. Each time point represents the mean ± SEM of 5 different biological replicates (two-way ANOVA; **** = $p < 0.0001$).

(legend continued on next page)

  - ○ Fetal human tissues for immunostaining
  - ○ PCARP/HSAN patient-derived primary fibroblasts culture
  - ○ Mouse model
  - ○ Murine embryonic neocortical neuroprogenitor cell (NPC) primary cultures
  - ○ Cell lines
- METHOD DETAILS
  - ○ Whole exome sequencing
  - ○ Fetal human tissues immunostaining
  - ○ “Flashtag” *in utero* injections
  - ○ FACS
  - ○ Quantitative real-time PCR analysis (qPCR)
  - ○ PCR
  - ○ Micro computed tomography (Micro-CT)
  - ○ Histological analysis
  - ○ Immunofluorescence analysis on mouse tissues
  - ○ Edu staining
  - ○ TUNEL assay
  - ○ RNA sequencing
  - ○ FLVCR1 scRNA-seq differential expression analysis
  - ○ NPCs proliferation
  - ○ Tandem affinity purification (TAP)
  - ○ Preparation of pulldown samples for proteomic analysis
  - ○ Mass spectrometry analysis
  - ○ Mass spectrometry data analysis
  - ○ Subcellular fractionation
  - ○ Immunofluorescence analyses on cell cultures
  - ○ Proximity ligation assay (PLA)
  - ○ Cell transient transfections and plasmids
  - ○ Gene silencing and overexpression
  - ○ Immunoprecipitation
  - ○ Western blotting
  - ○ Endoplasmic reticulum (ER) - mitochondria contact sites measurement
  - ○ Aequorin based calcium measurements
  - ○ FRET based calcium measurement
  - ○ Calcein/Co2+ quenching assays
  - ○ Mitochondrial extraction and electron transport chain (ETC) activity
  - ○ Activity of each ETC complexes
  - ○ Adenine nucleotide translocase (ANT) activity
  - ○ Pyruvate dehydrogenase, a-ketoglutarate dehydrogenase, isocitrate dehydrogenase activities
  - ○ Mitochondrial ATP levels
  - ○ Transmission electron ultrastructural analysis
  - ○ Embryonic NPC calcium imaging and quantification
- QUANTIFICATION AND STATISTICAL ANALYSIS

SUPPLEMENTAL INFORMATION

Supplemental information can be found online at https://doi.org/10.1016/j.xcrm.2024.101647.

ACKNOWLEDGMENTS

We acknowledge Marta Gai and the Open Lab of Advance Microscopy (OLMA@MBC) for technical assistance. We thank Vicente Pedrozo for his excellent technical assistance with the dissections for the isolation of “Flash-Tag”-labeled cells.

This work was supported by the National Institutes of Health (1R01NS123168-01 to T.A., E.T., and D. Chiabrando), Fondazione Telethon ETS (GMR22T1076 to D. Chiabrando), and PRIN (2022PX3SR3 to D. Chiabrando). We are thankful for the generous support from NIH R01MH125004 and the UCSF Program for Breakthrough Biomedical Research, Sandler Foundation (to G.P.) and funding from Compagnia di San Paolo, Italy (EX-POST 2021 funding to C.R.). Parts of this study were financed in the framework of the NME-GPS project by the European Regional Development Fund (ERDF; to A.R. and A.H.). The graphical abstract for this paper was created with BioRender (https://www.biorender.com).

AUTHOR CONTRIBUTIONS

Conceptualization, F.B., D. Chiabrando, and E.T.; methodology, F.B., D. Chiabrando, D.M., M.B., J.N., and N.S.; investigation, F.B., D. Chiabrando, D.M., M.B., J.N., L. Metani, D.I.Z.V., D. Chianese, N.S., I.C.S., A.H., E.Q., T.G., A.A.M., E.D., G. Allington, F. Maier, M.S., K.-P.G., G.P., C.R., C.B., E.S., D.P., M.d.R., and A.R.; writing – original draft, F.B. and D. Chiabrando; writing – review and editing, F.B., D. Chiabrando, G.P., V.F., G. Ammirata, K.T.K., P.G., P.P.P., A.L.A., S.P., F.D.G., L. Munaron, F. Mussano, C.B., and F.A.; supervision, D. Chiabrando, E.T., and M.B.; project administration, D. Chiabrando and E.T.; funding acquisition, D. Chiabrando, E.T., T.A., C.R., G.P., A.R., and A.H.

DECLARATION OF INTERESTS

E.T., V.F., D.Chiabrando, S.P., F.B., and A.L.A. are inventors in a patent filed by the University of Torino, not related to the research reported here.

Received: July 24, 2023
Revised: March 20, 2024
Accepted: June 16, 2024
Published: July 16, 2024

REFERENCES

1. Kahle, K.T., Kulkarni, A.V., Limbrick, D.D., and Warf, B.C. (2016). Hydrocephalus in children. Lancet *387*, 788–799. https://doi.org/10.1016/S0140-6736(15)60694-8.
2. Persson, E.K., Hagberg, G., and Uvebrant, P. (2006). Disabilities in children with hydrocephalus–a population-based study of children aged between four and twelve years. Neuropediatrics *37*, 330–336. https://doi.org/10.1055/s-2007-964868.
3. De Backer, A. (2016). Handbook of neurosurgery, 8th edition. Acta Chir. Belg. *116*, 269. https://doi.org/10.1080/00015458.2016.1229422.
4. Duy, P.Q., Rakic, P., Alper, S.L., Robert, S.M., Kundishora, A.J., Butler, W.E., Walsh, C.A., Sestan, N., Geschwind, D.H., Jin, S.C., and Kahle, K.T. (2023). A neural stem cell paradigm of pediatric hydrocephalus. Cereb. Cortex *33*, 4262–4279. https://doi.org/10.1093/cercor/bhac341.
5. Kousi, M., and Katsanis, N. (2016). The Genetic Basis of Hydrocephalus. Annu. Rev. Neurosci. *39*, 409–435. https://doi.org/10.1146/annurev-neuro-070815-014023.
6. Duy, P.Q., Weise, S.C., Marini, C., Li, X.J., Liang, D., Dahl, P.J., Ma, S., Spajic, A., Dong, W., Juusola, J., et al. (2022). Impaired neurogenesis

(D) Activity of the pyruvate, isocitrate, and α-ketoglutarate dehydrogenases in $Flvcr1a^{fl/fl}$;NesCRE+, Flvcr1a$^{fl/+}$;NesCRE+ and Flvcr1a$^{fl/fl}$ NPCs overexpressing an empty vector or MCU. Results are expressed as nmoles NADH/min/mg of mitochondrial protein. Data represent means ± SEM, $n = 2$.
(E) Activity of the ETC complexes in $Flvcr1a^{fl/fl}$;NesCRE+, Flvcr1a$^{fl/+}$;NesCRE+, and Flvcr1a$^{fl/fl}$ NPCs overexpressing an empty vector or MCU. Results are shown as nmoles of NAD+/min/mg of mitochondrial protein for complex I, nmoles reduced cytochrome *c*/min/mg of mitochondrial protein for complex II and III, and nmoles oxidized cytochrome *c*/min/mg of mitochondrial protein. Data represent means ± SEM, $n = 2$.
(F) Quantification of mitochondrial ATP levels in $Flvcr1a^{fl/fl}$;NesCRE+, $Flvcr1a^{fl/+}$;NesCRE+, and Flvcr1a$^{fl/fl}$ NPCs overexpressing an empty vector or MCU. Results are shown as nmoles ATP/mg of mitochondrial proteins. Data represent means ± SEM, $n = 2$ (two-way ANOVA; * = $p < 0.05$; ** = $p < 0.01$; *** = $p < 0.001$; **** = $p < 0.0001$).

alters brain biomechanics in a neuroprogenitor-based genetic subtype of congenital hydrocephalus. Nat. Neurosci. *25*, 458–473. https://doi.org/10.1038/s41593-022-01043-3.

7. Jin, S.C., Dong, W., Kundishora, A.J., Panchagnula, S., Moreno-De-Luca, A., Furey, C.G., Allocco, A.A., Walker, R.L., Nelson-Williams, C., Smith, H., et al. (2020). Exome sequencing implicates genetic disruption of prenatal neuro-gliogenesis in sporadic congenital hydrocephalus. Nat. Med. *26*, 1754–1765. https://doi.org/10.1038/s41591-020-1090-2.
8. Quigley, J.G., Yang, Z., Worthington, M.T., Phillips, J.D., Sabo, K.M., Sabath, D.E., Berg, C.L., Sassa, S., Wood, B.L., and Abkowitz, J.L. (2004). Identification of a human heme exporter that is essential for erythropoiesis. Cell *118*, 757–766. https://doi.org/10.1016/j.cell.2004.08.014.
9. Ri, K., Weng, T.H., Claveras Cabezudo, A., Jösting, W., Zhang, Y., Bazzone, A., Leong, N.C.P., Welsch, S., Doty, R.T., Gursu, G., et al. (2024). Molecular mechanism of choline and ethanolamine transport in humans. Nature *630*, 501–508. https://doi.org/10.1038/s41586-024-07444-7.
10. Son, Y., Kenny, T.C., Khan, A., Birsoy, K., and Hite, R.K. (2024). Structural basis of lipid head group entry to the Kennedy pathway by FLVCR1. Nature *629*, 710–716. https://doi.org/10.1038/s41586-024-07374-4.
11. Ha, H.T.T., Sukumar, V.K., Chua, J.W.B., Nguyen, D.T., Nguyen, T.Q., Lim, L.H.K., Cazenave-Gassiot, A., and Nguyen, L.N. (2023). Mfsd7b facilitates choline transport and missense mutations affect choline transport function. Cell. Mol. Life Sci. *81*, 3. https://doi.org/10.1007/s00018-023-05048-4.
12. Kenny, T.C., Khan, A., Son, Y., Yue, L., Heissel, S., Sharma, A., Pasolli, H.A., Liu, Y., Gamazon, E.R., Alwaseem, H., et al. (2023). Integrative genetic analysis identifies FLVCR1 as a plasma-membrane choline transporter in mammals. Cell Metabol. *35*, 1057–1071.e12. https://doi.org/10.1016/j.cmet.2023.04.003.
13. Tsuchiya, M., Tachibana, N., Nagao, K., Tamura, T., and Hamachi, I. (2023). Organelle-selective click labeling coupled with flow cytometry allows pooled CRISPR screening of genes involved in phosphatidylcholine metabolism. Cell Metabol. *35*, 1072–1083.e9. https://doi.org/10.1016/j.cmet.2023.02.014.
14. Giorgi, C., Marchi, S., and Pinton, P. (2018). The machineries, regulation and cellular functions of mitochondrial calcium. Nat. Rev. Mol. Cell Biol. *19*, 713–730. https://doi.org/10.1038/s41580-018-0052-8.
15. Richards, S., Aziz, N., Bale, S., Bick, D., Das, S., Gastier-Foster, J., Grody, W.W., Hegde, M., Lyon, E., Spector, E., et al. (2015). Standards and guidelines for the interpretation of sequence variants: a joint consensus recommendation of the American College of Medical Genetics and Genomics and the Association for Molecular Pathology. Genet. Med. *17*, 405–424. https://doi.org/10.1038/gim.2015.30.
16. Rajadhyaksha, A.M., Elemento, O., Puffenberger, E.G., Schierberl, K.C., Xiang, J.Z., Putorti, M.L., Berciano, J., Poulin, C., Brais, B., Michaelides, M., et al. (2010). Mutations in FLVCR1 cause posterior column ataxia and retinitis pigmentosa. Am. J. Hum. Genet. *87*, 643–654. https://doi.org/10.1016/j.ajhg.2010.10.013.
17. Shaibani, A., Wong, L.J., Wei Zhang, V., Lewis, R.A., and Shinawi, M. (2015). Autosomal recessive posterior column ataxia with retinitis pigmentosa caused by novel mutations in the FLVCR1 gene. Int. J. Neurosci. *125*, 43–49. https://doi.org/10.3109/00207454.2014.904858.
18. Yanatori, I., Yasui, Y., Miura, K., and Kishi, F. (2012). Mutations of FLVCR1 in posterior column ataxia and retinitis pigmentosa result in the loss of heme export activity. Blood Cells Mol. Dis. *49*, 60–66. https://doi.org/10.1016/j.bcmd.2012.03.004.
19. Ishiura, H., Fukuda, Y., Mitsui, J., Nakahara, Y., Ahsan, B., Takahashi, Y., Ichikawa, Y., Goto, J., Sakai, T., and Tsuji, S. (2011). Posterior column ataxia with retinitis pigmentosa in a Japanese family with a novel mutation in FLVCR1. Neurogenetics *12*, 117–121. https://doi.org/10.1007/s10048-010-0271-4.
20. Bertino, F., Firestone, K., Bellacchio, E., Jackson, K.E., Asamoah, A., Hersh, J., Fiorito, V., Destefanis, F., Gonser, R., Tucker, M.E., et al. (2019). Heme and sensory neuropathy: insights from novel mutations in the heme exporter Feline Leukemia Virus subgroup C Receptor 1. Pain *160*, 2766–2775. https://doi.org/10.1097/j.pain.0000000000001675.
21. Castori, M., Morlino, S., Ungelenk, M., Pareyson, D., Salsano, E., Grammatico, P., Tolosano, E., Kurth, I., and Chiabrando, D. (2017). Posterior column ataxia with retinitis pigmentosa coexisting with sensory-autonomic neuropathy and leukemia due to the homozygous p.Pro221Ser FLVCR1 mutation. Am. J. Med. Genet. B Neuropsychiatr. Genet. *174*, 732–739. https://doi.org/10.1002/ajmg.b.32570.
22. Chiabrando, D., Castori, M., di Rocco, M., Ungelenk, M., Gießelmann, S., Di Capua, M., Madeo, A., Grammatico, P., Bartsch, S., Hübner, C.A., et al. (2016). Mutations in the Heme Exporter FLVCR1 Cause Sensory Neurodegeneration with Loss of Pain Perception. PLoS Genet. *12*, e1006461. https://doi.org/10.1371/journal.pgen.1006461.
23. Lischka, A., Eggermann, K., Record, C.J., Dohrn, M.F., Laššuthová, P., Kraft, F., Begemann, M., Dey, D., Eggermann, T., Beijer, D., et al. (2023). Genetic landscape of congenital insensitivity to pain and hereditary sensory and autonomic neuropathies. Brain *146*, 4880–4890. https://doi.org/10.1093/brain/awad328.
24. Chiabrando, D., Marro, S., Mercurio, S., Giorgi, C., Petrillo, S., Vinchi, F., Fiorito, V., Fagoonee, S., Camporeale, A., Turco, E., et al. (2012). The mitochondrial heme exporter FLVCR1b mediates erythroid differentiation. J. Clin. Invest. *122*, 4569–4579. https://doi.org/10.1172/JCI62422.
25. Tailor, C.S., Willett, B.J., and Kabat, D. (1999). A putative cell surface receptor for anemia-inducing feline leukemia virus subgroup C is a member of a transporter superfamily. J. Virol. *73*, 6500–6505.
26. Fietz, S.A., Lachmann, R., Brandl, H., Kircher, M., Samusik, N., Schröder, R., Lakshmanaperumal, N., Henry, I., Vogt, J., Riehn, A., et al. (2012). Transcriptomes of germinal zones of human and mouse fetal neocortex suggest a role of extracellular matrix in progenitor self-renewal. Proc. Natl. Acad. Sci. USA *109*, 11836–11841. https://doi.org/10.1073/pnas.1209647109.
27. Pollen, A.A., Nowakowski, T.J., Chen, J., Retallack, H., Sandoval-Espinosa, C., Nicholas, C.R., Shuga, J., Liu, S.J., Oldham, M.C., Diaz, A., et al. (2015). Molecular identity of human outer radial glia during cortical development. Cell *163*, 55–67. https://doi.org/10.1016/j.cell.2015.09.004.
28. Petrillo, S., De Giorgio, F., Bertino, F., Garello, F., Bitonto, V., Longo, D.L., Mercurio, S., Ammirata, G., Allocco, A.L., Fiorito, V., et al. (2023). Endothelial cells require functional FLVCR1a during developmental and adult angiogenesis. Angiogenesis *26*, 365–384. https://doi.org/10.1007/s10456-023-09865-w.
29. Govindan, S., Oberst, P., and Jabaudon, D. (2018). In vivo pulse labeling of isochronic cohorts of cells in the central nervous system using FlashTag. Nat. Protoc. *13*, 2297–2311. https://doi.org/10.1038/s41596-018-0038-1.
30. Vinchi, F., Ingoglia, G., Chiabrando, D., Mercurio, S., Turco, E., Silengo, L., Altruda, F., and Tolosano, E. (2014). Heme exporter FLVCR1a regulates heme synthesis and degradation and controls activity of cytochromes P450. Gastroenterology *146*, 1325–1338. https://doi.org/10.1053/j.gastro.2014.01.053.
31. Shimada, I.S., Acar, M., Burgess, R.J., Zhao, Z., and Morrison, S.J. (2017). Prdm16 is required for the maintenance of neural stem cells in the postnatal forebrain and their differentiation into ependymal cells. Genes Dev. *31*, 1134–1146. https://doi.org/10.1101/gad.291773.116.
32. Roy, A., Murphy, R.M., Deng, M., MacDonald, J.W., Bammler, T.K., Aldinger, K.A., Glass, I.A., and Millen, K.J. (2019). PI3K-Yap activity drives cortical gyrification and hydrocephalus in mice. Elife *8*, e45961. https://doi.org/10.7554/eLife.45961.
33. Janikiewicz, J., Szymański, J., Malinska, D., Patalas-Krawczyk, P., Michalska, B., Duszyński, J., Giorgi, C., Bonora, M., Dobrzyn, A., and Wieckowski, M.R. (2018). Mitochondria-associated membranes in aging and senescence: structure, function, and dynamics. Cell Death Dis. *9*, 332. https://doi.org/10.1038/s41419-017-0105-5.
34. Journiac, N., Gilabert-Juan, J., Cipriani, S., Benit, P., Liu, X., Jacquier, S., Faivre, V., Delahaye-Duriez, A., Csaba, Z., Hourcade, T., et al. (2020). Cell

Metabolic Alterations due to Mcph1 Mutation in Microcephaly. Cell Rep. *31*, 107506. https://doi.org/10.1016/j.celrep.2020.03.070.

35. Namba, T., Dóczi, J., Pinson, A., Xing, L., Kalebic, N., Wilsch-Bräuninger, M., Long, K.R., Vaid, S., Lauer, J., Bogdanova, A., et al. (2020). Human-Specific ARHGAP11B Acts in Mitochondria to Expand Neocortical Progenitors by Glutaminolysis. Neuron *105*, 867–881.e869. https://doi.org/10.1016/j.neuron.2019.11.027.
36. Iwata, R., and Vanderhaeghen, P. (2021). Regulatory roles of mitochondria and metabolism in neurogenesis. Curr. Opin. Neurobiol. *69*, 231–240. https://doi.org/10.1016/j.conb.2021.05.003.
37. Iwata, R., Casimir, P., and Vanderhaeghen, P. (2020). Mitochondrial dynamics in postmitotic cells regulate neurogenesis. Science *369*, 858–862. https://doi.org/10.1126/science.aba9760.
38. Khacho, M., Clark, A., Svoboda, D.S., Azzi, J., MacLaurin, J.G., Meghaizel, C., Sesaki, H., Lagace, D.C., Germain, M., Harper, M.E., et al. (2016). Mitochondrial Dynamics Impacts Stem Cell Identity and Fate Decisions by Regulating a Nuclear Transcriptional Program. Cell Stem Cell *19*, 232–247. https://doi.org/10.1016/j.stem.2016.04.015.
39. Fame, R.M., and Lehtinen, M.K. (2021). Mitochondria in Early Forebrain Development: From Neurulation to Mid-Corticogenesis. Front Cell Dev. Biol. *9*, 780207. https://doi.org/10.3389/fcell.2021.780207.
40. Bonora, M., Giorgi, C., Bononi, A., Marchi, S., Patergnani, S., Rimessi, A., Rizzuto, R., and Pinton, P. (2013). Subcellular calcium measurements in mammalian cells using jellyfish photoprotein aequorin-based probes. Nat. Protoc. *8*, 2105–2118. https://doi.org/10.1038/nprot.2013.127.
41. Rizzuto, R., Pinton, P., Carrington, W., Fay, F.S., Fogarty, K.E., Lifshitz, L.M., Tuft, R.A., and Pozzan, T. (1998). Close contacts with the endoplasmic reticulum as determinants of mitochondrial Ca2+ responses. Science *280*, 1763–1766. https://doi.org/10.1126/science.280.5370.1763.
42. Li, H., Ding, X., Lopez, J.R., Takeshima, H., Ma, J., Allen, P.D., and Eltit, J.M. (2010). Impaired Orai1-mediated resting Ca2+ entry reduces the cytosolic [Ca2+] and sarcoplasmic reticulum Ca2+ loading in quiescent junctophilin 1 knock-out myotubes. J. Biol. Chem. *285*, 39171–39179. https://doi.org/10.1074/jbc.M110.149690.
43. Jozsef, L., Tashiro, K., Kuo, A., Park, E.J., Skoura, A., Albinsson, S., Rivera-Molina, F., Harrison, K.D., Iwakiri, Y., Toomre, D., and Sessa, W.C. (2014). Reticulon 4 is necessary for endoplasmic reticulum tubulation, STIM1-Orai1 coupling, and store-operated calcium entry. J. Biol. Chem. *289*, 9380–9395. https://doi.org/10.1074/jbc.M114.548602.
44. Bonora, M., Morganti, C., Morciano, G., Giorgi, C., Wieckowski, M.R., and Pinton, P. (2016). Comprehensive analysis of mitochondrial permeability transition pore activity in living cells using fluorescence-imaging-based techniques. Nat. Protoc. *11*, 1067–1080. https://doi.org/10.1038/nprot.2016.064.
45. Petronilli, V., Miotto, G., Canton, M., Brini, M., Colonna, R., Bernardi, P., and Di Lisa, F. (1999). Transient and long-lasting openings of the mitochondrial permeability transition pore can be monitored directly in intact cells by changes in mitochondrial calcein fluorescence. Biophys. J. *76*, 725–734. https://doi.org/10.1016/S0006-3495(99)77239-5.
46. Bonora, M., Patergnani, S., Rimessi, A., De Marchi, E., Suski, J.M., Bononi, A., Giorgi, C., Marchi, S., Missiroli, S., Poletti, F., et al. (2012). ATP synthesis and storage. Purinergic Signal. *8*, 343–357. https://doi.org/10.1007/s11302-012-9305-8.
47. Safwat, S., Flannery, K.P., El Beheiry, A.A., Mokhtar, M.M., Abdalla, E., and Manzini, M.C. (2024). Genetic blueprint of congenital muscular dystrophies with brain malformations in Egypt: A report of 11 families. Neurogenetics *25*, 93–102. https://doi.org/10.1007/s10048-024-00745-z.
48. AlAbdi, L., Shamseldin, H.E., Khouj, E., Helaby, R., Aljamal, B., Alqahtani, M., Almulhim, A., Hamid, H., Hashem, M.O., Abdulwahab, F., et al. (2023). Beyond the exome: utility of long-read whole genome sequencing in exome-negative autosomal recessive diseases. Genome Med. *15*, 114. https://doi.org/10.1186/s13073-023-01270-8.
49. Keel, S.B., Doty, R.T., Yang, Z., Quigley, J.G., Chen, J., Knoblaugh, S., Kingsley, P.D., De Domenico, I., Vaughn, M.B., Kaplan, J., et al. (2008). A heme export protein is required for red blood cell differentiation and iron homeostasis. Science *319*, 825–828. https://doi.org/10.1126/science.1151133.
50. Byon, J.C.H., Chen, J., Doty, R.T., and Abkowitz, J.L. (2013). FLVCR is necessary for erythroid maturation, may contribute to platelet maturation, but is dispensable for normal hematopoietic stem cell function. Blood *122*, 2903–2910. https://doi.org/10.1182/blood-2012-10-465104.
51. Philip, M., Funkhouser, S.A., Chiu, E.Y., Phelps, S.R., Delrow, J.J., Cox, J., Fink, P.J., and Abkowitz, J.L. (2015). Heme exporter FLVCR is required for T cell development and peripheral survival. J. Immunol. *194*, 1677–1685. https://doi.org/10.4049/jimmunol.1402172.
52. Fiorito, V., Forni, M., Silengo, L., Altruda, F., and Tolosano, E. (2015). Crucial role of Flvcr1a in the maintenance of intestinal heme homeostasis. Antioxidants Redox Signal. *23*, 1410–1423. https://doi.org/10.1089/ars.2014.6216.
53. Mercurio, S., Petrillo, S., Chiabrando, D., Bassi, Z.I., Gays, D., Camporeale, A., Vacaru, A., Miniscalco, B., Valperga, G., Silengo, L., et al. (2015). The heme exporter Flvcr1 regulates expansion and differentiation of committed erythroid progenitors by controlling intracellular heme accumulation. Haematologica *100*, 720–729. https://doi.org/10.3324/haematol.2014.114488.
54. Petrillo, S., Chiabrando, D., Genova, T., Fiorito, V., Ingoglia, G., Vinchi, F., Mussano, F., Carossa, S., Silengo, L., Altruda, F., et al. (2018). Heme accumulation in endothelial cells impairs angiogenesis by triggering paraptosis. Cell Death Differ. *25*, 573–588. https://doi.org/10.1038/s41418-017-0001-7.
55. Fiorito, V., Allocco, A.L., Petrillo, S., Gazzano, E., Torretta, S., Marchi, S., Destefanis, F., Pacelli, C., Audrito, V., Provero, P., et al. (2021). The heme synthesis-export system regulates the tricarboxylic acid cycle flux and oxidative phosphorylation. Cell Rep. *35*, 109252. https://doi.org/10.1016/j.celrep.2021.109252.
56. Petrillo, S., De Giorgio, F., Kopecka, J., Genova, T., Fiorito, V., Allocco, A.L., Bertino, F., Chiabrando, D., Mussano, F., Altruda, F., et al. (2021). Endothelial Heme Dynamics Drive Cancer Cell Metabolism by Shaping the Tumor Microenvironment. Biomedicines *9*, 1557. https://doi.org/10.3390/biomedicines9111557.
57. Allocco, A.L., Bertino, F., Petrillo, S., Chiabrando, D., Riganti, C., Bardelli, A., Altruda, F., Fiorito, V., and Tolosano, E. (2022). Inhibition of Heme Export and/or Heme Synthesis Potentiates Metformin Anti-Proliferative Effect on Cancer Cell Lines. Cancers *14*, 1230. https://doi.org/10.3390/cancers14051230.
58. Giorgi, C., Missiroli, S., Patergnani, S., Duszynski, J., Wieckowski, M.R., and Pinton, P. (2015). Mitochondria-associated membranes: composition, molecular mechanisms, and physiopathological implications. Antioxidants Redox Signal. *22*, 995–1019. https://doi.org/10.1089/ars.2014.6223.
59. Barazzuol, L., Giamogante, F., and Calì, T. (2021). Mitochondria Associated Membranes (MAMs): Architecture and physiopathological role. Cell Calcium *94*, 102343. https://doi.org/10.1016/j.ceca.2020.102343.
60. Donegan, R.K., Moore, C.M., Hanna, D.A., and Reddi, A.R. (2019). Handling heme: The mechanisms underlying the movement of heme within and between cells. Free Radic. Biol. Med. *133*, 88–100. https://doi.org/10.1016/j.freeradbiomed.2018.08.005.
61. Reddi, A.R., and Hamza, I. (2016). Heme Mobilization in Animals: A Metallolipid's Journey. Acc. Chem. Res. *49*, 1104–1110. https://doi.org/10.1021/acs.accounts.5b00553.
62. Brailoiu, E., Chakraborty, S., Brailoiu, G.C., Zhao, P., Barr, J.L., Ilies, M.A., Unterwald, E.M., Abood, M.E., and Taylor, C.W. (2019). Choline Is an Intracellular Messenger Linking Extracellular Stimuli to IP. Cell Rep. *26*, 330–337.e334. https://doi.org/10.1016/j.celrep.2018.12.051.

63. Gkini, V., and Namba, T. (2023). Glutaminolysis and the Control of Neural Progenitors in Neocortical Development and Evolution. Neuroscientist *29*, 177–189. https://doi.org/10.1177/10738584211069060.

64. Kalailingam, P., Wang, K.Q., Toh, X.R., Nguyen, T.Q., Chandrakanthan, M., Hasan, Z., Habib, C., Schif, A., Radio, F.C., Dallapiccola, B., et al. (2020). Deficiency of MFSD7c results in microcephaly-associated vasculopathy in Fowler syndrome. J. Clin. Invest. *130*, 4081–4093. https://doi.org/10.1172/JCI136727.

65. Santander, N., Lizama, C.O., Meky, E., McKinsey, G.L., Jung, B., Sheppard, D., Betsholtz, C., and Arnold, T.D. (2020). Lack of Flvcr2 impairs brain angiogenesis without affecting the blood-brain barrier. J. Clin. Invest. *130*, 4055–4068. https://doi.org/10.1172/JCI136578.

66. Meyer, E., Ricketts, C., Morgan, N.V., Morris, M.R., Pasha, S., Tee, L.J., Rahman, F., Bazin, A., Bessières, B., Déchelotte, P., et al. (2010). Mutations in FLVCR2 are associated with proliferative vasculopathy and hydranencephaly-hydrocephaly syndrome (Fowler syndrome). Am. J. Hum. Genet. *86*, 471–478. https://doi.org/10.1016/j.ajhg.2010.02.004.

67. Li, Y., Ivica, N.A., Dong, T., Papageorgiou, D.P., He, Y., Brown, D.R., Kleyman, M., Hu, G., Chen, W.W., Sullivan, L.B., et al. (2020). MFSD7C switches mitochondrial ATP synthesis to thermogenesis in response to heme. Nat. Commun. *11*, 4837. https://doi.org/10.1038/s41467-020-18607-1.

68. Rönkkö, J., Molchanova, S., Revah-Politi, A., Pereira, E.M., Auranen, M., Toppila, J., Kvist, J., Ludwig, A., Neumann, J., Bultynck, G., et al. (2020). Dominant mutations in ITPR3 cause Charcot-Marie-Tooth disease. Ann. Clin. Transl. Neurol. *7*, 1962–1972. https://doi.org/10.1002/acn3.51190.

69. Krols, M., Detry, S., Asselbergh, B., Almeida-Souza, L., Kremer, A., Lippens, S., De Rycke, R., De Winter, V., Müller, F.J., Kurth, I., et al. (2018). Sensory-Neuropathy-Causing Mutations in ATL3 Cause Aberrant ER Membrane Tethering. Cell Rep. *23*, 2026–2038. https://doi.org/10.1016/j.celrep.2018.04.071.

70. Kornak, U., Mademan, I., Schinke, M., Voigt, M., Krawitz, P., Hecht, J., Barvencik, F., Schinke, T., Gießelmann, S., Beil, F.T., et al. (2014). Sensory neuropathy with bone destruction due to a mutation in the membrane-shaping atlastin GTPase 3. Brain *137*, 683–692. https://doi.org/10.1093/brain/awt357.

71. Gregianin, E., Pallafacchina, G., Zanin, S., Crippa, V., Rusmini, P., Poletti, A., Fang, M., Li, Z., Diano, L., Petrucci, A., et al. (2016). Loss-of-function mutations in the SIGMAR1 gene cause distal hereditary motor neuropathy by impairing ER-mitochondria tethering and Ca2+ signalling. Hum. Mol. Genet. *25*, 3741–3753. https://doi.org/10.1093/hmg/ddw220.

72. Rodríguez, L.R., Lapeña-Luzón, T., Benetó, N., Beltran-Beltran, V., Pallardó, F.V., Gonzalez-Cabo, P., and Navarro, J.A. (2022). Therapeutic Strategies Targeting Mitochondrial Calcium Signaling: A New Hope for Neurological Diseases? Antioxidants *11*, 165. https://doi.org/10.3390/antiox11010165.

73. Prinz, W.A., Toulmay, A., and Balla, T. (2020). The functional universe of membrane contact sites. Nat. Rev. Mol. Cell Biol. *21*, 7–24. https://doi.org/10.1038/s41580-019-0180-9.

74. Liu, M., Bertolazzi, G., Sridhar, S., Lee, R.X., Jaynes, P., Mulder, K., Syn, N., Hoppe, M.M., Fan, S., Peng, Y., et al. (2024). Spatially-resolved transcriptomics reveal macrophage heterogeneity and prognostic significance in diffuse large B-cell lymphoma. Nat Commun *15*, 2113. https://doi.org/10.1038/s41467-024-46220-z.

75. Ho, K.H., and Patrizi, A. (2021). Assessment of common housekeeping genes as reference for gene expression studies using RT-qPCR in mouse choroid plexus. Sci. Rep. *11*, 3278. https://doi.org/10.1038/s41598-021-82800-5.

76. Bertino, F., Firestone, K., Bellacchio, E., Jackson, K.E., Asamoah, A., Hersh, J., Fiorito, V., Destefanis, F., Gonser, R., Tucker, M.E., et al. (2019). Heme and sensory neuropathy: insights from novel mutations in the heme exporter feline leukemia virus subgroup C receptor 1. Pain *160*, 2766–2775. https://doi.org/10.1097/j.pain.0000000000001675.

77. Rizzuto, R., Simpson, A.W., Brini, M., and Pozzan, T. (1992). Rapid changes of mitochondrial Ca2+ revealed by specifically targeted recombinant aequorin. Nature *358*, 325–327. https://doi.org/10.1038/358325a0.

78. Brini, M., Marsault, R., Bastianutto, C., Alvarez, J., Pozzan, T., and Rizzuto, R. (1995). Transfected aequorin in the measurement of cytosolic Ca2+ concentration ([Ca2+]c). A critical evaluation. J. Biol. Chem. *270*, 9896–9903. https://doi.org/10.1074/jbc.270.17.9896.

79. Kuchay, S., Giorgi, C., Simoneschi, D., Pagan, J., Missiroli, S., Saraf, A., Florens, L., Washburn, M.P., Collazo-Lorduy, A., Castillo-Martin, M., et al. (2017). PTEN counteracts FBXL2 to promote IP3R3- and Ca^{2+}-mediated apoptosis limiting tumour growth. Nature *546*, 554–558. https://doi.org/10.1038/nature22965.

80. Rapizzi, E., Pinton, P., Szabadkai, G., Wieckowski, M.R., Vandecasteele, G., Baird, G., Tuft, R.A., Fogarty, K.E., and Rizzuto, R. (2002). Recombinant expression of the voltage-dependent anion channel enhances the transfer of Ca2+ microdomains to mitochondria. J. Cell Biol. *159*, 613–624. https://doi.org/10.1083/jcb.200205091.

81. Szabadkai, G., Simoni, A.M., Chami, M., Wieckowski, M.R., Youle, R.J., and Rizzuto, R. (2004). Drp-1-dependent division of the mitochondrial network blocks intraorganellar Ca2+ waves and protects against Ca2+-mediated apoptosis. Mol. Cell *16*, 59–68. https://doi.org/10.1016/j.molcel.2004.09.026.

82. Schindelin, J., Arganda-Carreras, I., Frise, E., Kaynig, V., Longair, M., Pietzsch, T., Preibisch, S., Rueden, C., Saalfeld, S., Schmid, B., et al. (2012). Fiji: an open-source platform for biological-image analysis. Nat. Methods *9*, 676–682. https://doi.org/10.1038/nmeth.2019.

83. Perez-Riverol, Y., Bai, J., Bandla, C., García-Seisdedos, D., Hewapathirana, S., Kamatchinathan, S., Kundu, D.J., Prakash, A., Frericks-Zipper, A., Eisenacher, M., et al. (2022). The PRIDE database resources in 2022: a hub for mass spectrometry-based proteomics evidences. Nucleic Acids Res. *50*, D543–D552. https://doi.org/10.1093/nar/gkab1038.

84. Mercurio, S., Aspesi, A., Silengo, L., Altruda, F., Dianzani, I., and Chiabrando, D. (2016). Alteration of heme metabolism in a cellular model of Diamond-Blackfan anemia. Eur. J. Haematol. *96*, 367–374. https://doi.org/10.1111/ejh.12599.

85. Liao, Y., Smyth, G.K., and Shi, W. (2019). The R package Rsubread is easier, faster, cheaper and better for alignment and quantification of RNA sequencing reads. Nucleic Acids Res. *47*, e47. https://doi.org/10.1093/nar/gkz114.

86. Love, M.I., Huber, W., and Anders, S. (2014). Moderated estimation of fold change and dispersion for RNA-seq data with DESeq2. Genome Biol. *15*, 550. https://doi.org/10.1186/s13059-014-0550-8.

87. Thomas, P.D., Ebert, D., Muruganujan, A., Mushayahama, T., Albou, L.P., and Mi, H. (2022). PANTHER: Making genome-scale phylogenetics accessible to all. Protein Sci. *31*, 8–22. https://doi.org/10.1002/pro.4218.

88. Song, L., Pan, S., Zhang, Z., Jia, L., Chen, W.H., and Zhao, X.M. (2021). STAB: a spatio-temporal cell atlas of the human brain. Nucleic Acids Res. *49*, D1029–D1037. https://doi.org/10.1093/nar/gkaa762.

89. Stuart, T., Butler, A., Hoffman, P., Hafemeister, C., Papalexi, E., Mauck, W.M., Hao, Y., Stoeckius, M., Smibert, P., and Satija, R. (2019). Comprehensive Integration of Single-Cell Data. Cell *177*, 1888–1902.e21. https://doi.org/10.1016/j.cell.2019.05.031.

90. Muth, T., Vaudel, M., Barsnes, H., Martens, L., and Sickmann, A. (2010). XTandem Parser: an open-source library to parse and analyse X!Tandem MS/MS search results. Proteomics *10*, 1522–1524. https://doi.org/10.1002/pmic.200900759.

91. Vaudel, M., Barsnes, H., Berven, F.S., Sickmann, A., and Martens, L. (2011). SearchGUI: An open-source graphical user interface for simultaneous OMSSA and X!Tandem searches. Proteomics *11*, 996–999. https://doi.org/10.1002/pmic.201000595.

92. Gatz, C., Hathazi, D., Münchberg, U., Buchkremer, S., Labisch, T., Munro, B., Horvath, R., Töpf, A., Weis, J., and Roos, A. (2019). Identification of

Cellular Pathogenicity Markers for SIL1 Mutations Linked to Marinesco-Sjögren Syndrome. Front. Neurol. *10*, 562. https://doi.org/10.3389/fneur.2019.00562.

93. Wieckowski, M.R., Giorgi, C., Lebiedzinska, M., Duszynski, J., and Pinton, P. (2009). Isolation of mitochondria-associated membranes and mitochondria from animal tissues and cells. Nat. Protoc. *4*, 1582–1590. https://doi.org/10.1038/nprot.2009.151.
94. Rizzuto, R., Brini, M., Pizzo, P., Murgia, M., and Pozzan, T. (1995). Chimeric green fluorescent protein as a tool for visualizing subcellular organelles in living cells. Curr. Biol. *5*, 635–642. https://doi.org/10.1016/s0960-9822(95)00128-x.
95. Salaroglio, I.C., Belisario, D.C., Akman, M., La Vecchia, S., Godel, M., Anobile, D.P., Ortone, G., Digiovanni, S., Fontana, S., Costamagna, C., et al. (2022). Mitochondrial ROS drive resistance to chemotherapy and immune-killing in hypoxic non-small cell lung cancer. J. Exp. Clin. Cancer Res. *41*, 243. https://doi.org/10.1186/s13046-022-02447-6.
96. Xu, X., Tassone, B., Ostano, P., Katarkar, A., Proust, T., Joseph, J.M., Riganti, C., Chiorino, G., Kutalik, Z., Lefort, K., and Dotto, G.P. (2021). HSD17B7 gene in self-renewal and oncogenicity of keratinocytes from Black versus White populations. EMBO Mol. Med. *13*, e14133. https://doi.org/10.15252/emmm.202114133.
97. Kawamata, H., Starkov, A.A., Manfredi, G., and Chinopoulos, C. (2010). A kinetic assay of mitochondrial ADP-ATP exchange rate in permeabilized cells. Anal. Biochem. *407*, 52–57. https://doi.org/10.1016/j.ab.2010.07.031.

STAR★METHODS

KEY RESOURCES TABLE

REAGENT or RESOURCE	SOURCE	IDENTIFIER
Antibodies		
Mouse monoclonal, Anti-FLVCR1 (C-4)	Santa Cruz Biotechnology, Dallas, TX, USA	Cat# sc-390100
Rabbit polyclonal, Anti-FLVCR1	Proteintech, Rosemont, IL, USA	Cat# 26841-1-AP; RRID:AB_2880654
Mouse monoclonal, Anti-Vinculin	Sigma-Aldrich, St. Louis, MO, USA, St. Louis, MO, USA	Cat# SAB4200080; RRID: AB_10604160
Mouse monoclonal, Anti-IP3R3	BD Biosciences, Franklin Lakes, NJ, USA	Cat# 610312; RRID:AB_397704
Rabbit polyclonal, Anti-IP3R3	Bethyl Laboratories, Inc., Montgomery, Texas, USA	Cat# A302-160A; RRID:AB_1720368
Mouse monoclonal, Anti-VDAC1/Porin (B-6)	Santa Cruz Biotechnology, Dallas, TX, USA	Cat# sc-390996; RRID:AB_2750920
Rabbit polyclonal, Anti-VDAC1/Porin antibody - Mitochondrial Loading Control	Abcam, Cambridge, UK	Cat# ab15895; RRID:AB_2214787
Normal mouse IgG	Santa Cruz Biotechnology, Dallas, TX, USA	Cat# sc-2025; RRID:AB_737182
Rabbit IgG Isotype Control	Thermofisher Scientific, Waltham, MA, USA	10500C; RRID:AB_2532981
Rabbit polyclonal, Anti-Myc tag	Abcam, Cambridge, UK	Cat# ab9106
Mouse monoclonal, Anti-Myc-Tag (9B11)	Cell Signaling Technology, Danvers, MA, Danvers, MA,	Cat# 2276; RRID:AB_331783
Rabbit polyclonal, anti-GFP	This paper	N/A
Mouse monoclonal, anti-GFP 2G8/C11	This paper	N/A
Rabbit polyclonal, anti- SOX2	Abcam, Cambridge, UK	Cat# ab97959; RRID:AB_2341193
Rabbit polyclonal, anti-TBR2	Abcam, Cambridge, UK	Cat# ab15894; RRID:AB_302116
Rabbit polyclonal, anti-PAX6	BioLegend	Cat# PRB-278P; RRID:AB_291612
Rabbit monoclonal, anti-MCU	Cell Signaling Technology, Danvers, MA, Danvers, MA,	Cat# 14997; RRID:AB_2721812
Mouse monoclonal, anti-HA	Thermofisher Scientific, Waltham, MA, USA	Cat# 26183; RRID:AB_2610625
Mouse monoclonal, anti-porin (clone 20B12AF2)	Abcam, Cambridge, UK	Cat# ab14734; RRID:AB_443084
Rabbit polyclonal, anti-GRP75	Proteintech, Rosemont, IL, USA	14887-1-AP; RRID:AB_2120458
Mouse monoclonal, anti-GRP75	Abcam, Cambridge, UK	Cat# ab2792; RRID:AB_303304
Rabbit polyclonal, anti-Laminin	Abcam, Cambridge, UK	Cat# ab16048; RRID:AB_443298
Mouse monoclonal, anti-P4HB antibody [RL90]	Abcam, Cambridge, UK	Cat# ab2792; RRID:AB_303304
Rabbit polyclonal, anti-ATP5i	Abcam, Cambridge, UK	Cat# ab126181; RRID:AB_11129974
Rabbit polyclonal, Anti-Sigma 1R	Sigma-Aldrich, St. Louis, MO, USA	Cat# HPA018002; RRID:AB_1854802
CellTracker^{TM} Fluorescent Probes	Thermofisher Scientific, Waltham, MA, USA	Cat# C7025
Rat monoclonal, anti-Ctip2 antibody [25B6]	Abcam, Cambridge, UK	Cat#ab18465; RRID:AB_2064130
Rabbit polyclonal, Anti-TBR1 antibody	Abcam, Cambridge, UK	Cat#ab31940; RRID:AB_2200219
Rat monoclonal Purified, anti-PAX6 Antibody	Biolegend	Cat# 939802; RRID:AB_2888904
Mouse monoclonal, Anti-beta III Tubulin antibody [2G10] - Neuronal Marker	Abcam, Cambridge, UK	Cat# ab78078; RRID:AB_2256751
Rabbit polyclonal, Anti-TBR2/Eomes antibody	Abcam, Cambridge, UK	Cat# ab23345; RRID:AB_778267

(*Continued on next page*)

Continued

REAGENT or RESOURCE	SOURCE	IDENTIFIER
Dynabeads protein G	Thermofisher Scientific, Waltham, MA, USA	Cat# 10004D
Dynabeads protein A	Thermofisher Scientific, Waltham, MA, USA	Cat# 10001D
Rabbit polyclonal, Orai1 Antibody	Santa Cruz Biotechnology, Dallas, TX, USA	Cat# sc-68895; RRID:AB_2283283
Rabbit polyclonal, Myc-tag Antibody	Abcam, Cambridge, UK	Cat# ab9106; RRID:AB_307014
Biological samples		
Human Tissues	Gynecology-Obstetric Department at Robert Debre Hospital, Paris	N/A
Primary fibroblasts (C1, C3, P3)	Cell Line and DNA Biobank from patients affected by Genetic Diseases° (Istituto Giannina Gaslini), member of Telethon Network of Genetic Biobanks (project no. GTB12001).	N/A
Primary fibroblasts (P3)	Unit of Rare Neurological Diseases, Fondazione IRCCS Istituto Neurologico Carlo Besta, Milano, Italy	N/A
Chemicals, peptides, and recombinant proteins		
TRIZMA (2-Amino-2-(hydroxymethyl)-1,3-propanediol)	Sigma-Aldrich, St. Louis, MO, USA	T1503; CAS: 77-86-1
HCl (hydrochloric acid)	Sigma-Aldrich, St. Louis, MO, USA	H1758; CAS: 7647-01-0
KCl (potassium chloride)	Sigma-Aldrich, St. Louis, MO, USA	P9541; CAS: 7447-40-7
$MgCl_2$ hexahydrate (magnesium chloride)	Sigma-Aldrich, St. Louis, MO, USA	M2393; CAS: 7791-18-6
ATP (Adenosine 5′-triphosphate)	Sigma-Aldrich, St. Louis, MO, USA	A6419; CAS: 34369-07-8
EDTA (Ethylenediaminetetraacetic acid)	Sigma-Aldrich, St. Louis, MO, USA	E9884; CAS: 60-00-4
PMSF (Phenylmethylsulfonyl fluoride)	Sigma-Aldrich, St. Louis, MO, USA	52332; CAS: 329-98-6
NaF (sodium fluoride)	Sigma-Aldrich, St. Louis, MO, USA	S7920; CAS: 7681-49-4
Sucrose	Sigma-Aldrich, St. Louis, MO, USA	S0389; CAS: 57-50-1
K_2HPO_4 (dipotassium hydrogen phosphate)	Sigma-Aldrich, St. Louis, MO, USA	P8281; CAS: 7758-11-4
KH_2PO_4 (potassium dihydrogen phosphate)	Sigma-Aldrich, St. Louis, MO, USA	P5655; CAS: 7778-77-0
BSA (bovine serum albumin)	Sigma-Aldrich, St. Louis, MO, USA	A2153; CAS: 9048-46-8
Saponin	Sigma-Aldrich, St. Louis, MO, USA	47036; CAS: 8047-15-2
Cytochrome *c*	Sigma-Aldrich, St. Louis, MO, USA	C7752; CAS: 9007-43-6
NaN_3 (sodium azide)	Sigma-Aldrich, St. Louis, MO, USA	S2002; 26628-22-8
NADH (β-Nicotinamide adenine dinucleotide, reduced disodium salt)	Sigma-Aldrich, St. Louis, MO, USA	N7410; 606-68-8
L-glutamic acid	Sigma-Aldrich, St. Louis, MO, USA	G1251; CAS: 56-86-0
L-malic acid	Sigma-Aldrich, St. Louis, MO, USA	M1000; 97-67-6
ADP (Adenosine 5-diphosphate sodium salt)	Sigma-Aldrich, St. Louis, MO, USA	A2754; CAS: 20398-34-9
Calcein acetoxymethyl ester	Thermofisher Scientific, Waltham, MA, USA	C1430
Cobalt Chloride	Sigma-Aldrich, St. Louis, MO, USA	769495

(*Continued on next page*)

Continued

REAGENT or RESOURCE	SOURCE	IDENTIFIER
Calcium Chloride	VWR INTERNATIONAL, RADNOR, PA, USA	21114-1L
Ionomycin	Sigma-Aldrich, St. Louis, MO, USA	I3909
Histamine	Sigma-Aldrich, St. Louis, MO, USA	H7250
Carbachol (Carbamoylcholine chloride)	Sigma-Aldrich, St. Louis, MO, USA	C4382
DSP (dithiobis(succinimidyl propionate)), Lomant's Reagent	Thermofisher Scientific, Waltham, MA, USA	Cat# 22585
PNGase F from Elizabethkingia meningoseptica	Thermofisher Scientific, Waltham, MA, USA	P7367
Doxycycline	Clontech Laboratories Inc. A Takara Bio Company	Cat# 631311
Normal Donkey Serum, Sterile	Sigma-Aldrich, St. Louis, MO, USA	Cat# 566460
ProLong^{TM} Gold Antifade Mountant Green features	Thermofisher Scientific, Waltham, MA, USA	Cat# P10144
Hygromycin B	Thermofisher Scientific, Waltham, MA, USA	Cat# 10687010
DMEM	Thermofisher Scientific, Waltham, MA, USA	Cat# 11965092
DMEM/F12	Thermofisher Scientific, Waltham, MA, USA	Cat# 10565018
Fetal Bovine Serum	Thermofisher Scientific, Waltham, MA, USA	Cat# A5256701
N-2 Supplement	Thermofisher Scientific, Waltham, MA, USA	Cat# 17502048
B-27^{TM} Supplement	Thermofisher Scientific, Waltham, MA, USA	Cat# 17504-044
bFGF	Sigma-Aldrich, St. Louis, MO, USA	Cat# F0291
Insulin solution human	Sigma-Aldrich, St. Louis, MO, USA	Cat# I9278
Amphotericin B	Sigma-Aldrich, St. Louis, MO, USA	Cat# A2942-50ML
Human EGF Recombinant Protein	Thermofisher Scientific, Waltham, MA, USA	Cat# RP-8661
"Flashtag" (CellTrace^{TM} CFSE)	Thermofisher Scientific, Waltham, MA, USA	Catalog number: C34554
Papain	Worthington	LS003119
Trypsin Inhibitor	Sigma-Aldrich, St. Louis, MO, USA	SIAL-T9253-1G
Sytox Red	Thermofisher Scientific, Waltham, MA, USA	S34859
Critical commercial assays		
DUOLINK kit	Sigma-Aldrich, St. Louis, MO, USA	Cat# DUO92101
RNeasy Micro kit	Qiagen, Germantown, MD, USA, Germantown, MD, USA, Germantown, MD, USA	Cat# 74004
NEBNext Ultra II RNA Library Prep Kit	New England Biolabs	Cat# E7760
Protease Inhibitor Cocktail set III	Sigma-Aldrich, St. Louis, MO, USA	Cat# 535140
BCA Protein Assay kit	Sigma-Aldrich, St. Louis, MO, USA	BCA1
Adenosine 5′-triphosphate (ATP) Bioluminescent Assay Kit	Sigma-Aldrich, St. Louis, MO, USA	FLAA
Purelink RNA mini kit	Thermofisher Scientific, Waltham, MA, USA	Cat# 12183018A
High-Capacity cDNA Reverse Transcription Kit	Thermofisher Scientific, Waltham, MA, USA	Cat# 4368813

(*Continued on next page*)

Continued

REAGENT or RESOURCE	SOURCE	IDENTIFIER
Lipofectamine^{TM} 3000 Transfection Reagent	Thermofisher Scientific, Waltham, MA, USA	Cat# L3000001
jetOPTIMUS	Polyplus, now part of Sartorius, Illkirch, France	Cat# 101000025
Click-iT^{TM} EdU Cell Proliferation Kit for Imaging	Thermofisher Scientific, Waltham, MA, USA	Cat# C10340
SuperScript III First-Strand Synthesis SuperMix for qRT-PCR	Thermofisher Scientific, Waltham, MA, USA	Cat# 11752050
LightCycler 480 SYBR Green I Master	Roche, Vienna Austria	Cat# 04707516001
Qiagen, Germantown, MD, USA, Germantown, MD, USA RNeasy Micro Kit	Qiagen, Germantown, MD, USA, Germantown, MD, USA	Cat# 74004
Deposited data		
RNA-sequencing	This paper	GEO: GSE221231
Proteomic data	This paper	ProteomeXchange Consortium: PXD047897
Raw data	This paper	N/A
Experimental models: Cell lines		
293T	ATCC, MANASSAS, VA USA	CRL-3216; RRID:CVCL_0063
HeLa	ATCC, MANASSAS, VA USA	CCL2; RRID:CVCL_0030
Flp-In T-REx 293	Thermofisher Scientific, Waltham, MA, USA	Cat# R78007
Experimental models: Organisms/strains		
Mouse: Flvcr1-myc mouse	Petrillo S. et al.[28]	N/A
Mouse: Flvcr1afl/fl	Vinchi F. et al.[30]	N/A
Mouse: B6.Cg-Tg(Nes-cre)1Kln/J	The Jackson Laboratory	Cat# 003771 RRID:IMSR_JAX:003771
E13.5 timed pregnant Swiss Webster (CFW) dams (Charles River E14)	Charles River Laboratories (CRL)	Strain Code: 024 RRID:IMSR_CRL:024
Oligonucleotides		
Murine Cre Rev: CATCGACCGGTAATGCAG	Vinchi F. et al.[30]	N/A
Murine Cre Fw: ACACCTGCTACCATATCATCC, MANASSAS, VA USATAC	Vinchi F. et al.[30]	N/A
Murine ILoxFlvcr1 Fw: TCTAAGGCCCAGTAGGACCC	Vinchi F. et al.[30]	N/A
Murine ILoxFlvcr1 Rev: GAAAGCATTTCCGTCCGCCC	Vinchi F. et al.[30]	N/A
Murine IILoxFlvcr1 Rev: AGAGGGCAACCTCGGTGTCC	Vinchi F. et al.[30]	N/A
mouse-*Flvcr1a*-forward: CCGTCGCCT CGGTATGG	Chiabrando D. et al.[24]	N/A
mouse-*Flvcr1a*-reverse: CACTAAAA CAGGTGGCAACAAAAA	Chiabrando D. et al.[24]	N/A
mouse-*Actb*-forward: TGA CGT TGA CAT CCG TAA AG	Ho and Patrizi[75]	N/A
mouse-*Actb*-reverse: GAG GAG CAA TGA TCT TGA TCT	Ho and Patrizi[75]	N/A

(*Continued on next page*)

Continued

REAGENT or RESOURCE	SOURCE	IDENTIFIER
Recombinant DNA		
pCMV-mito-GEM-GECO1	Addgene, Watertown, MA, USA	Cat# 32461; RRID:Addgene_32461
pLVX-puro empty vector	Clontech Laboratories Inc. A Takara Bio Company	Cat# 632164
TRC Lentiviral pLKO.1 Human FLVCR1 shRNA set, clone TRCN0000059599	Dharmacon – Horizon Discovery	Cat#RHS4533-EG28982
TRC Lentiviral pLKO.1 Non-targeting Control shRNA	Dharmacon – Horizon Discovery	Cat#RHS6848
pLVX-puro FLVCR1a vector	Bertino F et al.[76]	N/A
Mitochondria-targeted Aequorin (mt-AEQ)	Rizzuto et al.[77]	N/A
Citosol-targeted Aequorin (ct-AEQ)	Brini M et al.[78]	N/A
pcDNA3-IP3R3 GFP	Kuchay et al.[79]	N/A
VDAC-HA	Rapizzi E. et al.[80]	N/A
mt-DsRED	Szabadkai G et al.[81]	N/A
SEC61-GFP	Addgene, Watertown, MA, USA, Watertown, MA, USA	Cat# 121159
Software and algorithms		
Spectronaut® Version 17.8	Biognosys, Schlieren, Switzerland	https://biognosys.com/software/spectronaut/?gclid=Cj0KCQiAj_CrBhD-ARIsAIiMxT9JiKw7DNQ38mjq9OVadP7d-COh75F6ERplfFpRS2aVnuNizd9BNUEaAoidEALw_wcB
Xcalibur™ Software 4.3	Thermofisher Scientific, Waltham, MA, USA	https://www.thermofisher.com/order/catalog/product/OPTON-30965
Chromeleon 7.3 CDS	Thermofisher Scientific, Waltham, MA, USA	https://www.thermofisher.com/order/catalog/product/CHROMELEON7
ProbeFinder software	Roche, Vienna Austria	RRID:SCR_014490
GraphPad Prism v5.0 and v8.0	GraphPad Software, Inc.	https://www.graphpad.com/; RRID: SCR_002798
Fiji	Schindelin et al.[82]	https://fiji.sc/; RRID: SCR_002285
SeqNext 4.0 (JSI Medical systems)		https://www.jsi-medisys.de/products/sequence-pilot/seqnext/
Variant Studio 3.0 (Illumina)		https://www.illumina.com/products/by-type/informatics-products/variantstudio.html
Moon Software 4.01 (Diploid/Invitae)		https://us.moon.diploid.com/users/sign_in
R version 3.6		https://www.r-project.org/
Rsubread version 2.10		https://www.bioconductor.org/packages/release/bioc/html/Rsubread.html
DESeq2 version 1.36		https://www.bioconductor.org/packages/release/bioc/html/DESeq2.html
EnhancedVolcano version 1.14		https://www.bioconductor.org/packages/release/bioc/html/EnhancedVolcano.html
PANTHER version 17.0		https://www.pantherdb.org/
Incucyte ® SX5 Live-Cell Analysis		https://www.sartorius.com
GraphPad Prism		RRID:SCR_002798

(*Continued on next page*)

Continued

REAGENT or RESOURCE	SOURCE	IDENTIFIER
Other		
xGen Exome Research Panel v2 (IDT; Integrated DNA Technologies)		Catalog# 10005152
Lotus DNA Library Prep Kit (IDT; Integrated DNA Technologies		Catalog# 10001074

RESOURCE AVAILABILITY

Lead contact

Further information and requests for resources and reagents should be directed to and will be fulfilled by the lead contact, Deborah Chiabrando (deborah.chiabrando@unito.it), upon reasonable request.

Materials availability

All reagents/materials generated in this study will be made available upon reasonable request. The request may require a completed Materials Transfer Agreement.

Data and code availability

- RNAseq dataset is available at GEO (https://www.ncbi.nlm.nih.gov/geo/query/acc.cgi?acc=GSE221231). The mass spectrometry proteomics data have been deposited to the ProteomeXchange Consortium via the PRIDE[83] partner repository with the dataset identifier PXD047897.
- This paper does not report the original code.
- Any additional information required to reanalyze the data reported in this paper is available from the lead contact upon reasonable request.

EXPERIMENTAL MODEL AND SUBJECT DETAILS

Ethic statement

All procedures involving human participants, performed in the studies of Prenatal-Medicine Munich, Gynecology-Obstetric Department at Robert Debre Hospital Paris and Istituto Neurologico Carlo Besta, were in accordance with the ethical standards of the institutional and/or national research committee and with the 1964 Helsinki Declaration and its later amendments or comparable ethical standards.

Human fetus carrying *FLVCR1* mutations

A consanguineous couple from the United Arab Emirates (1st degree and 2nd degree cousins; see Pedigree Figure 1B) presented at the Prenatal Medicine Munich clinic for evaluation of extreme fetal microcephaly. The pregnancy occurred after *in vitro* fertilization and preimplantation diagnosis with numerous chromosomal disorders. The pregnancy was terminated in 34 + 5 gestational weeks with a birth weight of 1590g (−2.18z < 1P), 41cm body length (−2.31z < 1P) and 27cm head circumference (−3,6<1P). No primary cells or tissue biopsy of the fetus were available for biochemical analyses. The parents of the fetus orally reported a miscarriage but there are no external reports about it. Written informed consent was provided by the parents for the autopsy of the fetus (postmortem examination) as well as for the genetic analyses (whole exome sequencing, described below). Ultrasound pictures, pathology pictures and the results of the molecular diagnostics were consented for publication.

Fetal human tissues for immunostaining

Fetal Human tissues were obtained from the Gynecology-Obstetric Department at Robert Debre Hospital, Paris, according to the rules established by the French Bioethics Agency and with parental consent. 11 Post Conception Weeks (PCW) fetal brains were obtained after volunteer abortion or spontaneous pregnancy termination, respectively. These human fetal tissues were used to analyze FLVCR1 expression in the human developing cortex by immunofluorescence.

PCARP/HSAN patient-derived primary fibroblasts culture

Patient 1 (P1) and Patient 3 (P3) have been previously described.[21,22] Briefly, P1 carried compound heterozygous variants in *FLVCR1* gene (c.574T>C; p.(Cys192Arg) and c.610del; p.(Met204Cysfs*56)) and showed early onset pain insensitivity reminiscent of hereditary sensory and autonomic neuropathy (HSAN).[22] P3 carried a homozygous missense variation c.661C>T, p.Pro221Ser in the *FLVCR1* gene and showed combination of typical PCARP and sensory-autonomic neuropathy.[21] Primary fibroblasts derived from

P1 and controls (C1, C3) were previously descibed,[22] whereas primary fibroblasts derived from P3 were isolated from the skin. Specifically, they were collected from the left deltoid region using a 3-mm punch biopsy under sterile conditions. This procedure was conducted with the patient informed consent and in accordance with the ethical guidelines approved by the Istituto Neurologico Carlo Besta Institution Review Board (NCT04880356). The experiments on primary fibroblasts were also approved by the local ethic committee of the University of Torino (Protocol number 0254821). Specifically, primary fibroblasts were used to perform proximity ligation assay (PLA) and western blotting, and to measure mitochondrial Ca2+ concentration upon histamine stimulation, mitochondrial ATP content, the activity of the ETC complexes as described below.

Mouse model

Flvcr1-myc mice have been described previously.[28] Briefly, *Flvcr1-myc* mice were generated by CRISPR/Cas9, inserting the MYC sequence in frame at the 3′ end of the FLVCR1 coding region. *Flvcr1a*$^{fl/fl}$ mice have been described previously.[30] To generate *Flvcr1a*$^{fl/fl}$;Nes-cre mice, *Flvcr1a*$^{fl/fl}$ mice were crossed to mice expressing Cre recombinase under control of nestin promoter (Nes-Cre). Nes-Cre mice were purchased from the Jackson Laboratory (B6.Cg-Tg(Nes-cre)1Kln/J Strain #:003771). Experiments on mice followed European legislation (Directive 2010/63/EU), concerning housing, husbandry, and animal welfare. The experimental procedures were approved by the Italian Ministry of Health (Approval number 604/2021-PR).

Murine embryonic neocortical neuroprogenitor cell (NPC) primary cultures

Mouse dorsal telencephalon was dissected from E12.5 brains in DMEM/F12 medium (Thermofisher Scientific). Cell suspension was obtained by mechanical dissociation. NPCs from each telencephalon were grown individually as neurospheres in 6 well plates and in DMEM/F12 medium supplemented with 1x N2 and 0.5xB27, 10 ng/mL EGF (Thermofisher Scientific) and bFGF (Sigma Aldrich) and 10 mg/mL Insulin (Sigma Aldrich). Two days after the culture start, primary cultures of the same genotype were pooled by two or three in a 10cm dish for further expansion during two to three days. At this stage, neurospheres were mechanically dissociated for seeding on gelatin-coated dishes, glass coverslips in 24-well plates or IBIDI slides (IBIDI). Attached cells were cultured in DMEM medium (Thermofisher Scientific) supplemented with 20% fetal bovine serum and 1mM sodium pyruvate. Cells were then maintained in culture for a maximum of 7 days. NPC primary cultures were used to analyze ultrastructural morphology (transmission electron microscopy), proliferation, calcium fluxes and energetic metabolism, as described below.

Cell lines

HEK293, Flp-In T-Rex 293 and HeLa cells were cultured in Dulbecco's modified Eagle's medium (DMEM; Gibco) supplemented with 10% fetal bovine serum (Gibco). Human fibroblasts were cultured in DMEM, supplemented with 10% fetal bovine serum and 1% Non-Essential Amino Acid (NEAA) (Gibco).

METHOD DETAILS

Whole exome sequencing

For Variant analysis and interpretation, the following softwares were used: SeqNext 4.0 (JSI Medicals), Variant Studio 3.0 (Illumina) and the Moon Software 4.0.1 (Diploid/Invitae). DNA was extracted from amniotic fluid and parental blood samples for Trio Whole Exome Sequencing (Trio-WES), following partents' informed consent. Investigation of the coding areas including adjacent intron regions of the Trio-whole exome was performed using high-throughput sequencing from genomic DNA (xGen Exome Research Panel v2; 19,433 genes; Integrated DNA Technology). The genomic DNA was processed using the hybrid capture method, relevant areas were enriched and amplified by PCR (Lotus DNA Library Prep Kit, IDT) and sequenced by massive parallel sequencing on the NextSeq 550 system (Illumina). Our quality criteria require a minimum coverage of 20 sequences per base for at least 96% of the target areas of all genes examined. For Variant analysis and interpretation, the following Softwares were used: SeqNext 4.0 (JSI Medicals), Variant Studio 3.0 (Illumina) and the Moon Software 4.0.1 (Diploid/Invitae). The analysis revealed a frameshift variant c.160delC, p. Arg54GlyfsTer59 in the *FLVCR1* gene in the homozygous state in the fetus and in the heterozygous state in each parent. These results were confirmed by conventional Sanger sequencing.

Fetal human tissues immunostaining

After 24 h fixation in 4% PFA, fetal human tissues (PCW11) were cryoprotected in 15% sucrose in PBS, frozen in isopentane at −50°C, and kept at −80°C. Transverse 20 micron-thick sections were cut on a Leica CM 3050 cryostat and kept at −80°C until use. Antigen retrieval was performed by heating sections in 50 mM citrate buffer pH 6 for 20 min at 95°C. After rinsing in PBS, sections were incubated overnight at 4°C with primary antibodies diluted in Bond Primary Antibody Diluent (LEICA; AR9352). The antibodies were mouse anti FLVCR1 (Santa Cruz Biotechnology; sc-390100; 1:500) and rabbit anti PAX6 (Proteintech; 12323-1-1P; 1:2000), anti SOX2 (Abcam; ab97959; 1:2000) and anti TBR2 (Abcam; ab23345; 1:250). After two 10 min washes in PBS, sections were incubated in highly absorbed goat anti-mouse and goat anti rabbit IgG, coupled to either Alexa 480 (Thermofisher Scientific) or Cy3 (Jackson) diluted 1:2000, for 2 h at room temperature. 1 μg/mL DAPI (4′,6-diamidino-2-phénylindole; Sigma-Aldrich) was added to the secondary antibody solution. After rinsing in PBS, sections were mounted in Fluoromount-G (SouthernBiotech). Imaging was performed using a Leica TCS SP8 confocal scanning system (Leica Microsystems) equipped with 405-nm Diode, 488-nm Ar and 561-nm DPSS lasers. A 20x HC PL APO oil-immersion objective was used to take tiles images in a sequential mode and with a 1024×1024 resolution. Pictures with composite colors and the corresponding Tiff files were generated on ImageJ and further processed on Photoshop C6 for sizing and eventually for improving color contrast.

"Flashtag" *in utero* injections

"Flashtag" labeling of enriched cell populations in wild type mice was conducted for a separate pilot experiment in the Panagiotakos lab, as described below. A portion of the RNA collected for that experiment was used for this study. Prior to surgery, "Flashtag" working solution was prepared according to Govindan et al.[29] Specifically, 8μL of DMSO and 1μL of 0.01% Fast Green was added to one vial of CellTrace CFSE (Thermofisher Scientific, C34554). Glass micropipettes were pulled and beveled to produce a fine pointed tip 30-70μM in outer diameter.

For "Flashtag" injections, E13.5 timed-pregnant Swiss Webster dams (E14, Charles River Labs) were anesthetized with isofluorane (2-4% to effect). Multimodal analgesia (0.1 mg/kg Buprenorphine hydrochloride and 5 mg/kg Carprofen) was administered preoperatively via subcutaneous injection. Aseptic technique was used throughout the procedure. The uterine horns were exposed via a midline incision and gently lifted out of the abdominal cavity onto sterile gauze pads. The abdominal cavity was continuously bathed in pre-warmed, sterile saline throughout the surgery. 0.5μL of "Flashtag" was injected into the lateral ventricle of individual embryos using a beveled micropipette. After all embryos were injected, the uterine horns were gently returned to the abdominal cavity, bathed one final time in warm saline, and the incision was closed in two layers. Lidocaine was applied locally prior to incision closure. Animals recovered in heated recovery cages and were returned to their home cages once they were alert and ambulating normally.

FACS

1h, 10hrs, 24hrs, and 4 days after "Flashtag" injection (corresponding to the labeling of radial glia, intermediate progenitor cells, newborn neurons and postmitotic neurons, respectively), pregnant dams were sacrificed, and embryonic brains were dissected in ice-cold HBSS. For the 1h and 10h post-injection time points, the ventricles of dissected brains were flushed with a pipette to dilute any residual "Flashtag" solution. The meninges were carefully removed from the brains, and individual cortical hemispheres were dissected and processed separately in downstream steps. Cortices were digested with papain (Worthington, LS003119) for 7 min at 37C and subsequently bathed in Trypsin Inhibitor (Sigma Aldrich, SIAL-T9253-1G) and dissociated into single cell suspensions in ice-cold HBSS with DNAse. Cortical hemispheres were then separately sorted on a BD FACS Aria. Dead cells were excluded using Sytox Red (Life Technologies, S34859), and the top 5–10% of "Flashtag"-expressing cells were collected in Buffer RLT (from the Qiagen RNeasy Micro Kit, 74004). Parameters for FACS gates were set up as described in Govindan et al., 2018.[29]

Quantitative real-time PCR analysis (qPCR)

For the analysis of Flvcr1a mRNA levels in "Flashtag"-cell populations, RNA was extracted using the Qiagen RNeasy Micro kit. RNA quality and concentration was confirmed using the Agilent BioAnalyzer, and cDNA was made using the Superscript III kit (Invitrogen, 11752050). qPCR was then performed using the LightCycler 480 SYBR Green I Master (Roche) with primers designed to specifically target each gene of interest. qPCR were performed on a Roche Lightcycler instrument Technical duplicates or triplicates were performed, and Ct values were normalized to Actb levels. Replicates were discarded if Ct values varied greater than 0.5 Ct values. A transcript's relative abundance was calculated as follows: (Etarget–Ct (target))/(EActB–Ct (ActB)). Primers used are listed below:

mouse-*Actb*-forward: TGA CGT TGA CAT CCG TAA AG70[75]
mouse-*Actb*-reverse: GAG GAG CAA TGA TCT TGA TCT70[75]
mouse-*Flvcr1a*-forward: CCGTCGCCTCGGTATGG
mouse *Flvcr1a*-reverse: CACTAAAACAGGTGGCAACAAAAA.

For the analysis of Flvcr1a and Flvcr1b mRNA levels in embryos brain or isolated NPCs, total RNA was extracted from mouse brain using Purelink RNA mini kit (Thermofisher Scientific, catalog *n* 12183018A). Between 500 and 1000ng of total RNA were transcribed into complementary DNA (cDNA) by High-Capacity cDNA Reverse Transcription Kit (Thermofisher Scientific, catalog *n* 4368813). qPCR was performed using gene-specific TaqMan Gene Expression Assays (Thermofisher Scientific). qPCR were performed on a 7300 or 7900 Real-Time PCR System (Thermofisher Scientific). Transcript abundance, normalized to 18S mRNA expression, is expressed as a fold increase over a calibrator sample. Primers and probe used are listed below:

mouse-*Flvcr1a*-forward: CCGTCGCCTCGGTATGG
mouse *Flvcr1a*-reverse: CACTAAAACAGGTGGCAACAAAAA
mouse-*Flvcr1b*-forward: TCGCTTCCTATTGACAGCTATTAACA
mouse *Flvcr1b*-reverse: CACTAAAACAGGTGGCAACAAAAA.
FAM probe (for both *Flvcr1a* and *Flvcr1b*): TTGGAACTGCAGTTGGT[24,84]

PCR

Mice and embryos genotyping was performed by PCR, as described in Petrillo S.et al.[54] To detect the Cre allele, primers Cre-Fw (5'-GGACATGTTCAGGGATCGCCAGGCG-3') and Cre-Rev (5'-GCATAACCAGTGAAACAGCATTGCT-3') were used. To detect the *Flvcr1a* deleted allele, primers ILox-Fw (5'-TCTAAGGCCCAGTAGGACCC-3') and IILox-Rev (5'-AGAGGGCAACCTCGGTGTCC-3') were used, given a 320-bp fragment. To analyze the *LoxP* sites on Flvcr1 gene, primers ILox-Fw (5'-TCTAAGGCCCAGTAGGAC CC-3') and ILox-Rev (5'-GAAAGCATTTCCGTCCGCCC-3') were used, given a 280-bp band for the floxed allele and a 242-bp band for the wild-type allele.[54]

Micro computed tomography (Micro-CT)

Micro-CT analysis was performed on E18.5 mouse embryos using a Bruker Skyscan 1172 micro-CT. Embryos were fixed in formalin and then stained for 15 days with a soft tissue contrast agent (phosphotungstic acid (PTA) 2.5% dissolved in water. Acquisitions were performed at 80KV using a 0.5mm Al filter at a resolution of 7 μm, 0.6° of rotation step, 360° scan, 4x frame averaging.

Histological analysis

Flvcr1a$^{fl/fl}$ and Flvcr1a$^{fl/fl}$;NesCRE+ P0 lungs were fixed in formalin, dehydrated, and embedded in paraffin. Slides were incubated with hematoxylin for 4 min, then rinsed in deionized water and incubated in 1% eosin for 30 s. Finally, slides were incubated for 30 s in 80-90-100% ethanol solution for dehydration and in 100% xylene (Sigma Aldrich, USA) for 1 min before mounting with DPX reagent (VWR) and coverslips. Microscopic analysis of histological sections was done with Automated Upright Microscope Leica DM6 B.

Immunofluorescence analysis on mouse tissues

Embryonic brains were collected and fixed overnight in 4% PFA, then washed 3 times in 1X PBS. The brains were frozen in OCT and cut 20 μm sections in a cryostat (Leica). The Sections were mounted on glass slides and washed 3 times in 1X PBS. Then were blocked and permeabilized for 1 h in a blocking buffer containing 0.5% Triton X-100, 1% BSA, and 5% normal donkey serum (Sigma Aldrich). Then, the sections were incubated with primary antibodies diluted in an antibody dilution buffer containing blocking buffer: PBS (1:1) in a humidified chamber overnight. Next day, the sections were washed 5 times in 1X PBS and after that were incubated with corresponding secondary antibodies in antibody dilution buffer for 2 h, washed again 5 times 1X PBS. Then mounted with Prolong gold antifade mounting media (Thermofisher Scientific). Images were taken using Zeiss 780 upright laser-scanning confocal microscope with a 34-detector array with a water immersion Zeiss Plan Apochromat 20 Å∼/1.0, D = 0.17, parfocal length 75 mm (Zeiss). The spectral configuration was set up using the recommended settings from Zen software (Zeiss). Raw images were analyzed using ImageJ.

Edu staining

E14.5 pregnant females were injected with 50 mg/kg Edu 2 h before sacrifice. Then, embryos were harvested, fixed in 4% PFA. Immunofluorescence was performed on cryosections according to the manufacturer instructions (Click-iT EdU Imaging Kits – Thermofisher Scientific).

TUNEL assay

TUNEL assay was performed on cryosection using the “*In Situ* Cell Death Detection Kit” (Roche), following the manufacturer instructions.

RNA sequencing

Total RNA from whole E14.5 embryo brain was isolated with RNAeasy Plus Micro kit (Qiagen). Sequencing libraries were constructed from total RNA with RIN>7 using the NEBNext Ultra II RNA Library Prep Kit (New England Biolabs, MA). Unstranded libraries were sequenced using a HiSeq4000 system (Illumina, CA) to produce ∼40 million 150 pb paired-end reads. After demultiplexing, fastq files were aligned to the mouse genome (mm10) with Rsubread 2.10[85] and quantified using FeatureCounts. Differential expression analysis was performed with DESeq2 1.36.[86] Volcano plots were rendered using the EnhancedVolcano 1.14[86] package and heatmaps were made with the pheatmap 1.0 package. Overrepresentation analysis was performed using PANTHER 17.0.[87]

FLVCR1 scRNA-seq differential expression analysis

Differential expression of *FLVCR1* was determined in a previously described scRNA-seq atlas of the human brain spanning the period between early-fetal development into adulthood.[88] The FindAllMarkers (dataset, features = ‘FLVCR1’, logfc.threshold = 0, min.cells.-feature = 0, return.thresh = 1) function from the Seurat package in R ([89]; version 3.2.0) was used to calculate the natural log fold change of the average expression of FLVCR1 between each cluster of interest and all other clusters in the dataset. Differential expression was based on a non-parametric, two-sided Wilcoxon rank-sum test with *p*-values adjusted through Bonferroni correction using all features in the dataset.

NPCs proliferation

NPCs were seeded on 96 wells and subsequently transfected with the appropriate plasmids. NPCs proliferation was assessed by using the Incucyte SX5 Live-Cell Analysis Instrument for 48 h post transfection. For the analysis the Incucyte SX5 Live-Cell Analysis software was used with scan type mode “whole well”, with 4X magnification. Representative images have been selected and shown for each condition.

Tandem affinity purification (TAP)

Flp-In T-Rex 293 cells that stably express inducible FLVCR1a cDNA fused to a C-terminal tandem affinity purification (TAP) tag (FLVCR1a-TAP), or the TAP tag alone (empty vector) were generated according to the manufacturer's instructions (Thermofisher Scientific). Hygromycin B (Thermofisher Scientific) at a concentration of 10 mg/mL was used for selection of stable cell clones. To induce expression doxycycline (Sigma Aldrich) was administered to the cells at a final concentration of 1 mg/mL for 48 h.

Preparation of pulldown samples for proteomic analysis

The snap-frozen pulldown samples were heated to 95°C for 5 min and cooled afterward until they reached room temperature. Ice-cold acetone was added in a 3-fold excess to the samples, which were then stored for protein precipitation at −20°C overnight. Samples with precipitated proteins were centrifuged at 12,000 g at 4°C for 20 min. Acetone was removed, and the samples were allowed to dry under the fume hood to evaporate the acetone. 8 M freshly prepared urea (50 μL) was added to the protein pellets to dissolve them. Disulfide bonds were then reduced by the addition of 10 mM TCEP at 37°C for 30 min, and free sulfhydryl bonds were alkylated with 15 mM IAA at room temperature (RT) in the dark for 30 min. Afterward, the sample solution was diluted to 1 M urea using 10 mM ABC (ammonium bicarbonate) buffer (pH 7.8), and an in-solution digestion was carried out using 1 μg trypsin (Sigma Gold). Samples were incubated at 37°C overnight. After 15 h, the reaction was stopped by adding 2 μL of 99% FA (formic acid). The samples were desalted using solid-phase extraction with C18 filter cartridges (Waters), washed with 0.1% TFA, and eluted with 80% acetonitrile. Cleaned samples were dried using a vacuum concentrator and dissolved in 20 μL of 0.1% TFA for mass spectrometry analysis.

Mass spectrometry analysis

All samples were analyzed using an UltiMate 3000 RSLC nano UHPLC coupled to a Thermo Scientific LTQ Orbitrap Velos. The samples were first transferred to a 75 μm × 2 cm, 100 Å, C18 pre column with a flow rate of 20 μL/min for 20 min followed by a separation on the 75 μm × 50 cm, 100 Å, C18 main column with a flow rate of 250 nL/min and a linear gradient consisting of solution A (99.9% water, 0.1% formic acid) and solution B (84% acetonitrile, 15.9% water, 0.1% formic acid) where the pure gradient length was 100 min (3–38% Solution B). The gradient was applied as follows: 3% B for 20 min, 3–38% for 100 min, followed by 3 wash steps each ranging to 95% buffer B for 3 min. After the last washing step, the instrument was allowed to equilibrate for 20 min at 3% buffer B. The acquisition of MS data was performed in DDA (data dependent acquisition) mode.

Mass spectrometry data analysis

Data analysis of the acquired label free quantitative MS data was performed using the Progenesis LC-MS software from Nonlinear Dynamics (Newcastle upon Tyne, U.K.). Alignment of MS raw data was conducted by Progenesis, which automatically selected one of the LC-MS files as reference for software-based normalization. Next, peak picking was performed and only features within retention time and m/z windows from 0 to 90 min and 300–1500 m/z, with charge states +2, +3, and +4 were considered for peptide statistics, analysis of variance (ANOVA). To minimize redundant MS/MS spectra, features with ≤5 rank were exported as peak lists which were searched against a concatenated target/decoy version of the human Uniprot database with 20226 target entries, downloaded on 26.10.2017 using Mascot 2.6 (Matrix Science) and XTANDEM Vengeance (2015.12.15.2)[90] with the help of SearchGUI 3.3.11.[91] Trypsin with a maximum of two missed cleavages was selected as enzyme. Carbamidomethylation of Cys was set as fixed and oxidation of Met was selected as variable modification. MS and MS/MS tolerances were set to 10 ppm and 0.5 Da, respectively. Combining the search results and filtering the data at a false discovery rate of 1% on the protein, peptide and peptide-spectrum match level was done using PeptideShaker 1.16.36. For reliable label-free quantification, only proteins with ≥2 unique peptides were considered for further analysis. Subsequently, the average normalized abundances (determined using Progenesis) were calculated for each protein and used to determine the ratio between the FLVCR1a and empty tag control samples. Proteins with a ratio (FLVCR1a/empty) of at least 4 or higher were considered for interaction partner analysis to exclude biological bias. Before IP3R3-VDAC and FLVCR1a interaction validation we verified that the selected proteins were not present in the list of interactors of TAP-tag alone (not shown) or other proteins with similar topology and localization as SIL1[92] and CLC3 and CLC4 (not shown).

Subcellular fractionation

Fractionations were performed as described previously.[93] IP3R3 (BD biosciences 610312) and VDAC (Abcam ab154856) were used as markers for the ER, cytosol, and pure mitochondria, respectively. ORAI1 (Santa Cruz Biotechnology; sc-68895) was used as a marker for plasma membrane protein.

Immunofluorescence analyses on cell cultures

Cells grown on glass coverslips were fixed with methanol and 4% paraformaldehyde (PFA) in phosphate buffered saline for 10 min at room temperature, and then permeabilized with 0.1% Triton X-100 in PBS for 10 min. Cells were subsequently incubated with primary antibodies: FLVCR1 primary antibody (Santa Cruz Biotechnology, Dallas, TX USA, catalog n° sc-390100; 1:50), rabbit FLVCR1a (Proteintech, catalog n° 26841), VDAC (Abcam, catalog n° ab154856), IP3R3 (BD biosciences, catalog n° 610312), GRP75 (Proteintech, catalog n°14887), Sigma 1R (Sigma Aldrich, catalog n° HPA018002). Dapi was used to label the nucleus (Sigma Aldrich; 1:500). Alexa 488 or Alexa 594 secondary antibodies (Thermo Fisher Scientific; 1:1000) were incubated with the cells for 60 min at room temperature. Confocal image acquisition was performed with a Leica TCS SP8 confocal system (Leica Microsystems) with an HC PL APO 63 ×/1.30 OIL CS2 objectives.

For the analysis of FLVCR1a localization, the percentage of FLVCR1a signal arising from the plasma membrane and from mitochondria associated membranes (MAMs) was assessed using ImageJ. To visualize the entire cell, we segmented the signal of the cell tracker using a binary mask. The cell membrane was calculated by eroding the cell tracker signal of 10um. MAMs were segmented using the Sigma1R signal. Then, the integrated density of FLVCR1a signal in the whole cell ROI was calculated together with the signal in the plasma membrane and MAMs ROI. Then, the ratio between plasma membrane/whole cell and MAMs/whole cell was measured. The colocalization of FLVCR1a with the plasma membrane and with the MAMs marker Sigma1R was evaluated using the JACOP plugin of ImageJ.

Proximity ligation assay (PLA)

PLA were performed on HeLa cells or human primary fibroblasts seeded on a 96 well plate. The assays were performed using a DUOLINK kit (Sigma Aldrich), following the supplier instructions and with the following antibody associations: rabbit FLVCR1a/mouse IP3R3 (1:50), mouse FLVCR1a/rabbit VDAC1 (1:50), mouse FLVCR1a/rabbit GRP75 (1:50). Negative controls have been made using FLVCR1 mouse or rabbit antibody in pair with rabbit or mouse antibodies, respectively, recognizing proteins which do not interact with FLVCR1. The following antibody associations were used: rabbit FLVCR1a/mouse PDI (1:50), mouse FLVCR1a/rabbit Atp5i (1:50), mouse FLVCR1a/rabbit Laminin (1:50). To analyze ER-mitochondria contact sites PLA was performed using mouse IP3R3 – rabbit VDAC antibodies pair (1:100). Duolink signal was acquired using the Olympus scanR fluorescence microscope equipped with an Uplan S apo 20x and a Hamamatsu ORCA 05G. The scanR Analysis software was used to process and analyze images. Cells were detected using the DAPI signal, for each cell Duolink dots were identified and fluorescence intensity of each dot collected. Duolink signal was then expressed as the integrated fluorescence intensity of all the dots per each cell.

The following antibodies were used: mouse FLVCR1a (Santa Cruz Biotechnology, catalog n° sc-390100), rabbit FLVCR1a (Proteintech, catalog n°26841), VDAC (Abcam, catalog n° ab154856), IP3R3 (BD biosciences, catalog n° 610312), GRP75 (Proteintech, catalog n° 14887), (Abcam, catalog n° ab2792), ATP5i (Abcam, catalog n° ab126181), Lamin (Abcam, catalog n° ab16048), PDI (Abcam, catalog n°ab2792).

Cell transient transfections and plasmids

Transient transfection in Hek293T cells was performed using LIPOFECTAMINE 2000 and 3000 (Thermofisher Scientific, 11668019) following manufacturer instructions. Transient transfections in NPCs were performed using jetOPTIMUS DNA transfection Reagent (Polyplus, 101000025). NPCs were seeded and analyzed 24 h after transfection.

Experiments were performed using the following plasmids: pCMV-mito-GEM-GECO1 (Addgene plasmid #32461), FLVCR1a-myc cDNA was cloned in plvx-puro vector (Addgene) as previously described.[76] pAc-GFPC1-Sec61beta (Addgene plasmid #15108), dsRed was cloned into pcDNA3, in frame with the mitochondria localization sequence of human COX8 as previously described,[94] mitochondrial aequorin was cloned into pcDNA3 as described in Rizzuto et al.[77]

Gene silencing and overexpression

FLVCR1a silencing in HeLa cells was performed using a shRNA that specifically downregulates FLVCR1a, without targeting the FLVCR1b isoform (TRC Lentiviral pLKO.1 Human FLVCR1 shRNA set RHS4533-EG28982, clone TRCN0000059599; Dharmacon). For control cells, a pLKO.1 lentiviral vector expressing a scramble (scr) shRNA was used. For FLVCR1a overexpression in HeLa cells the PLVX-pure vector with FLVCR1a-Myc-Tag was used. For control cells, the empty vector was used. Following lentiviral transduction, cells were maintained in selective medium containing 0.002 mg/ml puromycin (Puromycin dihydrochloride from Streptomyces alboniger, Sigma-Aldrich, catalog n° P8833).

Transient MCU overexpression was performed by transfecting human primary fibroblasts with JETOPTIMUS (Polyplus) according to manufacturer instructions. mito-GEM-GECO vector overexpression in Neural progenitor cells (NPCs) was achieved by using JETOPTIMUS (Polyplus) according to manufacturer instructions.

Immunoprecipitation

Cells were first incubated with DSP (dithiobis(succinimidyl propionate)) to facilitate protein crosslinking. The pellets were lysed in TAP lysis buffer (50mM Tris-HCl [pH 7.5], 150 mM NaCl, 1 %NP-40, 10% glycerol) and protease inhibitor cocktail (Roche, #04693159001) on ice for 30 min. For IP, 1 mg of protein extract was incubated with 1-3-5 μg of the appropriate antibody overnight at 4C. Rabbit or Mouse IgG were used as negative controls. The subsequent day, the antibody-protein complexes were incubated 2 h at 4°C with Dynabeads protein G (Thermofisher Scientific; Cat# 10004D) or Dynabeads protein A (Thermofisher Scientific; Cat# 10001D). The precipitates were washed with the TAP buffer without protease inhibitors 5 times. Beads were incubated with 2ul of PNGase 10′ 37°C to remove FLVCR1a glycosylation prior immunoblotting. Samples were incubated in 2 × Laemmli buffer freshly supplemented with 8% 2-mercaptoethanol 10 min at 37°C (to recover FLVCR1a) and then 10 min at 95°C.

Embryo brains were collected at E18.5 and lysed with MYC lysis buffer (40mM KCl, 25mM Tris-HCl pH 7.5, 1% Triton, 0.6mM MnCl2) with Protease Inhibitors Cocktail (Roche ref. 04693159001) and 1mM DTT on ice 20 min. For IP, 1 mg of protein extract was incubated with 3ug of VDAC antibody (VDAC Abcam catalog n° ab154856), overnight at 4°C. Rabbit IgG were used as negative controls. The subsequent day, the antibody-protein complexes were incubated 2 h at 4°C with Dynabeads protein A (Thermofisher Scientific; catalog n° 10001D). The precipitates were washed with the MYC buffer without protease inhibitors 5 times. Beads were incubated with 2ul of PNGase 10′ 37°C to remove FLVCR1a glycosylation prior immunoblotting. Samples were incubated in 2 × Laemmli buffer freshly supplemented with 8% 2-mercaptoethanol 10 min at 37°C (to recover FLVCR1a) and then 10 min at 95°C

The following antibodies were used for IP: mouse FLVCR1a (Santa Cruz Biotechnology, catalog n° sc-390100), rabbit FLVCR1a (Proteintech, catalog n°26841), VDAC (Abcam, catalog n° ab154856), GFP (home-made antibody generated for GFP tag), Myc-tag (Abcam, catalog n°ab9106).

Western blotting

To assess FLVCR1a expression, cells were lysed by rotation for 30 min at 4°C in RIPA buffer (150 mM NaCl, 50 mM Tris–HCl pH 7.5, 1% Triton X-100, 0.5% Sodium deoxycholate, 0.1% SDS, 1 mM EDTA). The buffer was freshly supplemented with 1 mM phosphatase inhibitor cocktail (Sigma Aldrich, catalog n° P0044), 1 mM PMSF (Sigma Aldrich, catalog n° 93482-50ML-F), and protease inhibitor cocktail (La Roche, catalog n° 04693116001). The cell lysate was clarified by centrifugation for 10 min at 4°C. Protein concentration in the supernatant was assessed by Bradford assay. For FLVCR1a protein detection, 10 μg of protein extracts was incubated 10 min at 37°C with 1 μL of PNGase-F from Elizabethkingia meningoseptica (Sigma Aldrich, catalog n° P-7367) to remove protein glycosylation. Before loading on 4–15% mini- PROTEAN TGX precast gel (Bio-Rad, Hercules, CA USA, catalog n°4568084), samples were incubated 5 min at 37°C (FLVCR1) or 5 min at 95°C (Vinculin, VDAC, IP3R3) in 4 × Laemmli buffer freshly supplemented with 8% 2-mercaptoethanol.

The primary antibodies and dilutions are as follows: FLVCR1 (C-4) (Santa Cruz Biotechnology, catalog n° sc-390100; 1:500); Vinculin (home-made, 1:8000); Anti-myc tag antibody (Abcam, catalog n°ab9106, 1:1000), VDAC (Abcam, catalog n° ab154856, 1:1000), IP3R3 (BD biosciences, catalog n°610312, 1:2000), IP3R3 (Bethyl Laboratories, catalog n° 50-156-1922, 1:1000), Myc-Tag antibody (Abcam, catalog n° ab9106, 1:1000), HA-tag Monoclonal antibody (Thermofisher Scientific, catalog n° 26183).

Endoplasmic reticulum (ER) - mitochondria contact sites measurement

Contact sites between ER and mitochondria were analyzed as follows. HeLa cells were transfected using a plasmid containing a mitochondria localization peptide fused with the fluorescent protein RFP (mt-DsRed) and a plasmid containing the ER resident protein Sec61 fused with GFP (Sec61-GFP). Living cells were analyzed for mt-DsRed and Sec61-GFP expression using an Olympus FV3000 confocal microscope equipped with PLAPON60XOSC2 60X oil immersion objective (n.a. 1.4). Colocalization of the two signals was quantified using the ImageJ Colocalization plugin JACOP, upon application of the TOP HAT (BOX) filter. A total of 10 cells per coverslip and 3 coverslips per experiment were analyzed. The results indicated a total of 3 independent experiments ($n = 3$).

Aequorin based calcium measurements

All aequorin measurements were performed transfecting cells with the appropriate aequorin chimera targeted to the mitochondria (mtAEQmut) or cytosol (citAEQ), as previously described.[40] Briefly, cells were seeded onto 13mm glass coverslips and transfected with a mitochondrial or cytosolic targeted Aequorin probe. Before the measurement, cells were incubated with 5 mM coelenterazine for 1.5 h in a saline buffer supplemented with 1mM CaCl2, and then transferred to the perfusion chamber. Cells were stimulated using an IP3-dependent agent (Histamine) to evoke Calcium discharge from the Endoplasmic Reticulum and rapid Calcium accumulation inside mitochondria. The experiments were terminated by lysing cells with Triton X-100 in a hypotonic calcium-rich solution, thus discharging the remaining aequorin pool. The light signal was collected and calibrated into [Ca2+] values by an algorithm based on the Calcium response curve of aequorin at physiological conditions of pH, [Mg2+], and ionic strength. 5 coverslips per experiment were subjected to the analysis. The results represent a total of 3 independent experiments ($n = 3$).

FRET based calcium measurement

Single-cell measurements of [Ca2+]m were performed in HeLa cells transfected with 4mtD3cpv. After 36 h, cells were imaged on a Zeiss Axiovert 100TV microscope equipped with an Uplan S Apo 60X oil immersion objective (n.a. 1.35), a Retiga R3 CCD camera (Photometrics) and controlled by METAFLUOR 7.0 Software (Universal Imaging). Emission ratio imaging of the cameleon was accomplished by using a 436DF20 excitation filter, a 450 nm dichroic mirror, and two emission filters (475/40 for ECFP and 535/25 for citrine) controlled by a Lambda 10-2 filter changer (Sutter Instruments). Fluorescence images were background corrected. Exposure times were typically 100 to 200 ms, and ratio images were collected 1 Hz.

Calcein/Co2+ quenching assays

For the calcein-cobalt quenching assay, all cells were stained with 1μM calcein acetoxymethyl ester (C1430, Thermofisher Scientific), 2mM CoCl2 (769495, Sigma Aldrich) and 1mM CaCl2 (21114-1L, VWR), in Krebs Ringer buffer for 30 min at 37°C in a 5% CO2 atmosphere. Image acquisition was performed with a Nikon Eclipse Ti widefield microscope equipped with a CFI Plan Apochromat Lambda D 60X Oil objective (n.a. 1.42). During imaging, cells were immersed in 2mM CoCl2 and 1mM CaCl2, in Krebs Ringer buffer and imaged for 60 s at 1Hz then stimulated with Ionomycin 1 μM (I3909, Sigma Aldrich) for 240 s. Images were processed with Fiji (https://imagej.net/software/fiji/downloads) to subtract background and suppress noise. Fluorescence intensity over the entire timelapse was next obtained for each cell in the field of view. The quenching rate was calculated as the slope of the fluorescence trace over a period of 60 s after stimulation.

Mitochondrial extraction and electron transport chain (ETC) activity

Mitochondria were extracted as reported in Salaroglio et al.[95] Cells were lysed in 0.5mL mitochondria lysis buffer (50 mM Tris-HCl, 100 mM KCl, 5 mM $MgCl_2$, 1.8 mM ATP, 1 mM EDTA, pH7.2), supplemented with Protease Inhibitor Cocktail III (Sigma), 1 mM phenylmethylsulfonyl fluoride (PMSF) and 250 mM NaF. Samples were clarified by centrifugation at 650*g* for 3 min at 4°C. Supernatants were collected and centrifuged at 13000g for 5 min at 4°C. The new supernatants, corresponding to the cytosolic fraction, were used for cytosolic ROS measurements. Pellets, containing mitochondria, were washed once with lysis buffer and resuspended in 0.25 mL mitochondria resuspension buffer (250 mM sucrose, 15 mM K_2HPO_4, 2 mM $MgCl_2$, 0.5 mM EDTA). 50 μL aliquots were sonicated and used for the measurement of protein content by the BCA Protein Assay kit (Sigma) and for quality control: 10 μg of each sonicated sample were analyzed by SDS-PAGE and immunoblotting with an anti-porin antibody (Abcam; clone 20B12AF2) to confirm the presence of mitochondrial proteins in the extracts. The remaining 200 μL were used to measure the electron flux from complex I to complex III, taken as an index of the mitochondrial respiratory activity,[95] 50 μg of non-sonicated mitochondrial samples, isolated as indicated above, were re-suspended in 0.2 mL buffer A (5 mM K_2HPO_4, 5 mM $MgCl_2$, 5% w/v bovine serum albumin, BSA; pH 7.2) to which 0.1 mL buffer B (25% w/v saponin, 50 mM K_2HPO_4, 5 mM $MgCl_2$, 5% w/v BSA, 0.12 mM oxidized cytochrome *c*, 0.2 mM NaN_3, which blocks complex IV allowing the accumulation of reduced cytochrome *c*; pH 7.5) was added for 5 min at room temperature. The cytochrome *c* reduction reaction was started by adding 0.15 mM NADH and was followed for 5 min at 37°C, reading the absorbance at 550 nm by a Packard microplate reader EL340 (Bio-Tek Instruments, Winooski, VT). The results were expressed as nanomoles of reduced cytochrome *c*/min/mg mitochondrial proteins.

Activity of each ETC complexes

The activity of each ETC complex was measured spectrophotometrically as detailed previously.[96] To measure complex I activity, 20 μg of non-sonicated mitochondrial samples was re-suspended in 0.2 mL buffer 1A (5 mM KH_2PO_4, 5 mM $MgCl_2$, 5% w/v BSA), incubated 1 min at room temperature followed by 7 min in 0.1 mL buffer 1B (25% w/v saponin, 50 mM KH_2PO_4, 5 mM $MgCl_2$, 5% w/v BSA, 0.12 mM oxidized ubiquinone, which acts as electrons shuttle from complex I to complex III, 2.5 mM antimycin A, which inhibits complex III, 0.2 mM NaN_3, which blocks complex IV; pH 7.5). 1.5 mM NADH, as electron donor was added to the mix. The rate of NADH oxidation was followed for 5 min at 37°C, reading the absorbance at 340 nm. The results were expressed as nanomoles of NAD^+/min/mg mitochondrial proteins.

Complex II activity was measured as rate of electrons transfer between complex II and complex III. 20 μg of non-sonicated mitochondrial samples was re-suspended in 0.1 mL buffer 2A (50 mM KH_2PO_4, 7.5 mM $MgCl_2$, 25% w/v saponin, 20 mM succinic acid; pH7.2) and incubated for 30 min at room temperature. 0.2 mL buffer 2B (50 mM KH_2PO_4, 7.5 mM $MgCl_2$, 5% w/v BSA, 30 mM succinic acid as substrate of complex II, 0.12 mM oxidized ubiquinone as electrons shuttle from complex II to complex III, 0.12 mM oxidized cytochrome *c* as acceptor of electrons flowing from complex II to complex III, 5 mM rotenone to prevent electron flux from complex I, 0.2 mM NaN3, to block complex IV) was added. The rate of reduction of cytochrome *c* was measured for 5 min at 37°C, reading the absorbance at 550 nm. The results were expressed as nanomoles of reduced cytochrome *c*/min/mg mitochondrial proteins.

The activity of complex III was measured in the same samples where the electron flux from complex I to complex III was evaluated. After 1 min from the addition of NADH, as inducer of electrons flow, 5 mM rotenone, which blocks the activity of complex I, was added. The rate of reduction of cytochrome *c*, which is dependent on the activity of complex III only in the presence of rotenone, was followed for 5 min at 37°C, reading the absorbance at 550 nm. The results were expressed as nanomoles of reduced cytochrome *c*/min/mg mitochondrial proteins.

To measure the activity of complex IV, the rate of oxidation of cytochrome *c* (reduced form, generated by complex III) was measured. 20 μg of non-sonicated mitochondrial samples was resuspended in 0.1 mL buffer 4A (50 mM KH_2PO_4, 20 mM succinic acid, 25% w/v saponin; pH 7.2) and incubated 30 min at room temperature. 0.2 mL buffer 4B (50 mM KH_2PO_4, 5 mM rotenone, which prevents electron flux from complex I to complex III, 30 mM succinic acid as substrate of complex II and electrons generator, 0.03 mM reduced cytochrome *c* as acceptor of electrons flowing from complex III to complex IV) was added. The rate of oxidation of cytochrome *c* was followed for 5 min at 37°C, reading the absorbance at 550 nm. The results were expressed as nanomoles of oxidized cytochrome *c*/min/mg mitochondrial proteins.

Adenine nucleotide translocase (ANT) activity

The activity of ANTs was measured fluorimetrically on 250 μg mitochondrial proteins according to Kawamata et al.[97] Results were expressed as μmoles exchanged ATP/mg mitochondrial proteins.

Pyruvate dehydrogenase, a-ketoglutarate dehydrogenase, isocitrate dehydrogenase activities

The activities of pyruvate dehydrogenase, α-ketoglutarate dehydrogenase and isocitrate dehydrogenase were measured spectrophotometrically using the Pyruvate dehydrogenase (PDH) Enzyme Activity Microplate Assay (Abcam), the Isocitrate Dehydrogenase

Activity Assay Kit (Sigma Aldrich), the Alpha Ketoglutarate (alpha KG) Assay Kit (Abcam) and the as per manufacturer's instructions. Results were expressed as nmoles NADH/min/mg proteins according to the respective titration curve previously set.

Mitochondrial ATP levels

ATP amounts in mitochondrial extracts were measured with the ATP Bioluminescent Assay Kit (Millipore Sigma), as per manufacturer's instructions. Results were expressed as nmoles ATP/mg mitochondrial proteins.

Transmission electron ultrastructural analysis

Cells were fixed with 2.5% glutaraldehyde in 0.1 M cacodylate buffer for 1 h at 4°C. After three rinses with 0.1 M sodium cacodylate buffer, cell pellets were embedded in 3% agarose and sliced into small blocks (1mm 3), rinsed with the same buffer three times and post-fixed with 1% osmium tetroxide and 0.8% Potassium Ferricyanide in 0.1 M sodium cacodylate buffer for one and a half hours at room temperature. Cells were rinsed with water and *en bloc* stained with 4% uranyl acetate in 50% ethanol for 2 h. Cells were dehydrated with increasing concentration of ethanol, transitioned into propylene oxide, infiltrated with Embed-812 resin and polymerized in a 60°C oven overnight. The semi-thin sections obtained with a Reichet Ultracut S ultramicrotome were stained with a 1% toluidine blue in an aqueous sodium borate solution and examined under light microscopy Nikon Eclipse E800. Ultrathin sections of selected areas were contrasted with lead-citrate according to Reynolds and observed on a TEM Thermo Fisher Talos L120C G2. ER and mitochondrial membranes were manually outlined using an optical pen and annotated in Fiji using the TrekEM2 plugin. Contact sites were identified manually to calculate their length.

Embryonic NPC calcium imaging and quantification

For ratiometric mito-GEM-GECO1 imaging of neuroepithelial cultures, the 405-nm Diode laser of a Leica TCS SP8 confocal scanning system (Leica Microsystems) was used. Emission windows were set to 427–467 nm (blue channel) and 502–537 nm (green channel). Eight-bit digital images were collected from a single optical plane using a 63x HC PL APO CS2 oil-immersion Leica objective (numerical aperture 1.40). Settings for laser intensity, pinhole (1 Airy unit), range property of emission window, electronic zoom, gain and offset of photomultiplicator, field format, scanning speed were optimized initially and held constant throughout the study so that all cells were digitized under the same conditions. Mitochondrial signals of the blue and green channels were segmented; their ratio was calculated and measured using the Analyze Particles command of FIJI/ImageJ.[82] To evoke Calcium discharge from the Endoplasmic Reticulum and rapid Calcium accumulation inside mitochondria, neural progenitor cells (NPCs) were treated with Carbachol at a working concentration of 500μM.

QUANTIFICATION AND STATISTICAL ANALYSIS

Sample size, mean and statistical details of experiments can be found in the figure legends. Statistical analyses were conducted in GraphPad Prism v9.0.0 (GraphPad Software, Inc., La Jolla, CA USA, https://www.graphpad.com/; RRID:SCR_002798). No statistical method was used to predetermine sample size in studies.

Cell Reports Medicine, Volume *5*

Supplemental information

Dysregulation of FLVCR1a-dependent mitochondrial calcium handling in neural progenitors causes congenital hydrocephalus

Francesca Bertino, Dibyanti Mukherjee, Massimo Bonora, Christoph Bagowski, Jeannette Nardelli, Livia Metani, Diletta Isabella Zanin Venturini, Diego Chianese, Nicolas Santander, Iris Chiara Salaroglio, Andreas Hentschel, Elisa Quarta, Tullio Genova, Arpana Arjun McKinney, Anna Lucia Allocco, Veronica Fiorito, Sara Petrillo, Giorgia Ammirata, Francesco De Giorgio, Evan Dennis, Garrett Allington, Felicitas Maier, Moneef Shoukier, Karl-Philipp Gloning, Luca Munaron, Federico Mussano, Ettore Salsano, Davide Pareyson, Maja di Rocco, Fiorella Altruda, Georgia Panagiotakos, Kristopher T. Kahle, Pierre Gressens, Chiara Riganti, Paolo P. Pinton, Andreas Roos, Thomas Arnold, Emanuela Tolosano, and Deborah Chiabrando

SUPPLEMENTARY FIGURES AND LEGENDS

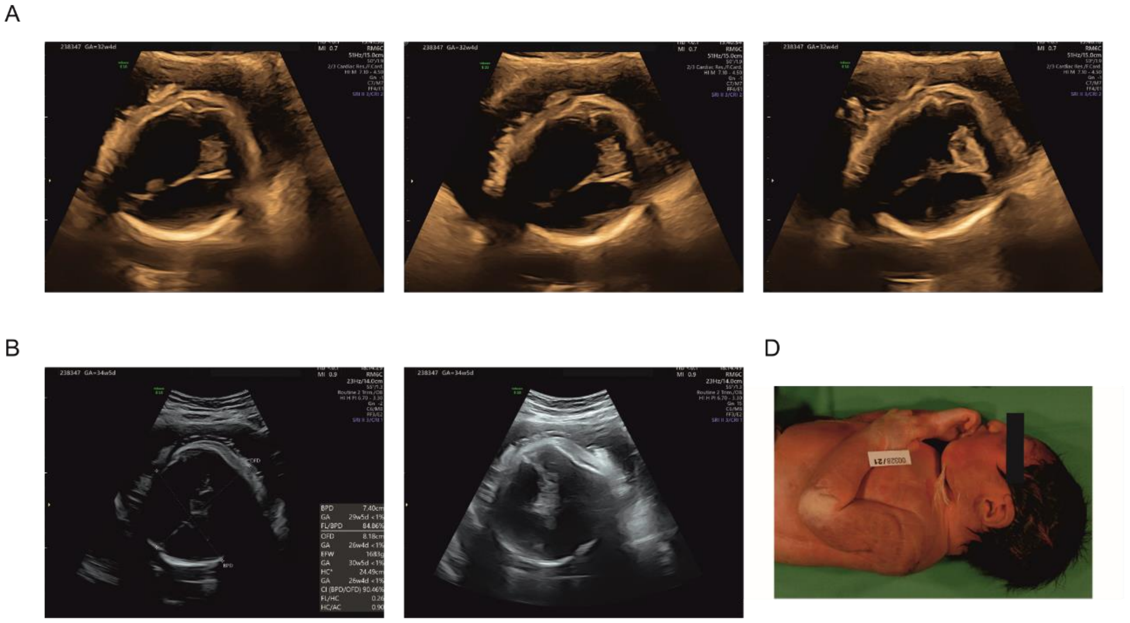

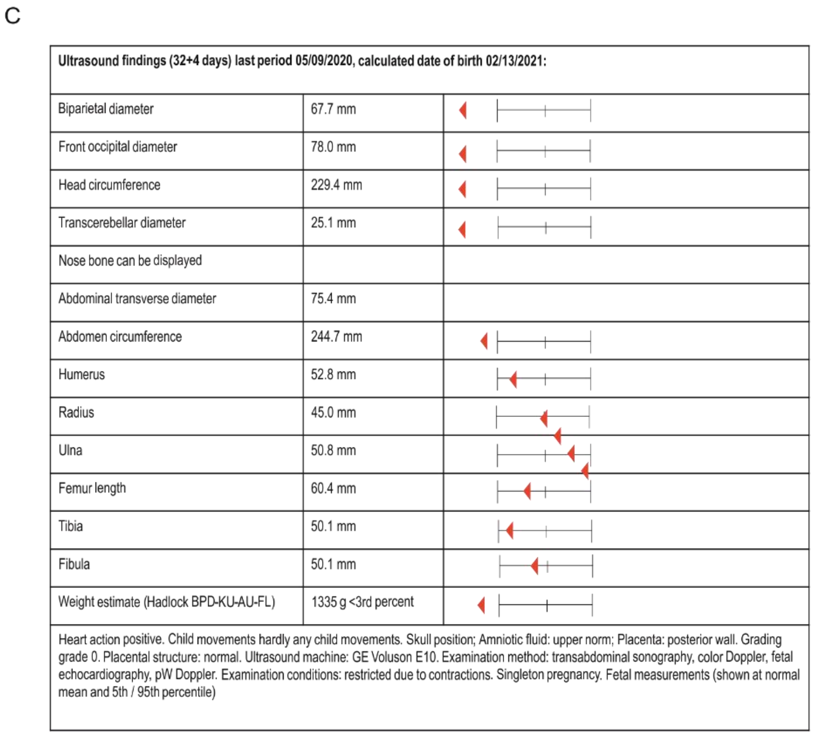

Ultrasound findings (32+4 days) last period 05/09/2020, calculated date of birth 02/13/2021:

Biparietal diameter	67.7 mm	
Front occipital diameter	78.0 mm	
Head circumference	229.4 mm	
Transcerebellar diameter	25.1 mm	
Nose bone can be displayed		
Abdominal transverse diameter	75.4 mm	
Abdomen circumference	244.7 mm	
Humerus	52.8 mm	
Radius	45.0 mm	
Ulna	50.8 mm	
Femur length	60.4 mm	
Tibia	50.1 mm	
Fibula	50.1 mm	
Weight estimate (Hadlock BPD-KU-AU-FL)	1335 g <3rd percent	

Heart action positive. Child movements hardly any child movements. Skull position; Amniotic fluid: upper norm; Placenta: posterior wall. Grading grade 0. Placental structure: normal. Ultrasound machine: GE Voluson E10. Examination method: transabdominal sonography, color Doppler, fetal echocardiography, pW Doppler. Examination conditions: restricted due to contractions. Singleton pregnancy. Fetal measurements (shown at normal mean and 5th / 95th percentile)

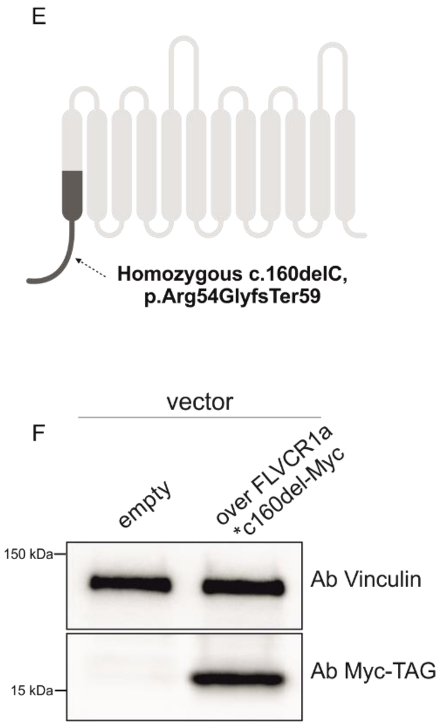

Figure S1. Macroscopic and Sonographic evaluation of the male fetus carrying inactivating mutations in the *FLVCR1* gene, Related to Figure 1

(A) Sonographic examinations of 32+4 weeks of pregnancy. **(B)** Sonographic examinations of 34+5 weeks of pregnancy. Sonographic examinations show extreme microcephaly with anechoic skull and no evidence of cerebral tissue. **(C)** Ultrasound findings (32+4 days) last period of pregnancy. **(D)** Macroscopic evaluation showed an immature male fetus of the 35th gestational week with microcephaly and hydrocephalus with only rudimentary cerebral structures and no indication of visceral anomalies. The anamnesis revealed that there was no family history of neuropathy, posterior column dysfunction or retinitis pigmentosa, clinical features associated with other rare disorders associated to FLVCR1 mutation(PCARP/HSAN). No clinical information was available on the miscarriage. **(E)** Schematic representation of the truncated protein resulting from the c.160delC(p.Arg54GlyfsTer59) *FLVCR1* mutation, highlighted in grey. **(F)** Immunobloting showing the overexpression of FLVCR1a*c160del-myc in HeLa cells. An antibody for the myc-tag was used.

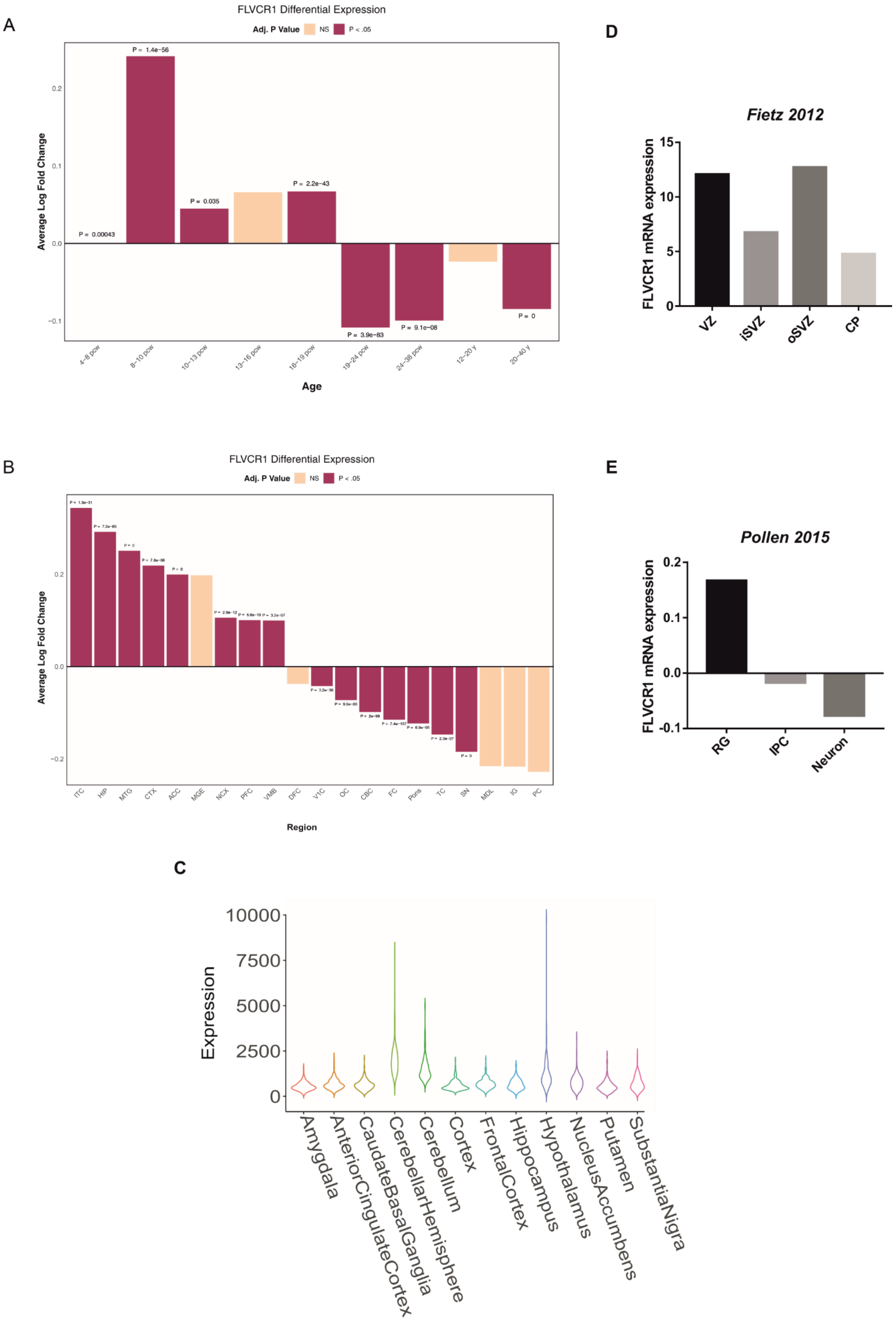
A
FLVCR1 Differential Expression
Adj. P Value
NS
P < .05
Average Log Fold Change
0.2
0.1
0.0
−0.1
P = 0.00043
P = 1.4e−56
P = 0.035
P = 2.2e−43
P = 3.9e−83
P = 9.1e−08
P = 0
4–8 pcw
8–10 pcw
10–13 pcw
13–16 pcw
16–19 pcw
19–24 pcw
24–38 pcw
12–20 y
20–40 y
Age
B
FLVCR1 Differential Expression
Adj. P Value
NS
P < .05
Average Log Fold Change
0.2
0.0
−0.2
P = 1.3e−31
P = 7.2e−65
P = 0
P = 7.8e−86
P = 0
P = 2.9e−12
P = 6.8e−10
P = 3.2e−07
P = 3.2e−36
P = 9.6e−05
P = 2e−99
P = 7.4e−157
P = 6.9e−05
P = 2.3e−07
P = 0
ITC
HIP
MTG
CTX
ACC
MGE
NCX
PFC
VMB
DFC
V1C
OC
CBC
FC
Pons
TC
SN
MDL
IG
PC
Region
C
Expression
10000
7500
5000
2500
0
Amygdala
AnteriorCingulateCortex
CaudateBasalGanglia
CerebellarHemisphere
Cerebellum
Cortex
FrontalCortex
Hippocampus
Hypothalamus
NucleusAccumbens
Putamen
SubstantiaNigra
D
Fietz 2012
FLVCR1 mRNA expression
15
10
5
0
VZ
iSVZ
oSVZ
CP
E
Pollen 2015
FLVCR1 mRNA expression
0.2
0.1
0.0
-0.1
RG
IPC
Neuron

Figure S2. FLVCR1a expression pattern in developmental and adult human brains, Related to Figure 1

(A) Differential expression of FLVCR1 across developmental periods in a single-cell data set of over 100,000 cells. PCW, postconceptional weeks; Y, years; **(B)** Differential expression of FLVCR1 across different brain regions in a single-cell data set of over 100,000 cells spanning from 4 PCW to 40 years old. **(C)** Allen Brain Atlas analysis of FLVCR1a expression in the adult human brain. ACC, anterior cingulate cortex; CBC, cerebellar cortex; CTX, cortex; DFC, dorsolateral prefrontal cortex; FC, frontal cortex; HIP, hippocampus; IG, insular gyris; ITC, inferior temporal cortex; MDL, medulla; MGE, medial ganglionic eminence; MTG, middle temporal gyrus; NCX, neocortex; OC, occipital cortex; PC, parietal cortex; PFC, prefrontal cortex; SN, substantia nigra; TC, temporal cortex; V1C, primary visual cortex; VMB, ventral midbrain; PCW, postconceptional weeks; Y, years; **(D)** FLVCR1 mRNA levels in human ventricular zone (VZ), inner subventricular zone (iSVZ), outer subventricular zone (oSVZ) and cortical plate (CP) from the Fietz et. al dataset.[S1] **(E)** FLVCR1 mRNA levels in radial glia (RGCs), intermediate progenitors (IPs) and mature neurons from the Pollen et. al dataset.[S2]

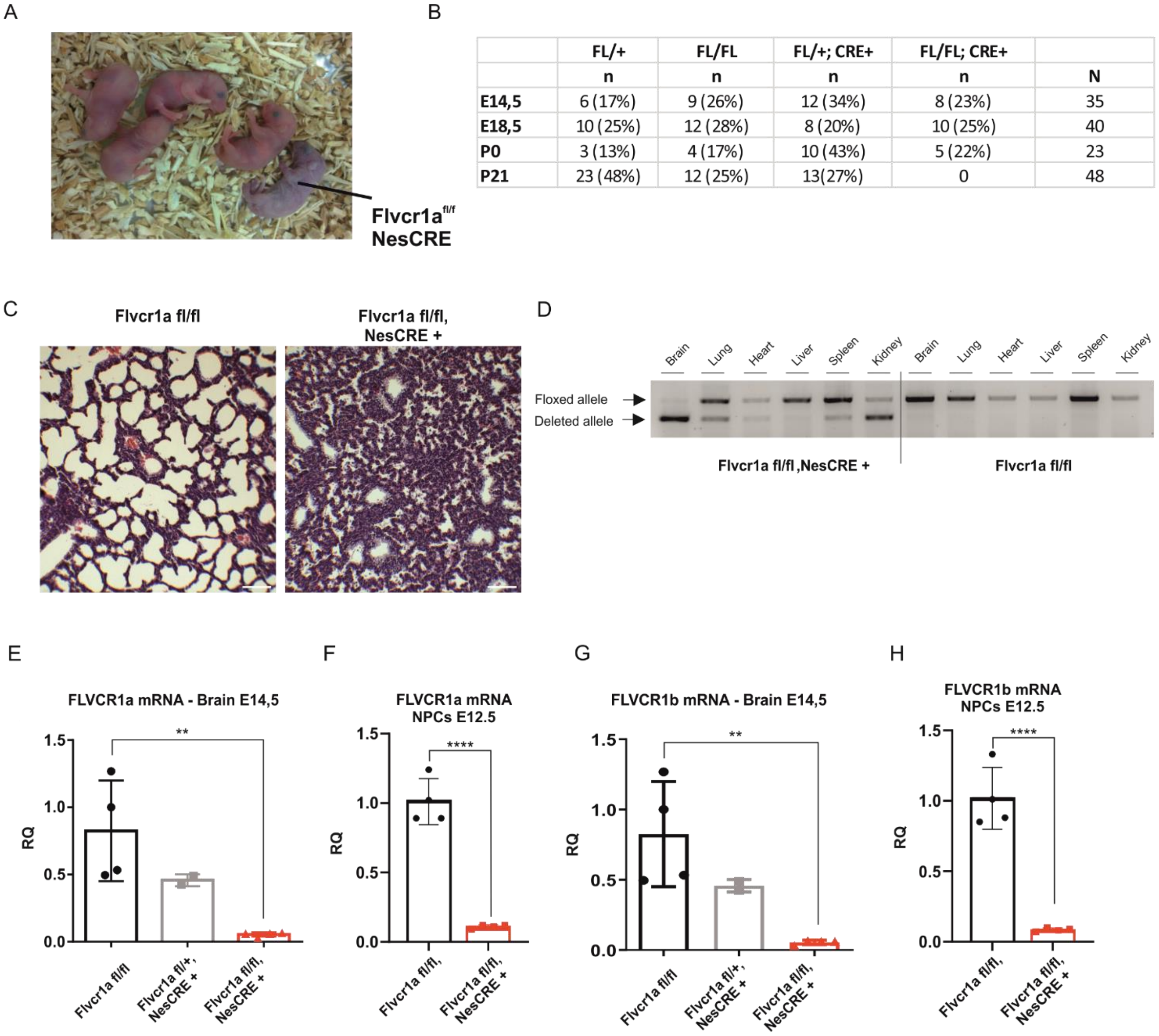

	FL/+	FL/FL	FL/+; CRE+	FL/FL; CRE+	
	n	n	n	n	N
E14,5	6 (17%)	9 (26%)	12 (34%)	8 (23%)	35
E18,5	10 (25%)	12 (28%)	8 (20%)	10 (25%)	40
P0	3 (13%)	4 (17%)	10 (43%)	5 (22%)	23
P21	23 (48%)	12 (25%)	13(27%)	0	48

Figure S3. Generation of conditional knockout mice lacking Flvcr1a exclusively in neuronal progenitors (*Flvcr1a*$^{fl/fl}$;NesCRE+), Related to Figure 2

(A) Newborns derived from crossing *Flvcr1a*$^{fl/+}$;NesCRE+ and *Flvcr1a*$^{fl/fl}$ mice. A representative picture is shown. **(B)** Genotyping of embryos and pups derived by crossing *Flvcr1a*$^{fl/+}$;NesCRE+ and *Flvcr1a*$^{fl/fl}$ mice. **(C)** H&E images of P0 lungs derived from *Flvcr1a*$^{fl/fl}$ control and *Flvcr1a*$^{fl/fl;}$NesCRE+ pups. Scale bar 100um. **(D)** The deletion of Flvcr1a was confirmed by PCR on genomic DNA from P0 *Flvcr1a*$^{fl/fl}$;NesCRE+ and *Flvcr1a*$^{fl/fl}$ embryos. The floxed and deleted alleles were amplified using the primers indicated in the methods section. A representative picture is shown. **(E)** Qrt-PCR analysis of *Flvcr1a* mRNA in E14.5 brains dissected from *Flvcr1a*$^{fl/fl}$;NesCRE+ and *Flvcr1a*$^{fl/fl}$ embryos. N=4. **(F)** qRT-PCR analysis of *Flvcr1a* mRNA in E12.5 neural progenitor cells (NPCs) isolated from *Flvcr1a*$^{fl/fl}$;NesCRE+ and *Flvcr1a*$^{fl/fl}$ embryos. N=4. **(G)** qRT-PCR analysis of Flvcr1b mRNA in E14.5 brains dissected from *Flvcr1a*$^{fl/fl}$;NesCRE+ and *Flvcr1a*$^{fl/fl}$ embryos. N=4. **(H)** qRT-PCR analysis of Flvcr1b mRNA in E12.5 neural progenitor cells (NPCs) isolated from *Flvcr1a*$^{fl/fl}$;NesCRE+ and *Flvcr1a*$^{fl/fl}$ embryos. N=4. One Way ANOVA. **=P<0.01; ****=P<0.0001.

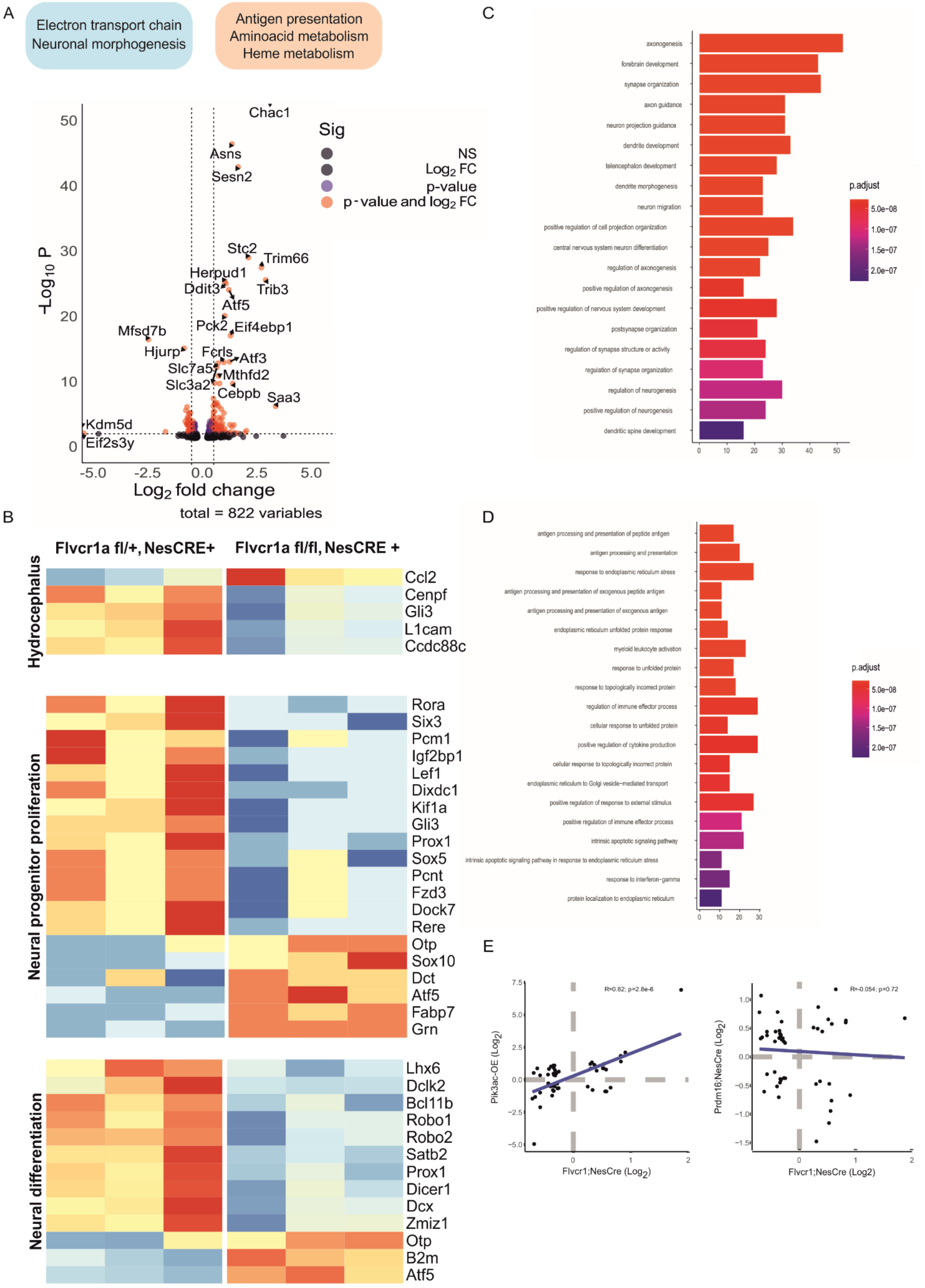
A
Electron transport chain
Neuronal morphogenesis
Antigen presentation
Aminoacid metabolism
Heme metabolism
Chac1
Asns
Sesn2
Stc2
Trim66
Herpud1
Ddit3
Trib3
Atf5
Pck2
Eif4ebp1
Mfsd7b
Hjurp
Fcrls
Atf3
Slc7a5
Mthfd2
Slc3a2
Cebpb
Saa3
Kdm5d
Eif2s3y
Sig
NS
Log2 FC
p-value
p-value and log2 FC
$-Log_{10}$ P
50
40
30
20
10
0
-5.0
-2.5
0.0
2.5
5.0
Log_2 fold change
total = 822 variables
B
Flvcr1a fl/+, NesCRE+
Flvcr1a fl/fl, NesCRE +
Hydrocephalus
Ccl2
Cenpf
Gli3
L1cam
Ccdc88c
Neural progenitor proliferation
Rora
Six3
Pcm1
Igf2bp1
Lef1
Dixdc1
Kif1a
Gli3
Prox1
Sox5
Pcnt
Fzd3
Dock7
Rere
Otp
Sox10
Dct
Atf5
Fabp7
Grn
Neural differentiation
Lhx6
Dclk2
Bcl11b
Robo1
Robo2
Satb2
Prox1
Dicer1
Dcx
Zmiz1
Otp
B2m
Atf5
C
axonogenesis
forebrain development
synapse organization
axon guidance
neuron projection guidance
dendrite development
telencephalon development
dendrite morphogenesis
neuron migration
positive regulation of cell projection organization
central nervous system neuron differentiation
regulation of axonogenesis
positive regulation of axonogenesis
positive regulation of nervous system development
postsynapse organization
regulation of synapse structure or activity
regulation of synapse organization
regulation of neurogenesis
positive regulation of neurogenesis
dendritic spine development
0
10
20
30
40
50
p.adjust
5.0e−08
1.0e−07
1.5e−07
2.0e−07
D
antigen processing and presentation of peptide antigen
antigen processing and presentation
response to endoplasmic reticulum stress
antigen processing and presentation of exogenous peptide antigen
antigen processing and presentation of exogenous antigen
endoplasmic reticulum unfolded protein response
myeloid leukocyte activation
response to unfolded protein
response to topologically incorrect protein
regulation of immune effector process
cellular response to unfolded protein
positive regulation of cytokine production
cellular response to topologically incorrect protein
endoplasmic reticulum to Golgi vesicle−mediated transport
positive regulation of response to external stimulus
positive regulation of immune effector process
intrinsic apoptotic signaling pathway
intrinsic apoptotic signaling pathway in response to endoplasmic reticulum stress
response to interferon−gamma
protein localization to endoplasmic reticulum
0
10
20
30
p.adjust
5.0e−08
1.0e−07
1.5e−07
2.0e−07
E
R=0.62; p=2.8e-6
7.5
5.0
2.5
0.0
-2.5
-5.0
Pik3ac-OE (Log_2)
0
1
2
Flvcr1;NesCre (Log_2)
R=-0.054; p=0.72
1.0
0.5
0.0
-0.5
-1.0
-1.5
Prdm16;NesCre (Log_2)
0
1
2
Flvcr1;NesCre (Log2)

Figure S4. RNA-seq analysis of E14.5 *Flvcr1a*$^{fl/fl}$;NesCRE+ brains highlighted impaired neurogenesis, Related to Figure 2

(A) Volcano plot of most downregulated and upregulated terms in the E14.5 *Flvcr1a*$^{fl/fl}$;NesCRE+ brain highlights electron transport chain among the most downregulated terms and heme metabolism among the most upregulated. **(B)** Heat map showing altered expression of genes involved in hydrocephalus, neural progenitor proliferation and differentiation in E14.5 *Flvcr1a*$^{fl/fl}$;NesCRE+ brains compared to E14.5 *Flvcr1a*$^{fl/+}$;NesCRE+ control brains **(C)** Gene ontology analysis of biological processes in *Flvcr1a*$^{fl/fl}$;NesCRE+ E14.5 brains. **(D)** Gene ontology analysis of biological processes in *Flvcr1a*$^{fl/fl}$;NesCRE+ E14.5 brains. **(E)** Linear regression plots of genes differentially expressed in Flvcr1a and Pik3ac-OE model and in Flvcr1a and Prdm16 OE model.

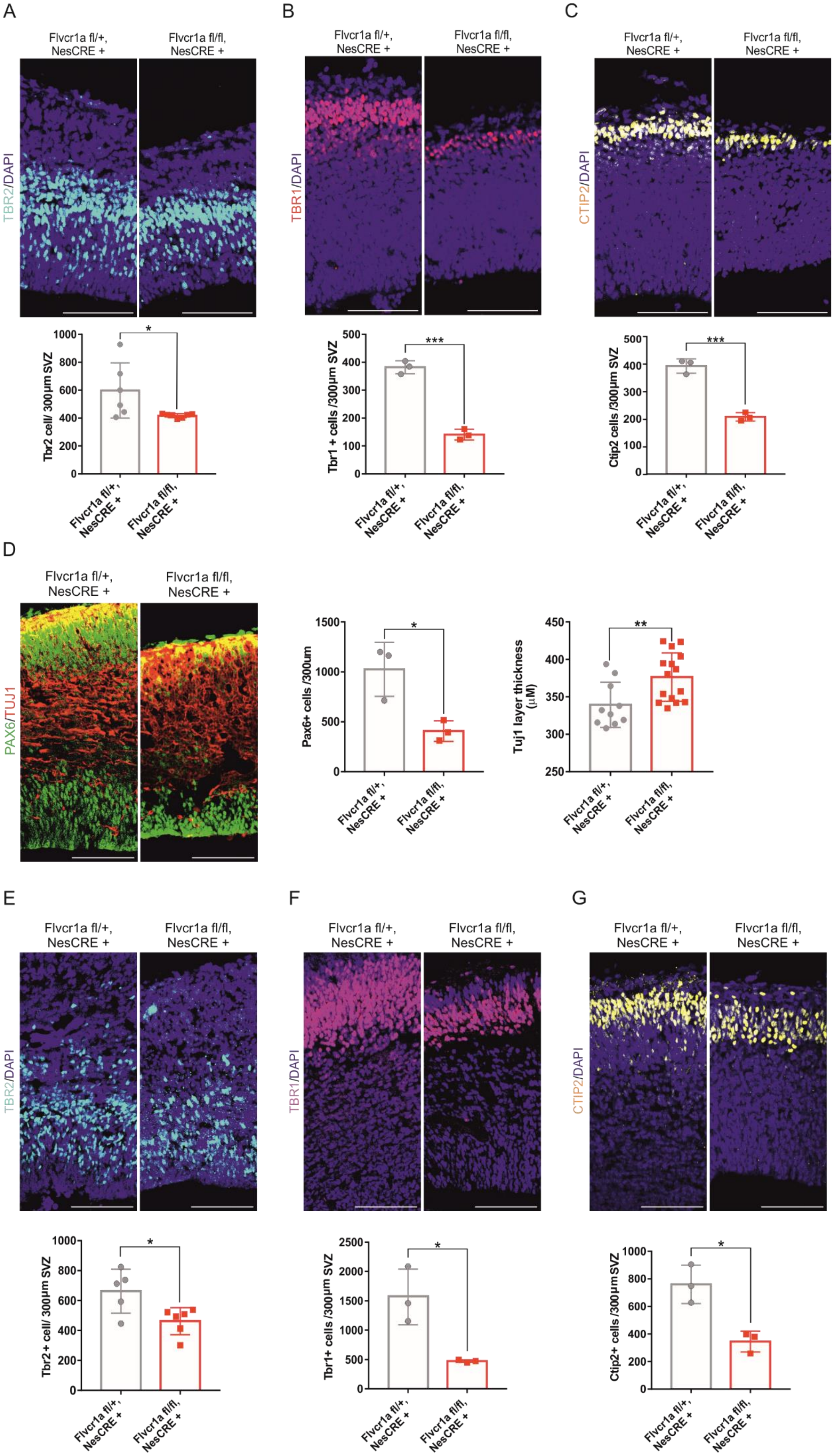
A
Flvcr1a fl/+, NesCRE +
Flvcr1a fl/fl, NesCRE +
TBR2/DAPI
Tbr2 cell/ 300μm SVZ
1000
800
600
400
200
0
*
Flvcr1a fl/+, NesCRE +
Flvcr1a fl/fl, NesCRE +
B
Flvcr1a fl/+, NesCRE +
Flvcr1a fl/fl, NesCRE +
TBR1/DAPI
Tbr1 + cells /300μm SVZ
500
400
300
200
100
0
***
Flvcr1a fl/+, NesCRE +
Flvcr1a fl/fl, NesCRE +
C
Flvcr1a fl/+, NesCRE +
Flvcr1a fl/fl, NesCRE +
CTIP2/DAPI
Ctip2 cells /300μm SVZ
500
400
300
200
100
0
***
Flvcr1a fl/+, NesCRE +
Flvcr1a fl/fl, NesCRE +
D
Flvcr1a fl/+, NesCRE +
Flvcr1a fl/fl, NesCRE +
PAX6/TUJ1
Pax6+ cells /300um
1500
1000
500
0
*
Flvcr1a fl/+, NesCRE +
Flvcr1a fl/fl, NesCRE +
Tuj1 layer thickness (μM)
450
400
350
300
250
**
Flvcr1a fl/+, NesCRE +
Flvcr1a fl/fl, NesCRE +
E
Flvcr1a fl/+, NesCRE +
Flvcr1a fl/fl, NesCRE +
TBR2/DAPI
Tbr2+ cell/ 300μm SVZ
1000
800
600
400
200
0
*
Flvcr1a fl/+, NesCRE +
Flvcr1a fl/fl, NesCRE +
F
Flvcr1a fl/+, NesCRE +
Flvcr1a fl/fl, NesCRE +
TBR1/DAPI
Tbr1+ cells /300μm SVZ
2500
2000
1500
1000
500
0
*
Flvcr1a fl/+, NesCRE +
Flvcr1a fl/fl, NesCRE +
G
Flvcr1a fl/+, NesCRE +
Flvcr1a fl/fl, NesCRE +
CTIP2/DAPI
Ctip2+ cells /300μm SVZ
1000
800
600
400
200
0
*
Flvcr1a fl/+, NesCRE +
Flvcr1a fl/fl, NesCRE +

Figure S5. *Flvcr1a* loss in mouse NPCs results in reduced cortex thickness and reduced number of radial glia (RGCs), intermediate progenitors (IPs) and cortical neurons, Related to Figure 2

(A) Immunostaining of TBR2 (IPs) in *Flvcr1a*$^{fl/fl}$;NesCRE+ mutant and *Flvcr1a*$^{fl/+}$;NesCRE+ E14.5 mouse cortex. DAPI (blue) was used as a nuclear marker. Each dot represents the mean of three images quantified from each animal. N=3. Scale bar=100µm. **(B)** Immunostaining of TBR1 (cortical neurons) in *Flvcr1a*$^{fl/fl}$;NesCRE+ mutant and *Flvcr1a*$^{fl/+}$;NesCRE+ E14.5 mouse cortex. DAPI (blue) was used as a nuclear marker. Each dot represents the mean of three images quantified from each animal. N=3. **(C)** Immunostaining of CTIP2 (cortical neurons) in *Flvcr1a*$^{fl/fl}$;NesCRE+ mutant and *Flvcr1a*$^{fl/+}$;NesCRE+ E14.5 mouse cortex. DAPI (blue) was used as a nuclear marker. Each dot represents the mean of three images quantified from each animal. N=3. Scale bar=100µm. **(D)** Immunostaining of PAX6 (RGCs) and TUJ1 (cortical neurons) in *Flvcr1a*$^{fl/fl}$;NesCRE+ and *Flvcr1a*$^{fl/+}$;NesCRE+ control E16.5 mouse cortex. N=3. Scale bar=100µm. **(E)** Immunostaining of TBR2 (IPs) in *Flvcr1a*$^{fl/fl}$;NesCRE+ and *Flvcr1a*$^{fl/+}$;NesCRE+ control E16.5 mouse cortex. N=3. Scale bar=100µm. N=3 **(F)** Immunostaining of TBR1 (cortical neurons) in *Flvcr1a*$^{fl/fl}$;NesCRE+ and *Flvcr1a*$^{fl/+}$;NesCRE+ control E16.5 mouse cortex. Each dot corresponds to the mean of three different measurements for each brain. N=3. Scale bar=100µm. **(G)** Immunostaining of CTIP2 (cortical neurons) in *Flvcr1a*$^{fl/fl}$;NesCRE+ and *Flvcr1a*$^{fl/+}$;NesCRE+ control mouse cortex. Each dot corresponds to the mean of three different measurements for each brain. N=3 Scale bar=100µm

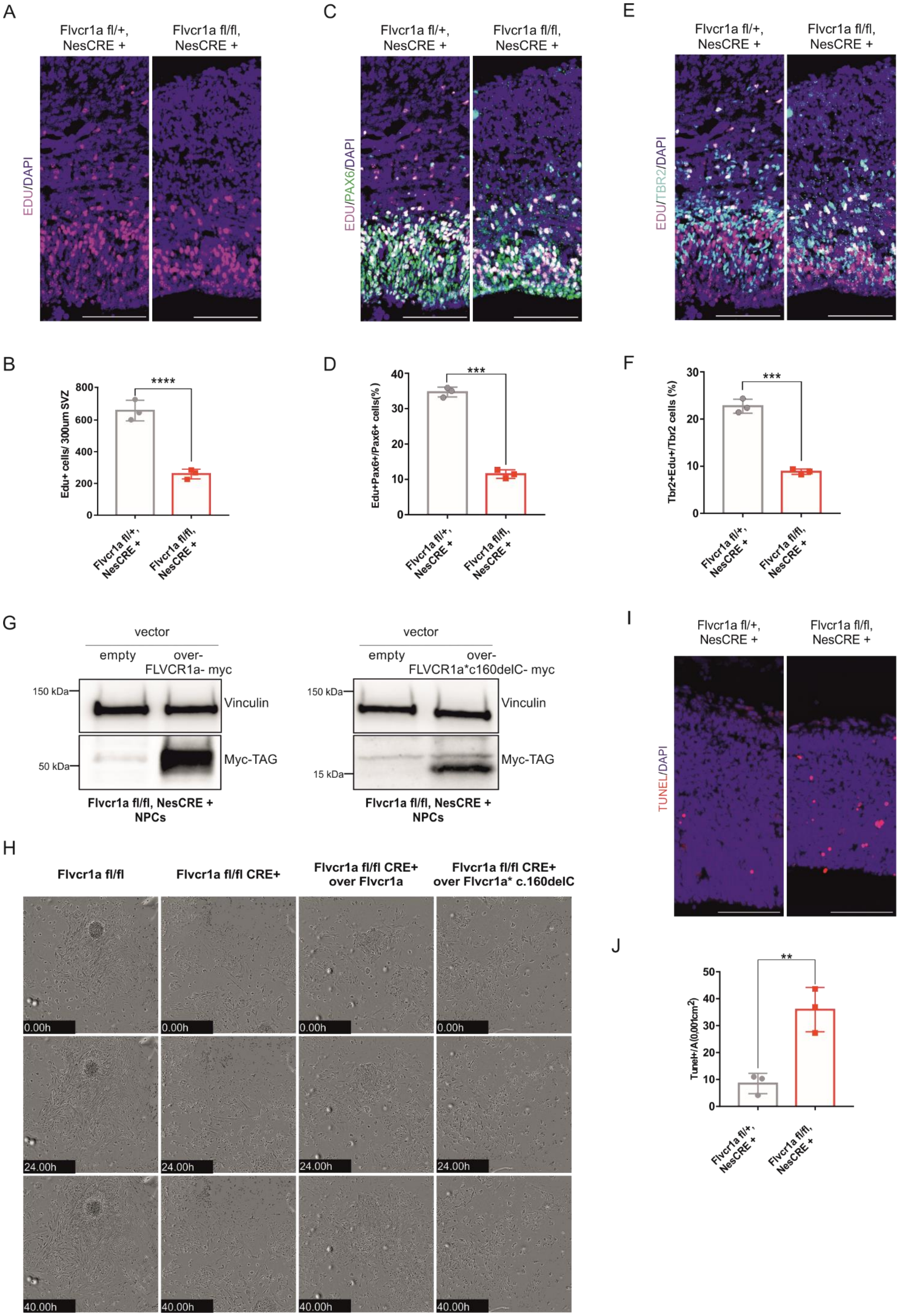
A
Flvcr1a fl/+, NesCRE +
Flvcr1a fl/fl, NesCRE +
EDU/DAPI
C
Flvcr1a fl/+, NesCRE +
Flvcr1a fl/fl, NesCRE +
EDU/PAX6/DAPI
E
Flvcr1a fl/+, NesCRE +
Flvcr1a fl/fl, NesCRE +
EDU/TBR2/DAPI
B
Edu+ cells/ 300um SVZ
800
600
400
200
0
****
Flvcr1a fl/+, NesCRE +
Flvcr1a fl/fl, NesCRE +
D
Edu+Pax6+/Pax6+ cells(%)
40
30
20
10
0
***
Flvcr1a fl/+, NesCRE +
Flvcr1a fl/fl, NesCRE +
F
Tbr2+Edu+/Tbr2 cells (%)
30
20
10
0
***
Flvcr1a fl/+, NesCRE +
Flvcr1a fl/fl, NesCRE +
G
vector
empty
over-FLVCR1a- myc
150 kDa
50 kDa
Vinculin
Myc-TAG
Flvcr1a fl/fl, NesCRE + NPCs
vector
empty
over-FLVCR1a*c160delC- myc
150 kDa
15 kDa
Vinculin
Myc-TAG
Flvcr1a fl/fl, NesCRE + NPCs
H
Flvcr1a fl/fl
Flvcr1a fl/fl CRE+
Flvcr1a fl/fl CRE+ over Flvcr1a
Flvcr1a fl/fl CRE+ over Flvcr1a* c.160delC
0.00h
0.00h
0.00h
0.00h
24.00h
24.00h
24.00h
24.00h
40.00h
40.00h
40.00h
40.00h
I
Flvcr1a fl/+, NesCRE +
Flvcr1a fl/fl, NesCRE +
TUNEL/DAPI
J
Tunel+/A(0,001cm2)
50
40
30
20
10
0
**
Flvcr1a fl/+, NesCRE +
Flvcr1a fl/fl, NesCRE +

Figure S6 *Flvcr1a* loss alters NPCs proliferation, Related to Figure 2

(A) EdU staining of E16.5 *Flvcr1a*$^{fl/fl}$;NesCRE+ mutant and *Flvcr1a*$^{fl/+}$;NesCRE+ cortex. DAPI (blue) was used as a nuclear marker. Scale bar=100µm. **(B)** Relative quantification of EdU positive cells. Each dot corresponds to the mean of three different measurements for each brain. N=3. **(C)** EdU and PAX6 co-staining of E16.5 *Flvcr1a*$^{fl/fl}$;NesCRE+ mutant and *Flvcr1a*$^{fl/+}$;NesCRE+ cortex. DAPI (blue) was used as a nuclear marker. Scale bar=100µm. **(D)** Relative quantification of EdU/Pax6 positive cells. Each dot corresponds to the mean of three different measurements for each brain. N=3. **(E)** EdU and TBR2 co-staining of E16.5 *Flvcr1a*$^{fl/fl}$;NesCRE+ mutant and *Flvcr1a*$^{fl/+}$;NesCRE+ cortex. DAPI (blue) was used as a nuclear marker. Scale bar=100µm. **(F)** Relative quantification of EdU/TBR2 positive cells. Each dot corresponds to the mean of three different measurements for each brain. N=3. **(G)** Immunoblotting of neural progenitor cells (NPCs) isolated from *Flvcr1a*$^{fl/fl}$;NesCRE+ mutant cortexes showing overexpression of FLVCR1a-myc and FLVCR1a*c.160 del-myc. **(H)** Representative images of NPCs isolated from *Flvcr1a*$^{fl/fl}$ control cortexes overexpressing an empty vector and *Flvcr1a*$^{fl/fl}$;NesCRE+ mutant cortexes overexpressing an empty vector, FLVCR1a-myc and FLVCR1a*c.160del-myc. NPCs proliferation was measured for 40 hours post-transfection using Incucyte ® SX5 Live-Cell Analysis. (T-Test; *=P<0.05; **=P<0.01; ***=P<0.001; ****=P<0.0001. **(I)** TUNEL assay of E14.5 *Flvcr1a*$^{fl/fl}$;NesCRE+ mutant and *Flvcr1a*$^{fl/+}$;NesCRE+ cortex. DAPI (blue) was used as a nuclear marker. Scale bar=100µm. **(J)** Relative quantification of TUNEL positive cells. Each dot corresponds to the mean of three different measurements for each brain. N=3

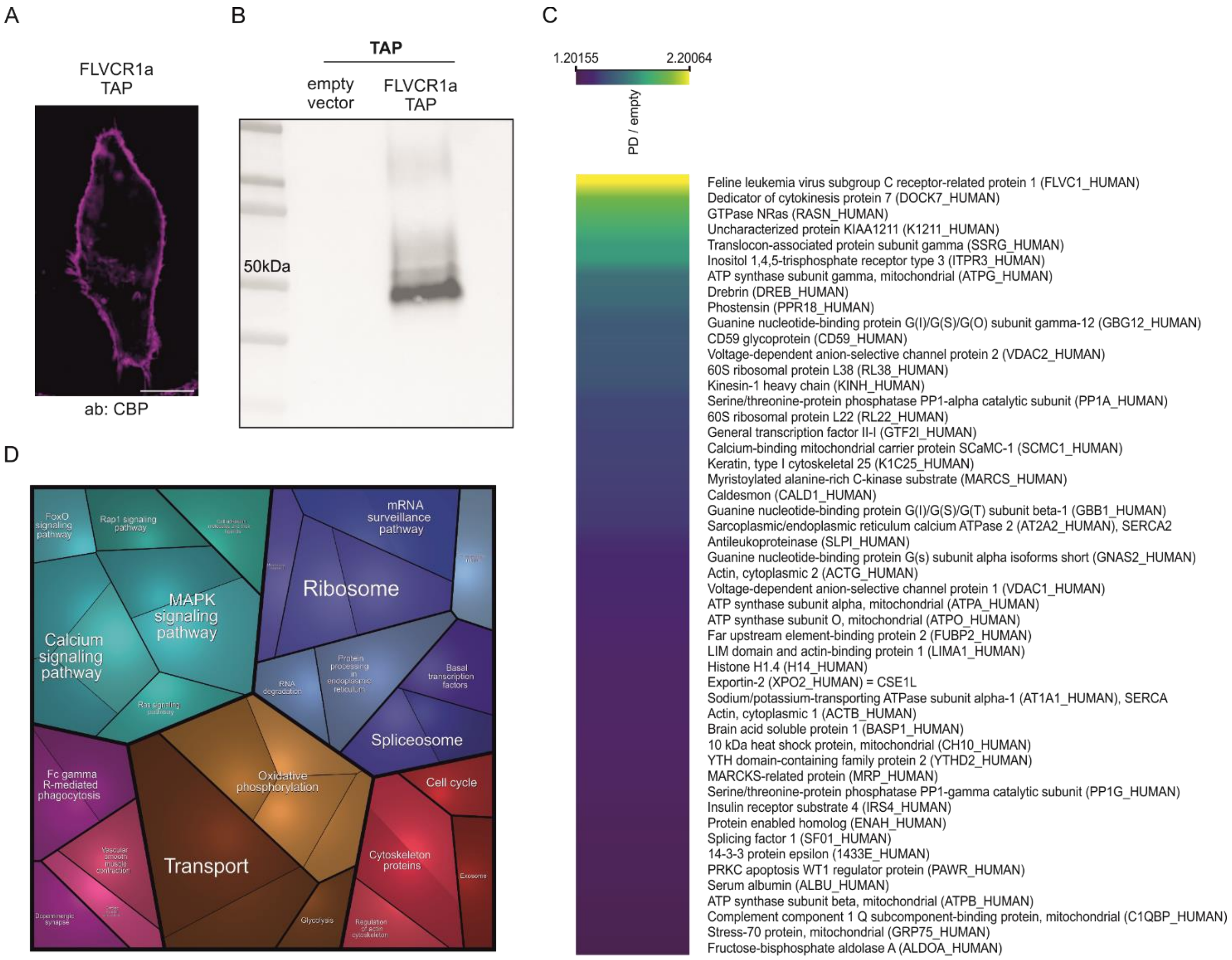

Figure S7. FLVCR1a interactome, Related to Figure 3

(A) Immunofluorescence of FLVCR1a-TAP upon transient overexpression in HeLa cells. An antibody against the (calmodulin binding protein (CBP) tag was used (CBP is part of the TAP tag). Scale bar 10um. **(B)** Western Blot of FLVCR1a following TAP purification. An antibody for FLVCR1a was used. **(C)** Top 50 FLVCR1a interactors, stratified based on the ratio of FLVCR1a-TAP pulldown/empty and sorted for highest enriched proteins from top to lowest on the bottom. **(D)** Proteomaps Voronoi plot based on the top 50 enriched proteins after the pulldown.

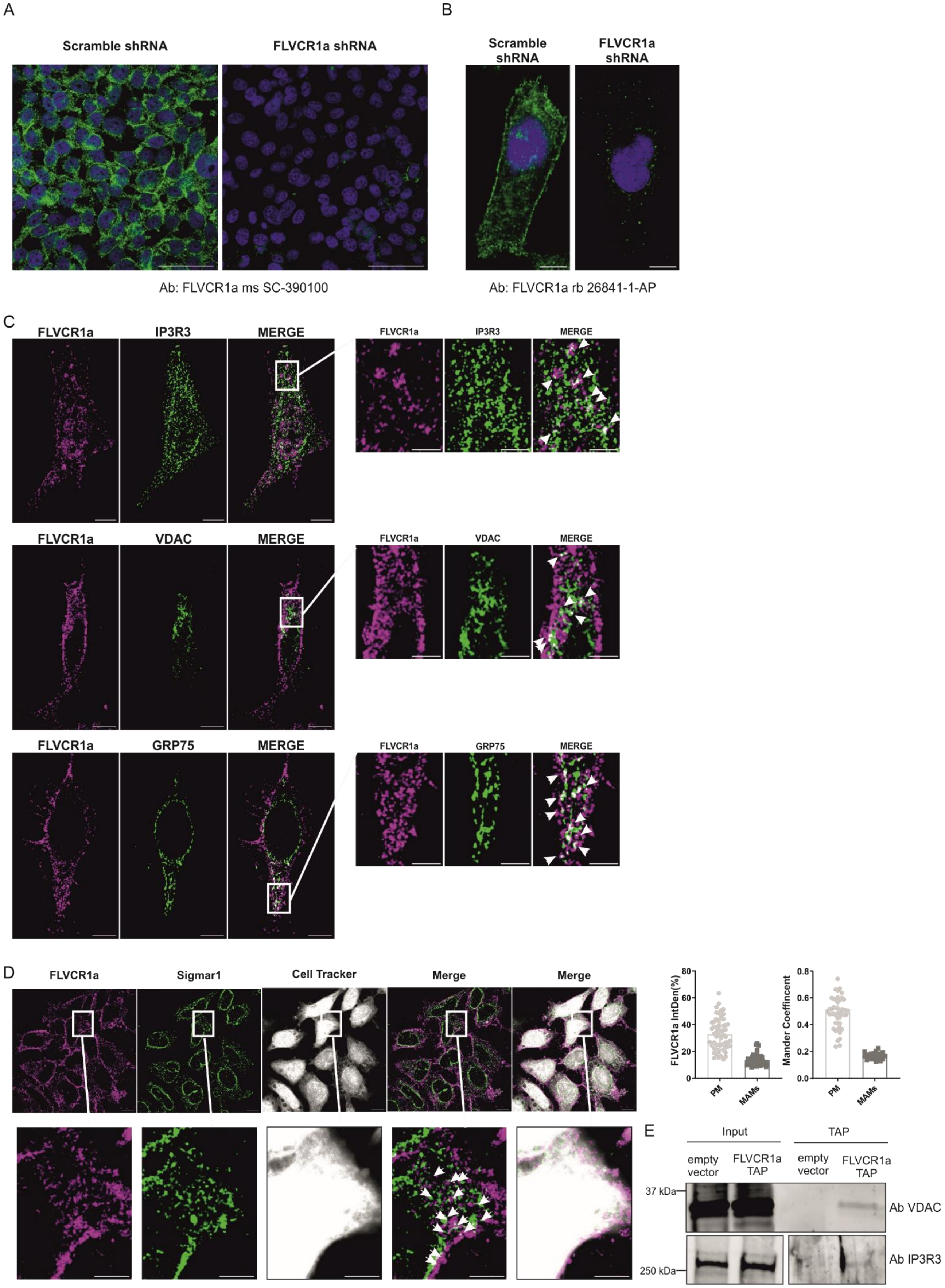
A
Scramble shRNA
FLVCR1a shRNA
Ab: FLVCR1a ms SC-390100
B
Scramble shRNA
FLVCR1a shRNA
Ab: FLVCR1a rb 26841-1-AP
C
FLVCR1a
IP3R3
MERGE
FLVCR1a
VDAC
MERGE
FLVCR1a
GRP75
MERGE
D
FLVCR1a
Sigmar1
Cell Tracker
Merge
Merge
FLVCR1a IntDen(%)
0
20
40
60
80
PM
MAMs
Mander Coeffincent
0.0
0.2
0.4
0.6
0.8
PM
MAMs
E
Input
TAP
empty vector
FLVCR1a TAP
empty vector
FLVCR1a TAP
37 kDa
250 kDa
Ab VDAC
Ab IP3R3

Figure S8. Analysis of FLVCR1a endogenous localization in HeLa cells, Related to Figure 3

(**A**) Immunofluorescence of BTEC (breast tumor endothelial cells) stably down regulating FLVCR1a. A scramble shRNA was used as a control. To visualize FLVCR1a expression the antibody SC-390100 was used. The antibody recognizes the N-terminal part of the protein, allowing specific visualization of FLVCR1a isoform. Scale bar 50um. **(B)** Immunofluorescence of HeLa cells stably down regulating FLVCR1a. A scramble shRNA was used as a control. To visualize FLVCR1a expression the proteintech antibody 26841-1-AP was used. The antibody recognizes the N-terminal part of the protein, allowing specific visualization of FLVCR1a isoform. Scale bar 10µm. **(C)** Immunofluorescence staining for FLVCR1a (magenta) and VDAC1 (green) (top panels), or IP3R3 (green, middle panels), or GRP75 (green; bottom panels) confirms FLVCR1a colocalization in HeLa cells (white arrows). We used the FLVCR1 antibody SC-390100 to analyze the colocalization with IP3R3. We used the FLVCR1 antibody (proteintech 26841-1-AP) in the other circumstances. Scale bar=10µm. Image magnifications are shown at the side. Scale bar=5µm. **(D)** Immunofluorescence staining of FLVCR1a (SC-390100) endogenous localization in HeLa cells. MAMs were marked using the sigmar1 antibody (green) while the whole cell was stained with the cell tracker (white). Image magnifications are shown. Scale bar=5µm. The percentage of FLVCR1a localizing at the plasma membrane or at MAMs is shown on the right together with the colocalization index with both compartments (Manders Coefficient). **(E)** Tandem affinity purification of FLVCR1a-TAP protein followed by western blot of endogenous VDAC and IP3R3 confirms protein-protein interaction. The empty vector expressing the TAP tag alone served as an irrelevant interacting protein.

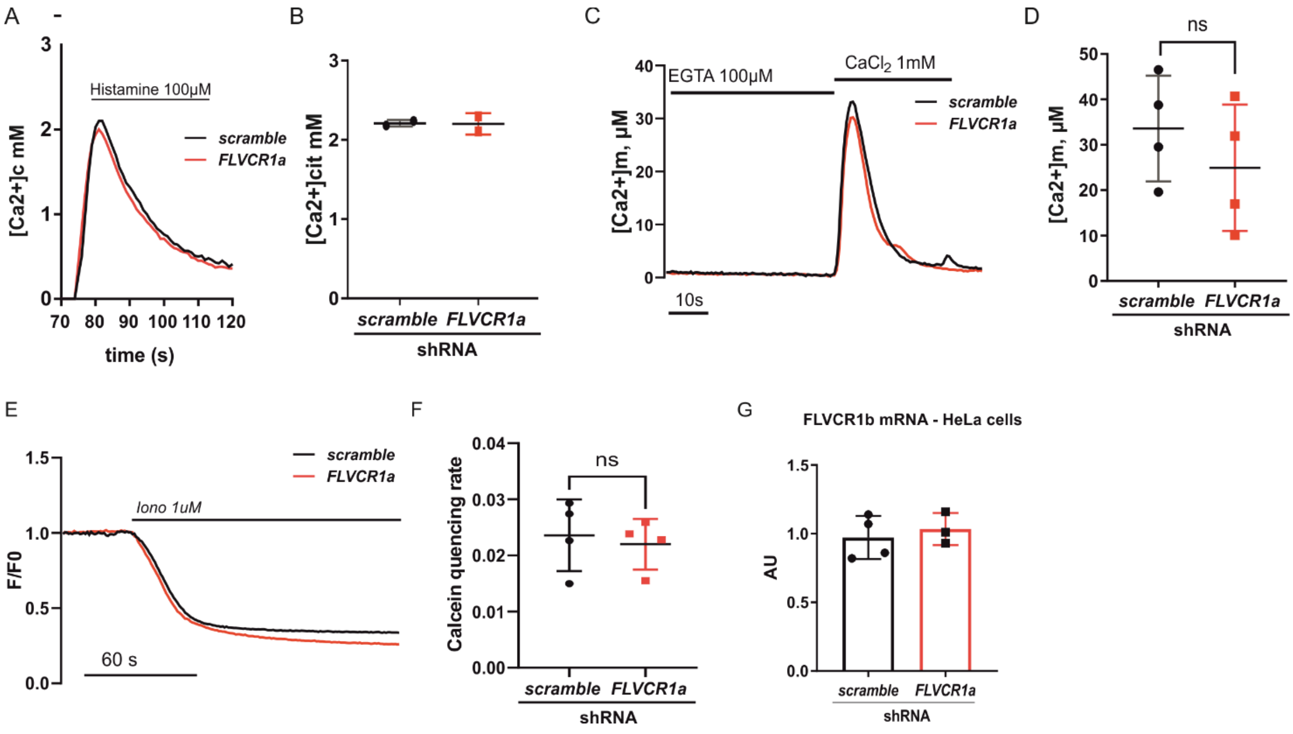

Figure S9. Cellular calcium handling in FLVCR1a-down modulated and control HeLa cells, Related to Figure 4

(A) Cytosolic calcium measured as Ca2+ responses to an agonist stimulation (100 µM Histamine) in HeLa cells expressing a cytosolic aequorin-based probe. Representative calcium traces are shown. **(B)** Quantification of peak cytosolic calcium amplitude in HeLa cells upon agonist stimulation. Each dot represents the mean of five different wells from two independent experiments. N=2 **(C)** Mitochondrial calcium elevation in HeLa cells expressing a mitochondrial aequorin-based probe in response to extracellular calcium deprivation and (EGTA 100uM) followed by extracellular calcium restoration (CaCl2 1mM). Representative traces are shown. **(D)** Quantification of peak mitochondrial calcium amplitude in HeLa cells upon extracellular calcium deprivation followed by extracellular calcium restoration. Each dot represents the mean of five different wells from four independent experiments. N=4. **(E)** Calcein quenching rates after ionomycin stimulation in HeLa cells. Representative traces are shown. **(F)** Quantification of calcein quenching rates in HeLa cells after ionomycin stimulation. Each dot represents the mean of four independent experiments. N=4. **(G)** qRT-PCR analysis of Flvcr1b mRNA in control and FLVCR1a-down modulated HeLa cells. N=4.

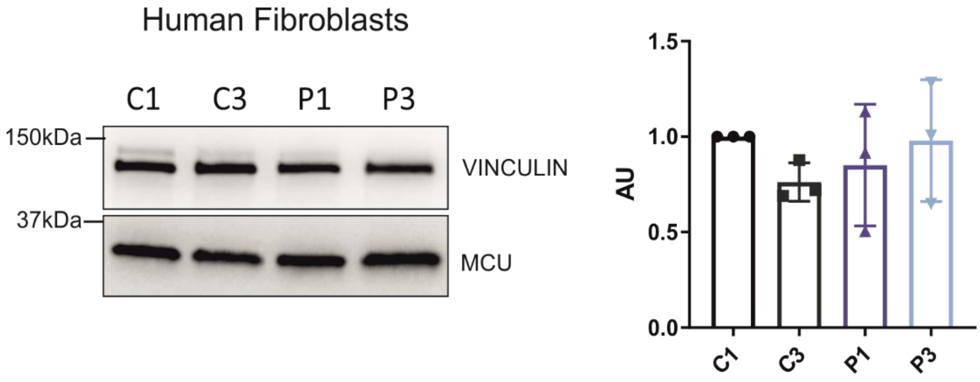

Figure S10. Mitochondrial Calcium Uniporter (MCU) expression levels in human primary fibroblasts carrying *FLVCR1* mutations and controls, Related to Figure 5

Immunoblotting showing MCU expression levels in primary fibroblasts derived from PCARP/HSAN patients (P1 and P3) and healthy subjects (C1 and C3). Vinculin was used as loading control. The relative quantification is shown on the right. Each dot represents the mean expression of three independent experiments. N=3.

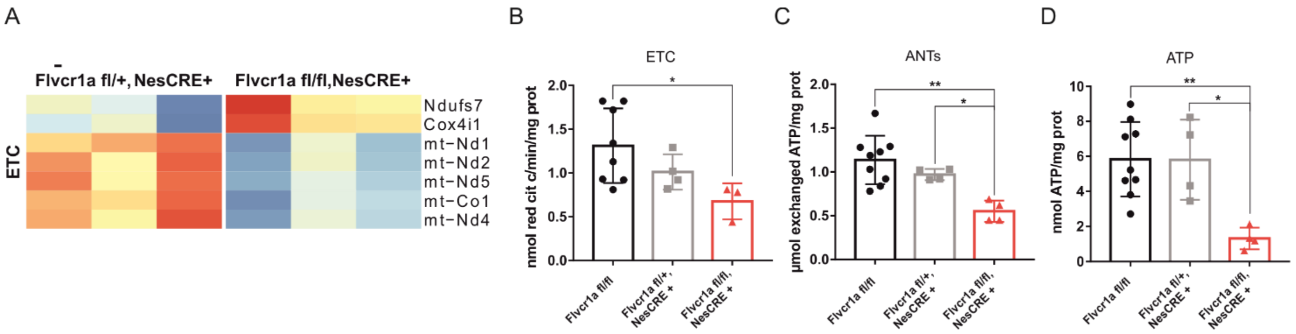

Figure S11. Reduced oxidative metabolism in E14.5 *Flvcr1a*$^{fl/fl}$;NesCRE+ total brains, Related to Figure 6

(A) Heat map showing altered expression of genes encoding the electron transport chain (ETC) complexes in E14.5 *Flvcr1a*$^{fl/fl}$;NesCRE+ brains. **(B)** Activity of the mitochondrial electron transport chain (ETC) complexes I-III in *Flvcr1a*$^{fl/fl}$;NesCRE+ mutant and *Flvcr1a*$^{fl/fl}$, *Flvcr1a*$^{fl/+}$;NesCRE+ control brains. Results are shown as nmoles reduced cytochrome c/ min/mg of mitochondrial protein. N=8,4,4. **(C)** Mitochondria ANTs activity in *Flvcr1a*$^{fl/fl}$;NesCRE+ mutant and *Flvcr1a*$^{fl/fl}$, *Flvcr1a*$^{fl/+}$;NesCRE+ control brains. Results are expressed as µmoles exchanged ATP/mg mitochondrial protein. N=8,4,4. **(D)** ATP levels measured by a bioluminescence assay. Results are shown as nmoles ATP/mg of mitochondrial proteins. N=8,4,4. (One way anova: *=P<0.05; **=P<0.01).

SUPPLEMENTARY REFERENCES

S1. Fietz, S.A., Lachmann, R., Brandl, H., Kircher, M., Samusik, N., Schröder, R., Lakshmanaperumal, N., Henry, I., Vogt, J., Riehn, A., et al. (2012). Transcriptomes of germinal zones of human and mouse fetal neocortex suggest a role of extracellular matrix in progenitor self-renewal. Proc Natl Acad Sci U S A *109*, 11836-11841. 10.1073/pnas.1209647109.

S2. Nowakowski, T.J., Bhaduri, A., Pollen, A.A., Alvarado, B., Mostajo-Radji, M.A., Di Lullo, E., Haeussler, M., Sandoval-Espinosa, C., Liu, S.J., Velmeshev, D., et al. (2017). Spatiotemporal gene expression trajectories reveal developmental hierarchies of the human cortex. Science *358*, 1318-1323. 10.1126/science.aap8809.